DESIGN, DEVELOPMENT, AND VERIFICATION OF A GNSS-R UAV-BASED PAYLOAD FOR REFLECTOMETRY APPLICATIONS

SOGAND TALEBI

A THESIS SUBMITTED TO

THE FACULTY OF GRADUATE STUDIES

IN PARTIAL FULFILLMENT OF THE REQUIREMENTS

FOR THE DEGREE OF

MASTER OF SCIENCE

Graduate Program in Earth and Space Science

York University

Toronto, Ontario

February 2024

ABSTRACT

This thesis focuses on the design, development, and verification of a Global Navigation Satellite System-Reflectometry (GNSS-R) payload tailored for Unmanned Aerial Vehicles (UAVs) utilizing Commercial Off-The-Shelf (COTS) components. UAVs serve as versatile aerial platforms capable of operating at diverse altitudes, thereby offering varying levels of spatial resolution suitable for localized remote sensing applications. A customized GNSS-R payload was created and tested in a comprehensive flight campaign over diverse terrains. The collected data underwent post-processing to generate reflectometry products, such as Delayed Doppler Maps (DDM) and Delayed Waveforms (DWF). Comparative analyses were conducted on GNSS-R reflections from different surfaces to confirm the payload's reflectometry capabilities. The research results offer valuable insights into the practical applications of GNSS-R technology in remote sensing, emphasizing its potential viability for various applications in this field.

ACKNOWLEDGEMENTS

I want to express my sincere gratitude to my supervisor, Dr. Bisnath, for his invaluable mentorship, unwavering compassion, and uplifting humour when it mattered most. I also want to thank Dr. Lee for treating me as her student and offering me indispensable guidance. I am deeply thankful to my lab partner (soon-to-be Dr.) Gavili, for her support and generous sharing of her knowledge in reflectometry. Special thanks to Mr. Samigulin for his assistance with the Raspberry Pi. I am also indebted to everyone at the GNSS-Lab and York University who has provided support in various experiments over the years. Lastly, my most profound appreciation goes to my closest friends and family, my steadfast cheerleaders these past few years. Your unwavering support has been a source of strength and encouragement.

TABLE OF CONTENTS

LIST OF TABLES

LIST OF FIGURES

Chapter 1
Introduction

GNSS-Reflectrometry (GNSS-R) is a remote sensing technique that uses these ubiquitous, freely available, reflected GNSS signals to derive fundamental geophysical properties of the reflecting surface. The World Meteorological Organization (WMO) recognized soil moisture as an essential climate variable (ECV) due to its critical contribution to characterizing Earth's climate (WMO 2021). Soil Moisture Content (SMC) is often expressed as a ratio of water contained in soil, and it serves a key role in the planet's water and energy cycles through evapotranspiration. SMC determination is important to researchers, policymakers, and entities concerned with "weather and climate, runoff potential and flood control, soil erosion and slope failure, reservoir management, geotechnical engineering, and water quality" (Arnold 1999).

York University's GNSS Laboratory is working on the Technology Demonstration of Soil Moisture Monitoring with Reflected GNSS signals project under the Canadian Space Agency's Flights and Fieldwork for the Advancement of Science and Technology (FAST) program. The project aims to develop a flight-ready GNSS-R receiver payload and processing algorithm for surface soil moisture detection and demonstrate it onboard an airborne platform (CSA 2019). This research focuses on developing an affordable GNSS-R payload capable of seamless integration into commercial UAVs. It serves as an initial exploration into obtaining localized reflectometry measurements to derive valuable information, such as soil moisture content for agricultural purposes.

1.1 Research Objectives

This thesis aims to achieve two primary research objectives. The first objective involves the design and development of a GNSS-Reflectometry payload specifically for commercial UAVs (Unmanned Aerial Vehicles). The second objective entails the verification of the reflectometry capabilities through the post-processing of flight data obtained from the developed payload. To accomplish these objectives, the study encompasses a comprehensive examination of the GNSS-R payload architecture, the setup for field testing, and the generation of reflectometry products during the post-processing phase.

1.1.1 GNSS-R Payload Architecture

The goal of designing the payload architecture involved studying the history and state-of-the-art GNSS-Reflectometry technology. The most recent GNSS-R space mission, known as CYGNSS and conducted by NASA, was reviewed during this exploration. CYGNSS employs a GNSS-R method, collecting direct and reflected signals using zenith and nadir-looking antennas. The nadir antenna, capable of receiving signals with both left and right-handed polarization, adds supplementary datasets for exploration during post-processing. With the knowledge gained, a decision was made to employ commercial-off-the-shelf (COTS) hardware for constructing the payload. The primary objective was to create a cost-effective and accessible design suitable for deployment on various commercial UAVs. These overarching objectives led to the establishment of three fundamental requirements for the payload design: the capability to collect three RF streams, non-interference with the UAV's flight operations, and the maintenance of structural integrity to minimize vibrations during flight.

1.1.2 Field Test Set-up

One of the aims of this thesis is to validate the reflectometry capabilities of the payload. One straightforward approach to achieve this involves the comparison of reflections obtained from three distinct surfaces with varying reflective characteristics. To facilitate this experiment, the Toronto Scarborough Bluffs beach was chosen as the test location. The selected site offers an ideal setting due to its proximity to Lake Ontario, a sandy shoreline for land reflections, and the densely vegetated Scarborough Bluffs escarpment. These three diverse surfaces are expected to exhibit notable disparities in their interactions with GNSS signals, providing valuable data for verifying the payload's reflectometry component.

1.1.3 Post-Processing of the Data

To validate the reflectometry capabilities, post-processing software initially developed for the CYGNSS mission is employed. The process unfolds in distinct steps. Initially, the direct GNSS results are processed and cross-referenced with alternative data sources to ensure the accuracy of the payload's navigational solutions. Subsequently, the generation of Reflectrometry products, specifically the Delayed Waveform (DWF) and the Delayed Doppler Map (DDM), takes place for each dataset corresponding to the reflective surfaces of water, sand, and vegetation. This procedure is carried out for the top three satellites for which direct signals were acquired. The resulting DWFs and DDMs from each surface are then compared to one another, confirming the reflectometry capabilities of the payload.

1.2 Design Limitations/Boundaries

The original design of the payload aimed to achieve various objectives, such as storing raw data for later ground-based processing, providing GNSS navigation solutions, and

generating reflectometry products like Delayed Waveform (DWF) and Delayed Doppler Map (DDM) on board. Within the research scope, the focus shifted to capturing digitized IF-reflected signals and performing post-processing on the ground using NASA's CYGNSS software. To accomplish this, a Raspberry Pi was selected as the onboard computer, and a Python script was created to reformat the captured dataset into a suitable input format for the CYGNSS software.

Although this payload was constructed as part of the demonstration of technology for soil moisture monitoring utilizing GNSS-R capabilities, the boundaries of this thesis extend only to the completion of the verification of the reflectometry products. Further processing, such as soil moisture monitoring and detection, involves more extensive post-processing procedures that lie beyond the scope of this thesis. Nevertheless, soil moisture is highlighted as a use case application for a UAV-based GNSS-R payload. This is because soil moisture measurements necessitate a higher spatial resolution, which can be achieved by flying the UAV closer to the Earth's surface.

1.3 Thesis Contribution

This thesis outlines the payload design, development, and verification of a GNSS-R payload onboard a UAV aerial platform as part of CSA's FAST program. The project focuses on the demonstration of soil moisture monitoring technology with reflected GNSS signals. These are the three main contributions made by this thesis to the project above:

1. Design of the GNSS-R payload architecture to meet the GNSS-R scientific requirements.

2. Building the payload to seamlessly integrate with the chosen UAV platform and planning and conducting flight field campaigns to collect data effectively with the payload onboard.

3. Verification of the GNSS-R receiver payload and the processing reflectometry algorithm using the field data set.

This thesis attempts to contribute to the field through the innovative design of the GNSS-R payload using COTS, the use of UAVs for field campaigns, and the thorough verification of the developed technology using real-world data. These aspects collectively enhance the understanding and applicability of GNSS-R technology for soil moisture monitoring.

1.4 Thesis Outline

This thesis summarises the concepts and history of GNSS-R, the design and development of a GNSS-R payload for a UAV, and the subsequent verification achieved through post-processing of the collected data. Chapter 1 serves as an introductory chapter, setting the stage for the study by outlining its motivation and objectives. This chapter also clarifies how the thesis aligns with the broader CSA project. Chapter 2 presents a comprehensive literature review and background information on GNSS-R as a remote sensing method. Additionally, the fundamental concepts crucial for post-processing are discussed. Chapter 3 delves into the design and structure of the payload derived from the requirements. This chapter also covers the setup for the flight campaign. Chapter 4 is dedicated to the post-processing of the flight data sets. It encompasses verifying the results obtained through direct acquisition, identifying specular points from the satellites, and presenting DWFs and DDMs for the reflected signals originating from these satellites. These data are systematically compared to validate the performance of the payload. Concluding the study in Chapter 5 is an overview of the work accomplished thus far and recommendations for future research endeavours.

Chapter 2
GNSS-R Fundamentals

This chapter serves as an introduction to GNSS and reflectometry. It commences by delving into GNSS's historical evolution and fundamental principles, encompassing signal transmission and structure. Subsequently, the focus shifts to reflectometry, providing an overview of its historical development, state-of-the-art missions, and their diverse applications in airborne, space-based, and UAV missions. Additionally, essential concepts such as the Delayed Doppler Map (DDM), Delayed Waveform (DWF), and specular points are introduced.

2.1 Global Navigation Satellite System

Global Navigation Satellite Systems (GNSS) have become indispensable for various terrestrial applications, including surveying, remote sensing, tracking, and aviation (Egea-Roca et al. 2022). This section explores a brief history of GNSS, its basic concepts, signal transmission and structure, and the architecture and components that make up the receivers built to process these GNSS signals.

2.1.1 History and Basic Concepts

GNSS is a term used for a constellation of satellites that provide global coverage, positioning, navigation, and timing (PNT) solutions. Multiple GNSS constellations exist in Earth's orbit, such as Europe's Galileo, Russia's Global'naya Navigatsionnaya Sputnikovaya Sistema (GLONASS), and China's BeiDou. Figure 2.1 shows a visual representation of these four constellations. This research focuses on the USA's Global Positioning System (GPS) since it is one of the most widely used satellite navigation systems globally,

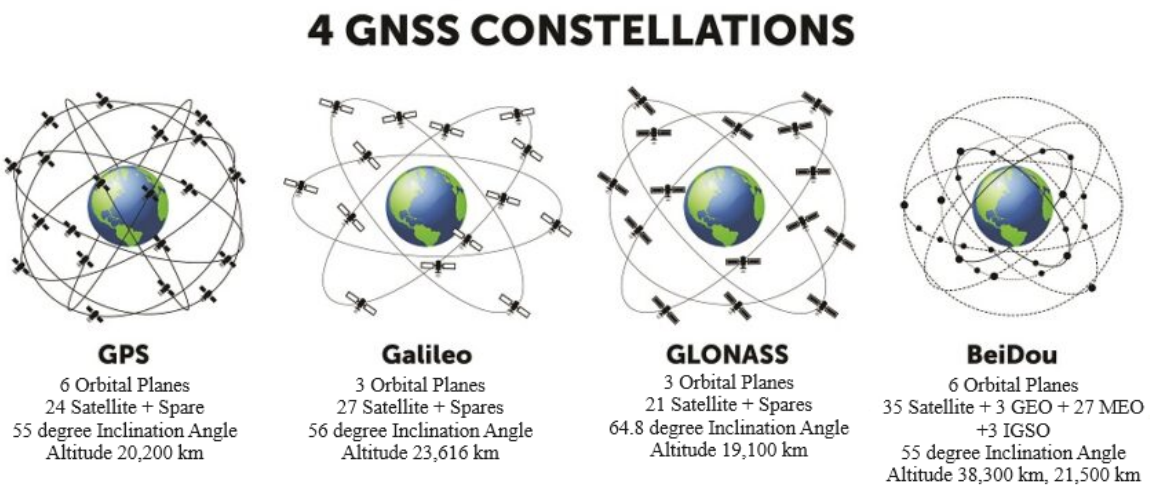

Figure 2.1: Visualization of some of the prominent GNSS constellations (Sickle 2001)

with extensive incorporation of GPS signals in remote sensing literature. The first GPS satellite was launched in the 1970s, and by the 1990s, there were 24 satellites in orbit, making the constellation fully operational (Hofmann-Wellenhof et al. 2007).

The GPS satellite constellation consists of six orbital planes, each inclined at 55 degrees. In theory, a minimum of 24 satellites is sufficient to guarantee that users always have access to at least four visible satellites. Nevertheless, the current GPS constellation comprises 32 satellites to ensure continuous coverage, accounting for satellite servicing and decommissioning needs. These satellites follow nearly circular orbits with eccentricities of less than 0.02. Their orbits place them in the Medium Earth Orbit (MEO) category, situated at an altitude of approximately 20,000 kilometers. Notably, these satellites complete two orbits around the Earth in a single day (Leick et al. 2015).

2.1.2 GPS Signal Transmission

GPS satellites utilize right-hand circular polarization (RHCP) for signal transmission, a choice to overcome the drawbacks of linear polarization. Circular polarization helps mitigate issues like polarization fading and the potential for poor signal reception. These

challenges arise from two factors: the satellites' motion in relation to receivers on Earth and the Faraday rotation caused by the ionosphere. Faraday rotation causes electromagnetic waves to reach the Earth's surface with a different polarization angle than without the ionosphere (Moernaut et al. 2009). GPS satellite signals traverse through space, and as these signals reach Earth, their received power levels drop below the thermal noise floor (see Figure 2.2).

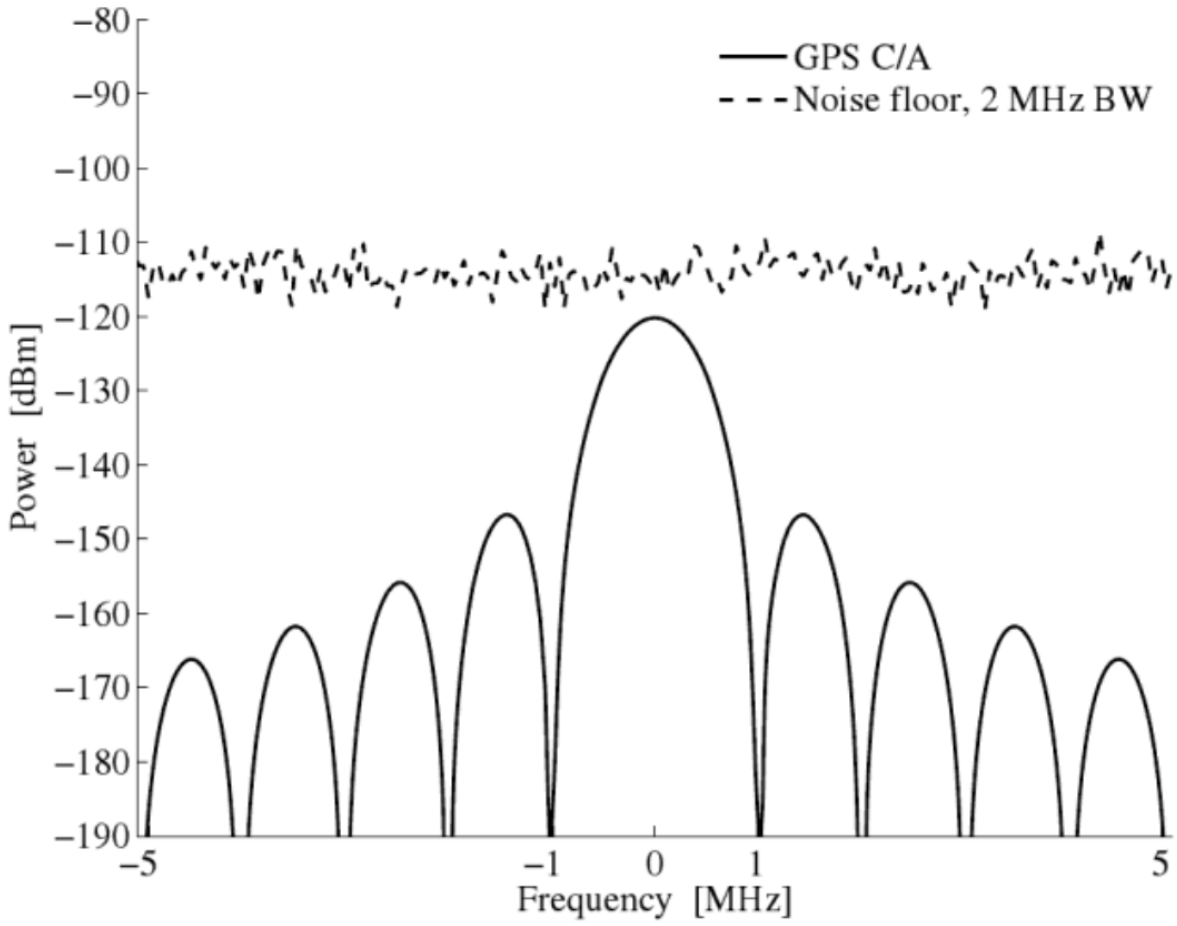

Figure 2.2: Frequency Domain of the GPS signal and thermal noise power (Borre et al. 2007)

When received on the Earth's surface, the GPS signals are actually below the thermal noise floor. In simpler terms, if a GPS antenna is connected to a spectrum analyzer, the GPS signal stays hidden amidst the noise. This means that the signal can be recovered

from the noise only through processing. Thermal noise is a background noise that exists in all receivers due to the random motion of electrons within conductors that are present, and it is directly related to temperature.

The thermal noise floor discussion provides valuable insights into the power of received GPS signals on Earth. It contextualizes the weakness of these signals and sheds light on the even more challenging task of capturing and analyzing fainter reflected signals utilized in reflectometry. The GPS antenna gain pattern is deliberately designed to maintain relatively consistent received signal strength, whether receiving a satellite signal from the horizon or at the zenith. Figure 2.3 depicts the guaranteed received power based on the user elevation angle; the minimum power received is -128.5 dBm. Discussion about the thermal noise floor is important to fully capture and understand the relative weakness of the GPS signals and put in perspective the weakness of reflected signals, which are used for reflectometry purposes.

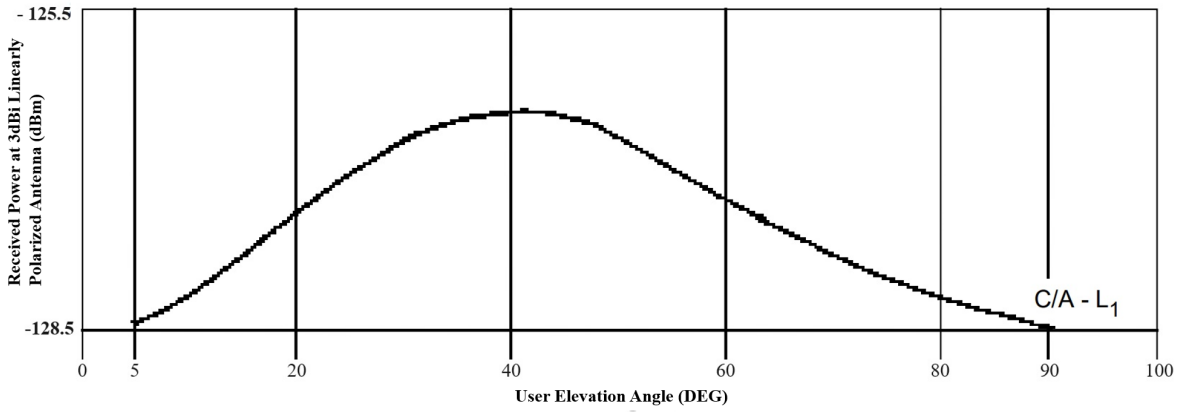

Figure 2.3: User received minimum signal level variations (Flores 2021)

2.1.3 GPS Signal Structure

The original design of the GPS signal structure contained two signal outputs: L1, operating at a carrier frequency of 1575.42 MHz, and L2, at a frequency of 1227.60 MHz. The generation of these frequencies initially involves multiplying the fundamental frequency,

f_0=10.23 MHz, produced by the onboard atomic clocks.

- L1 frequency $f_{L1} = f_0 * 154 = 1575.42$ MHz
- L2 frequency $f_{L2} = f_0 * 120 = 1227.60$ MHz

There are two PRN codes generated by GPS satellites, C/A-code or coarse acquisition and P-code or Precision code. The notable differences between C/A-code and the P-code are given in Table 2.1.

	C/A-code	**P-code**
Transmission rate:	1.023 MHz	10.23 MHz
Intended application:	Civilian use	Military use
Transmitted on:	L1	L1 & L2

Table 2.1: Differences between C/A-code and P-code

As shown in Figure 2.4, three digital signals are used superimposed onto the carrier frequencies L1 and L2 to transmit information used to provide positioning, navigation and timing services. These three digital signals are composed of two PRN (pseudo-random noise) codes, namely C/A-code and P-code, and a navigation message.

The navigation message of 50 bits/second is continuous data, which is a modulo two sum with C/A-code and P-code, and these codes are modulated with L1 and L2 carrier signals. The navigation message encompasses crucial information, including the current status of the GPS satellite constellation, the time of transmission from each satellite, time transfer to Coordinated Universal Time (UTC), corrections for satellite clocks, precise satellite positions (ephemeris), and details regarding satellite health and the effects of propagation delay (Lawrence 2013).

The navigation messages transmitted by each satellite differ according to factors such as health status and approximate location. As shown in figure 2.4, the navigation message is common to C/A-code and P-codes on both the L1 and L2 frequencies.

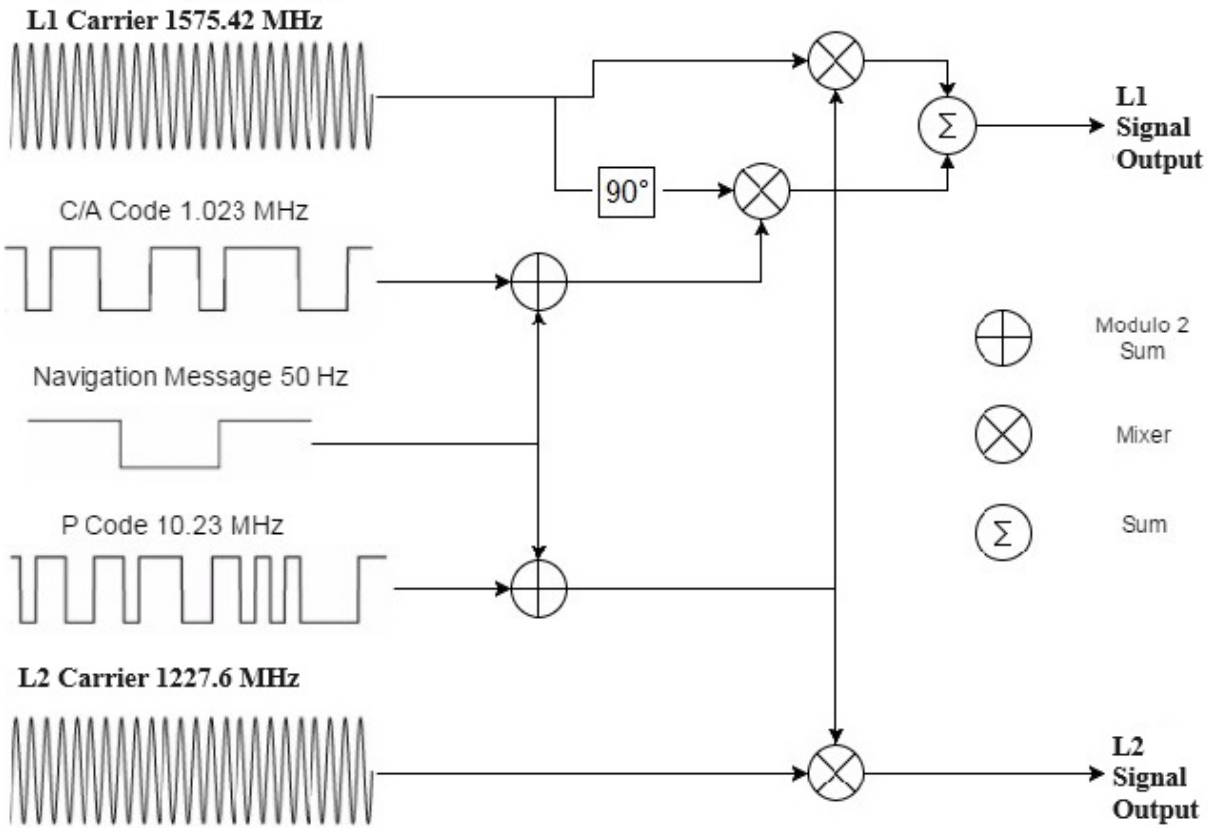

Figure 2.4: GPS signal modulation (Süzer et al. 2017)

2.1.4 GNSS Receiver Basic Structure

This section dives into the essential workings of a typical GNSS receiver. It begins with the antenna capturing signals from GNSS satellites, which are then passed to the RF front-end receiver. The front-end filters, conditions, and converts these analog signals into digital data (see figure 2.5). Next, the receiver processes the digitized data, identifying the source satellites and decoding the signals to create a comprehensive navigation solution. These explanations set the stage for understanding the concepts in the following two chapters. Figure 2.5 also provides a block diagram of a conventional GNSS receiver.

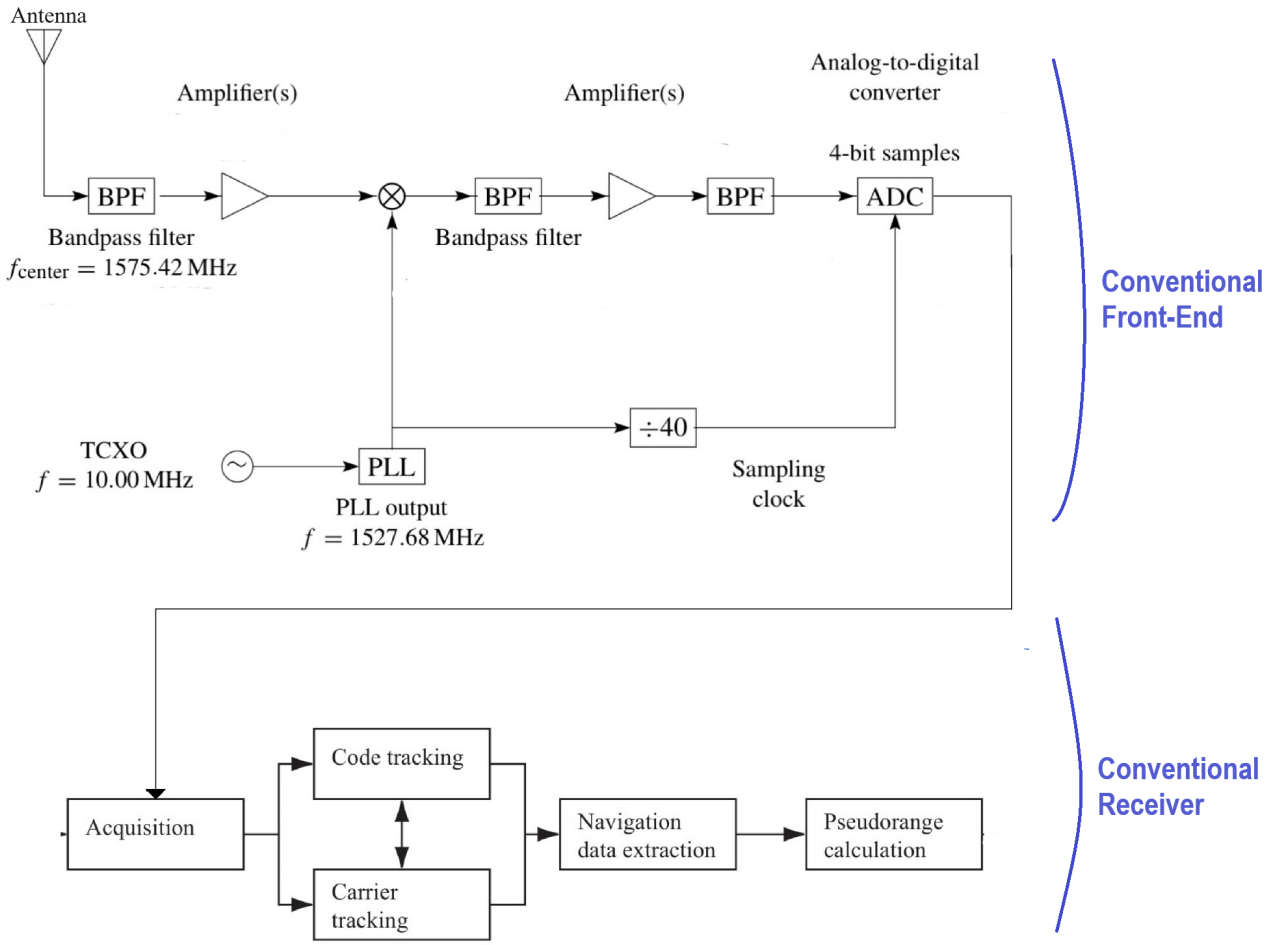

Figure 2.5: (Top) Block diagram of a conventional GNSS front-end; (Bottom) Block diagram of a conventional GNSS receiver (Borre et al. 2007)

2.1.4.1 Antenna

Antennas serve two main functions based on their functionality: receiving and transmitting signals. Apart from the transmitting GNSS antennas used on GNSS satellites, receiving GNSS antennas exclusively receive signals and focus solely on capturing signals emitted at specific frequencies. The primary role of a receiving antenna involves converting electromagnetic waves into electrical signals, a process elucidated by the principle of electromagnetic induction. This discussion on GNSS antenna design will delve into three fundamental parameters: frequency, polarization, and gain pattern.

In designing antennas, the aim is to induce a voltage from the electromagnetic waves

of a particular frequency. For instance, a GNSS antenna can be tailored to pick up GPS L1 signals at 1575.42 MHz and GPS L2 signals at 1227.60 MHz. The acceptance of these frequencies occurs within a defined bandwidth, influenced by factors like voltage standing wave ratio (VSWR) and impedance. VSWR measures impedance mismatch, providing insights into how much incident power is absorbed versus reflected (Balanis 2016).

Electromagnetic wave polarization pertains to the path created by the electric field vector over time. Circular polarization, shown in Figure 2.6, is emphasized for GNSS applications due to its suitability for space transmission compared to linear counterparts. GPS satellites transmit signals with right-hand circular polarization (RHCP), necessitating that receiving antennas adopt RHCP. However, it is crucial to acknowledge that no antenna is perfect. Despite the focus on RHCP, there is a possibility of picking up left-hand circular polarization (LHCP) energy, known as the cross-polar element. Consequently, the real-world challenge lies in achieving optimal RHCP while managing the presence of LHCP signals (Schmidhuber et al. 2022).

The antenna gain pattern plays a crucial role in determining the antenna's directivity, which measures how radiation emitted by the antenna is concentrated in a specific direction. An isotropic radiator, with a directivity of 1, radiates equally in all directions, resembling a sphere. However, this is not ideal for transmitting or receiving antennas as it results in a wasteful distribution of radiative power (Milligan 2005). To illustrate, Figure 2.7 showcases the gain pattern of an active GPS L1 antenna, revealing optimal signal reception at higher elevation angles. This practical feature aligns with GNSS observations, which commonly impose a 10-15°cut-off elevation angle to mitigate multipath errors and atmospheric delays.

2.1.4.2 Front-End RF Receiver

The front-end, serving as the initial phase in signal processing, is pivotal in tasks like filtering, amplification, down-conversion, and quantization. The filtering stage, initiated

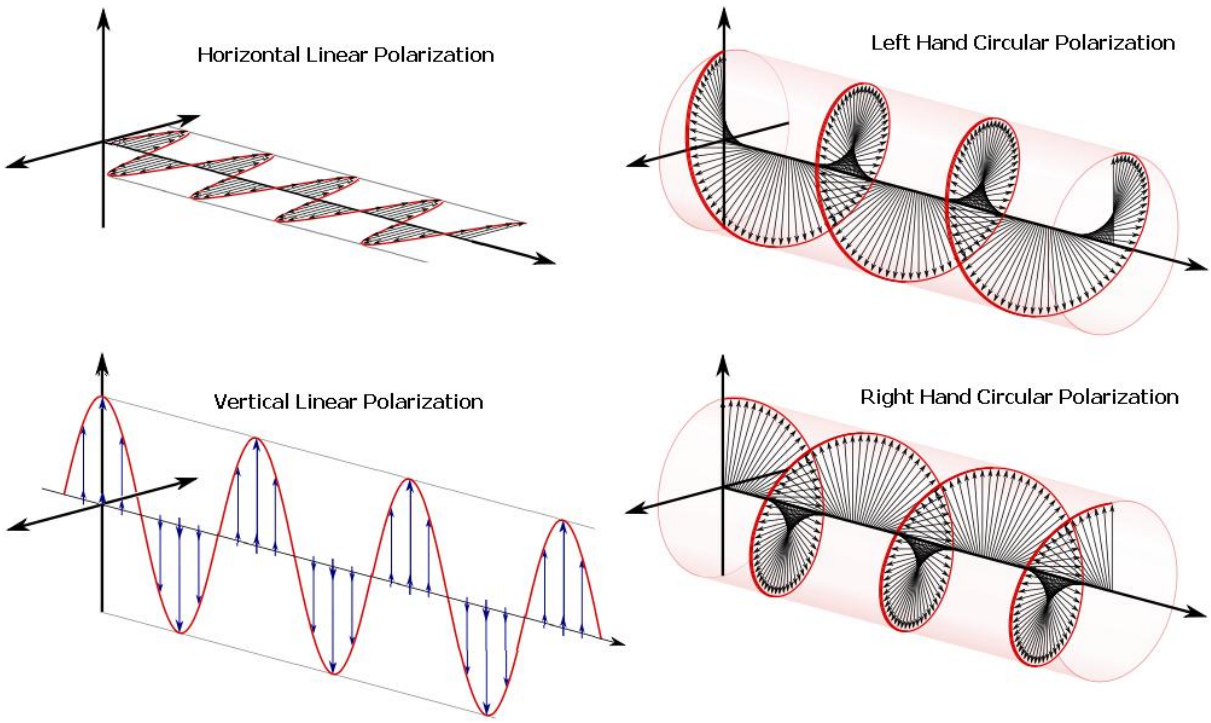

Figure 2.6: from top left to right: horizontal linear, LHC, vertical linear, and RHC polarization are depicted (Schmidhuber et al. 2022)

at the beginning and continuing after down-conversion, utilizes a band pass filter (BPF) to exclusively permit GPS L1 signals, ensuring the rejection of out-of-band signals (Borre et al. 2007). Antennas also contribute to frequency selection in an earlier stage, but since they are not ideal frequency selectors, subsequent amplification is essential to eliminate unwanted frequencies. A perfect filter would maintain the selected frequency while sharply cutting off anything outside the bandwidth. However, insertion loss occurs within the selected band, necessitating amplification after each filter stage.

Down-conversion is a critical step facilitating subsequent digital processing, where the radio frequency (RF) signal transforms into an intermediate frequency (IF) using a mixer and local oscillator (LO). The equation $|IF = RF - LO|$ demonstrates how the IF frequency is calculated. In figure 2.5, the LO is connected to the TXCO, which stands for Temperature Compensated Crystal Oscillator. TCXO is an oscillator that utilizes a crystal oscillator combined with a temperature compensation circuit to maintain

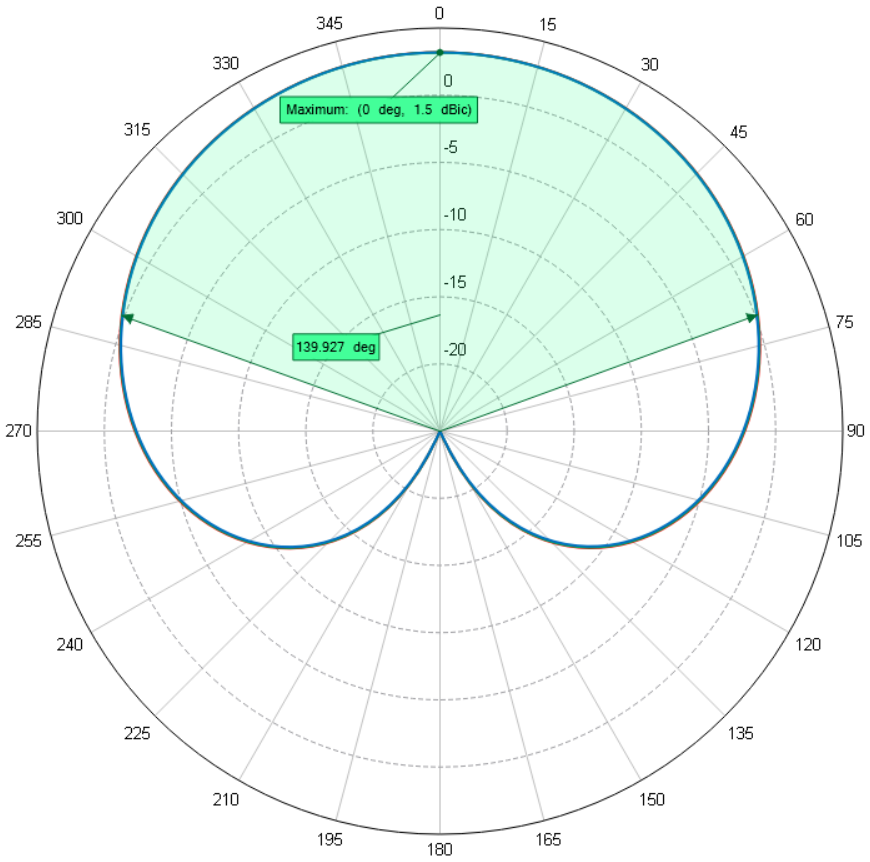

Figure 2.7: Antenna gain pattern for an Active GPS L1 antenna (Southwest-Antennas 2015)

frequency stability across varying temperatures. Down-conversion is essential for handling high-frequency RF signals, such as the 1.5 GHz frequency of GPS L1, transforming into IF more cost-effectively and less complexly, preserving signal information with minimal loss.

Quantization, the final step and a primary function of the front-end, transforms the continuous analog signal into a digital signal during this stage. Each sample is represented by 2 bits, one for magnitude and one for sign, resulting in the raw IF data set. This output undergoes post-processing using GNSS receiver solutions to derive valuable information for navigation and positioning (Texas-Instruments 2015).

2.1.4.3 Receiver

The receiver processes the raw IF digitized signal to extract navigation solutions. GNSS receivers exist in both hardware and software forms. It is important to note that almost all commercial GNSS receivers are hardware receivers, most commonly known as application-specific integrated circuit (ASICS) receivers. Hardware receivers offer swift and precise performance as standalone devices, but may lack adaptability due to limited reconfigurability. In contrast, software receivers rely on flexible and updatable algorithms, though they may have limitations based on the underlying hardware. Despite these differences, both hardware and software GNSS receivers follow the same general steps in finding a navigation solution: Acquisition, Tracking, Navigation data extraction, and finally, pseudo-range calculations.

The Acquisition step is the initial post-processing of the raw IF digitized dataset. This step identifies all visible satellites detected by the receiver, providing the frequency and code phase of the received signal for each satellite. Despite satellites broadcasting at the same carrier frequency, the frequency may experience a Doppler shift based on the relative motion between the satellite and the receiver. Code phase represents the time delay between transmission and reception by the GNSS receiver. The locally generated PRN code adjusts over time to synchronize with the PRN code received from the satellite, with the amount of time represented by the code delay depicted as tau in Figure 2.8.

As detailed in 2.1.1 (GNSS History and Basic Concepts), GNSS constellations consist of multiple satellites, each differentiated by their unique pseudorandom noise (PRN) ranging codes. With high auto-correlation and low cross-correlation properties, PRN sequences enable satellites to distinguish themselves within the constellation. Figure 2.9 illustrates an example of auto and cross-correlation for a C/A code.

The tracking stage involves tracking the frequency and code phase established in the acquisition stage. Carrier frequency tracking utilizes a delay lock loop, correlating locally generated PRN replicas with incoming signals. These replicas, categorized as too early,

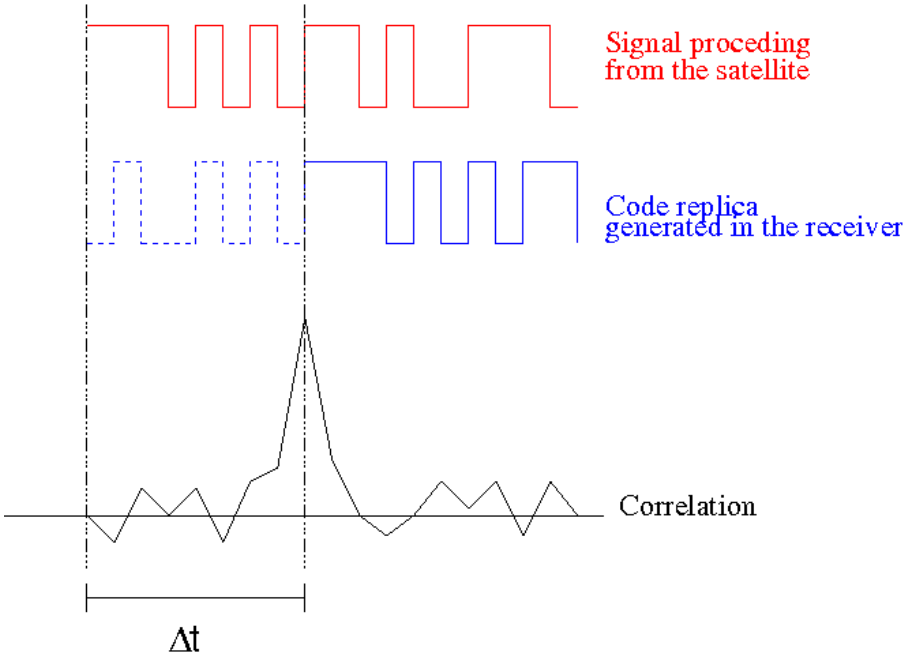

Figure 2.8: Code delay explanation graph (J. Sanz Subirana 2011)

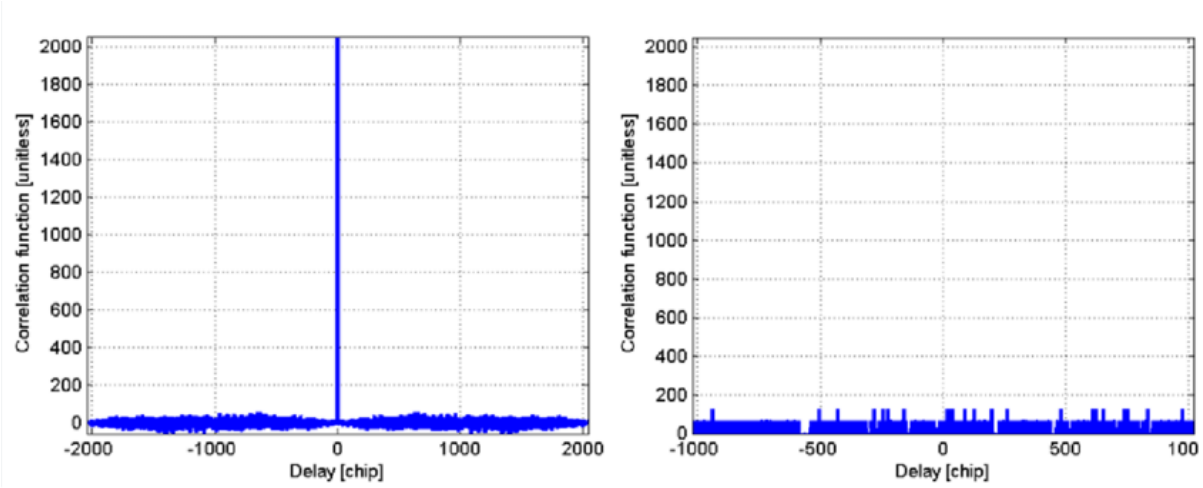

Figure 2.9: (Left) Auto correlation example for a C/A-code; (Right) Cross-correlation example for C/A-code (Susi 2017)

prompt, or late, guide the tracker to adjust and reach the prompt stage over time.

The final stages involve removing the C/A-code and carrier wave and initiating the decoding of the navigation message (refer to Figure 2.4). This message includes satellite

transmission time and ephemeris data, enabling the computation of pseudoranges crucial for determining the user's position.

2.2 Reflectometry

GNSS originally intended to deliver Positioning, Navigation, and Timing services. Over time, the remote sensing field has uncovered numerous indirect applications for GNSS signals. One such application is GNSS Radio Occultation (GNSS-RO), where low-Earth-orbit satellites capture signals from GNSS satellites to extract valuable data about the ionosphere. This technique is a crucial resource for weather prediction, contributing significantly to our understanding of atmospheric conditions and potential applications in tracking climate change (Hajj et al. 1994). Additionally, GNSS signals are employed in GNSS-Reflectometry (GNSS-R), which utilizes reflected signals to derive information about the reflective surface.

2.2.1 GNSS-R Basic Concepts

GNSS reflectometry is a technique for characterizing the Earth's surface by analyzing reflected GNSS signals. This passive sensing method utilizes the existing GNSS infrastructure, receiving direct signals from the GNSS constellation and signals reflected off the Earth's surface simultaneously. It is important to clarify that while GNSS operates as an active sensing technique, GNSS-R, on the other hand, solely utilizes existing GNSS signals without actively transmitting anything. Therefore, GNSS-R is considered a passive technique. The fundamental principle involves detecting parameter variations such as time delay, Doppler shift, signal power, and polarization between the direct and reflected signals using GNSS-R receivers. Geophysical information such as sea level, snow height, and soil moisture can be estimated using the aforementioned parameters. It is essential to acknowledge that multiple parameters may coexist simultaneously, necessitating more

sophisticated models for accurately assessing individual parameters. For instance, when evaluating soil moisture, it is imperative to consider factors such as vegetation, surface roughness, soil texture, and temperature.

As evident in figure 2.10, the reflection point changes depending on the position of the receiving antenna and the GNSS satellites. Note that this figure only illustrates one GNSS satellite whilst, in reality, the receiver is receiving signals from multiple satellites at the same time. The reflectometry geometry can become more complex depending on the location and motion of the receiver. This concept will be further explored later in the chapter in section 2.2.4.2

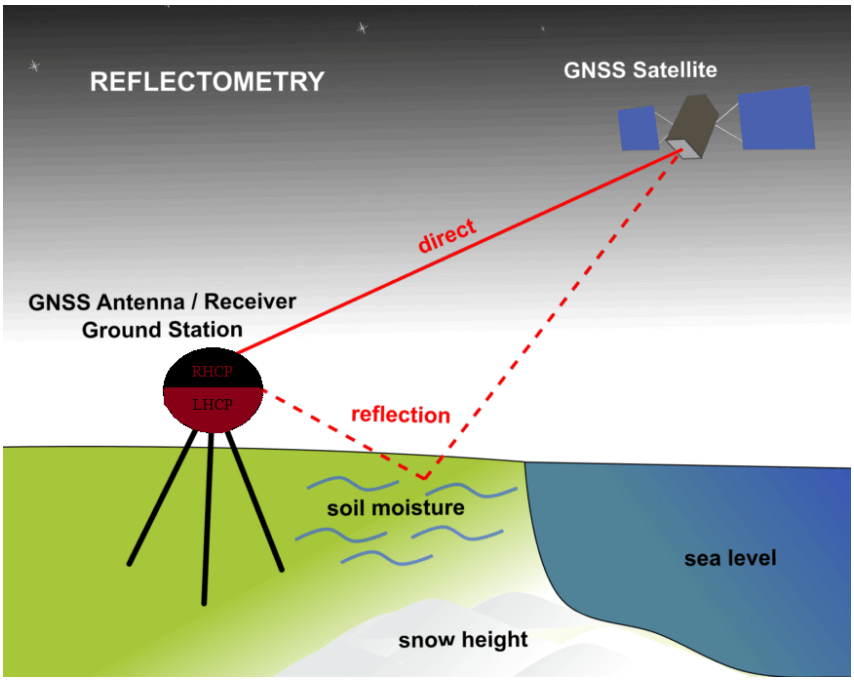

Figure 2.10: Principle of GNSS reflectometry (Sehnal n.d.)

2.2.2 History

In 1988, researchers initially introduced the idea of using Global Navigation Satellite System (GNSS) signals in reflectometry applications(Hall et al. 1988), now known as GNSS-R. Subsequently, two distinct GNSS-R methodologies emerged: Interferometric GNSS-R (iGNSS-R) and Conventional GNSS-R (cGNSS-R).

The iGNSS-R concept traces back to 1993, when introduced by the European Space Agency (ESA). This approach, known as PARIS (Passive Reflectometry and Interferometric System), proposed using passive instruments to perform ocean altimetry measurements in directions other than nadir. This technique compares the direct signal from a satellite with the same signal once it is reflected off the ground to find cross-correlation (Martin-Neira 1993).

Conversely, cGNSS-R existed in 1996 when NASA outlined using GPS signals to determine ionospheric delays over the ocean. This technique integrates a GPS receiver and a downward-pointing antenna on satellites carrying single-frequency altimeters. This method compares the reflected satellite signal with a clean, locally generated code replica, resulting in a higher signal-to-noise ratio (SNR) than iGNSS-R (Katzberg et al. 1996).

Regarding susceptibility to RFI and satellite cross-talk, iGNSS-R can be affected by RFI in both direct and reflected signals (Onrubia et al. 2016), potentially leading to cross-correlation peaks from multiple visible satellites (Pascual et al. 2016). In contrast, cGNSS-R is susceptible to RFI only in the reflected signal and displays peaks corresponding to the correlated code.

In post-processing, iGNSS-R does not require code generation at a specific frequency, and the Doppler effects of both direct and reflected signals are nearly identical. On the other hand, cGNSS-R involves the generation of a code at a precise frequency and necessitates careful consideration of Doppler effects. Finally, hardware requirements vary significantly. iGNSS-R typically employs complex systems with large arrays and steerable beams, while cGNSS-R may offer a more streamlined and hardware-efficient approach (Onrubia-Ibáñez 2020).

2.2.3 State-of-the-Art GNSS-R Missions and Applications

The initial phases of GNSS-R experiments were predominantly carried out on airborne platforms, frequently occurring within aircraft, as vital proof-of-concept trials. These in-

struments underwent significant advancements as time progressed, increasing complexity and diversifying their uses. This review presents the evolution of GNSS-R instrumentation, highlighting key milestones in its history, from its early airborne missions to later deployments in space missions, and showcasing how it has expanded its scope of applications in table 2.2.

2.2.3.1 Airborne

In 1997, a series of aircraft experiments used an innovative payload that would subsequently be known as the Serial Delayed Mapping Receiver (SDMR). These experiments incorporated a dual-input receiver featuring customized software, enabling tracking of up to six satellites. The receiver configuration included a zenith-oriented RHCP antenna for direct signal reception and a Left-Hand Circularly Polarized (LHCP) antenna for collecting reflected signals. Over the next few years, this instrument examined ocean surface wind speeds (Garrison et al. 2000) and soil moisture levels (Masters et al. 2000). Later in early 2000s, a modified GPS receiver was made for reflectrometry purposes (Lowe et al. 2000) for ocean altimetry solution on board an aircraft with centimetre accuracy (Lowe et al. 2002). In 2004, Eddy became the first software-based GNSS-R instrument for sea height and mean sea level determination applications (Ruffini et al. 2004). In 2007, the GPS Open Loop Differential Real-Time Receiver (GOLD-RTR) became the first system to calculate Delayed Doppler Maps (DDMs) in real-time (Nogues-Correig et al. 2007). This system stood out for its practical use of both RHCP and LHCP with nadir-looking antennas, which played a crucial role in estimating Ocean Permittivity (Cardellach et al. 2011). In 2012, within the LEiMON project, a GNSS-R instrument was placed in the heart of a crop field, elevated 25 m above the ground. This experiment employed both LHCP and RHCP nadir antennas. The significance of this experiment lies in its focused application on agriculture, particularly in the context of assessing soil moisture (Egido et al. 2012).

2.2.3.2 Space Missions

The UK's Disaster Monitoring Constellation Satellite (UK-DMC) marked a significant achievement as the first satellite to capture reflected GNSS signals from space. Its primary role is to provide disaster area imagery for relief agencies worldwide. In 2003, a GNSS-R payload called Space GNSS Receiver (SGR) was added as an extra feature. SGR included three antennas: two for regular GPS navigation and a third specialized antenna pointing downwards to capture surface-reflected signals. The payload can process the data in real time, but it is also possible to download the raw intermediate frequency (IF) signal for post-processing (Gleason et al. 2005). This mission was very successful since it proved the feasibility of retrieving reflected signals from various terrains, including the ocean, ground, and ice. The data gathered with the UK-DMC has been used in various applications, most notably in estimating ocean wind direction and velocity (Clarizia et al. 2009).

In 2014, the UK launched TechDemoSat-1 (TDS-1), which featured a modified version of the SGR known as SGR-Remote Sensing Instrument (SGR-ReSI). SGR-ReSI can receive signals from GPS and Galileo on L1, L2, L5, and E5ab. It boasts a higher sampling rate, increased storage capacity, and an automatic gain control (AGC) feature. Notably, both direct and reflected tracking functionalities are reprogrammable, and it offers continuous Delayed Doppler outputs. The primary purpose of this mission was to serve as a technology demonstration for the Cyclone Global Navigation Satellite System (CYGNSS) mission (Kramer 2013).

In December 2016, NASA launched the CYGNSS mission to measure wind speeds over the Earth's oceans. Comprising a constellation of eight micro-satellites in Low Earth Orbit (LEO), this system guarantees nearly uninterrupted monitoring of the planet's surface, specifically the critical latitude band for tropical cyclone formation and movement. This system offers a revisit time of seven hours, with a median revisit time of three hours.

CYGNSS represents NASA's first mission to use a GNSS-R payload, a passive remote sensing technique, marking a pioneering shift from traditional microwave scatterometry.

This novel approach offers numerous advantages, with a primary distinction being that traditional scatterometry relies on a higher-frequency microwave band, predominantly the Ku (IEEE-Std 1984). However, these higher frequencies are susceptible to signal degradation in intense precipitation and severe weather conditions. On the other hand, GNSS signals operate within the lower microwave band, the L band, making them highly reliable under a wide range of weather conditions (PO.DAAC 2017).

CYGNSS's primary scientific instrument is Delayed Doppler Mapping Instrument (DDMI). Illustrated in figure 2.11, the DDMI comprises three antennas: one zenith antenna serving the dual purpose of navigation and used as a coherent reference for the encoded GPS signal, and two nadir-facing antennas, both circularly polarized (both LHCP and RHCP), designed to capture reflected signals. Each of these antennas features its own dedicated front-end processors. Furthermore, the system integrates a GNSS receiver, which generates navigation solutions and provides tracking and navigation data to the DDM processors responsible for producing Delayed Doppler Maps (DDMs).

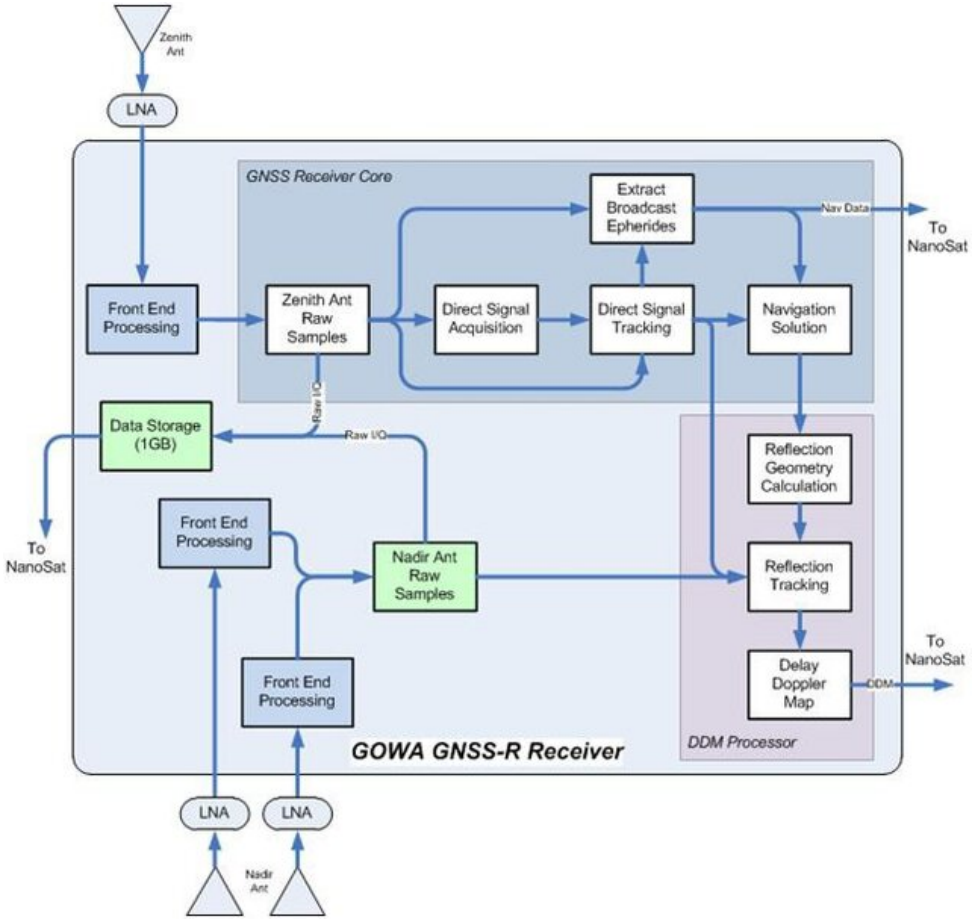

Figure 2.11: CYGNSS Delay Doppler Map instrument architecture (Ruf et al. 2014)

One notable capability of CYGNSS is its ability to generate four Delay Doppler Maps (DDMs) simultaneously onboard while transmitting the raw IF data for subsequent ground-based processing. The formation of DDMs follows a conventional GNSS-R method, which involves cross-correlating the received signal with a locally generated replica, accounting for time delays and Doppler shifts. Additionally, an open-loop tracking algorithm enhances the processing of DDMs by predicting the position of the specular reflection point, leveraging the known position of the payload (Razal et al. 2014). Table 2.3 summarizes the evolution of GNSS-R instrumentation, covering its progression from ground-based applications to airborne missions and its integration into space missions, as discussed in the preceding paragraphs.

Name	**Year**	**Bands**	**Based**	**Primary Application**
SDMR	1997	L1	Aircraft	Wind Speed & Soil Moisture
Modified TurboRogue	2000	L1/L2	Aircraft	Ocean Altimetry
SGR UK (DMC)	2003	L1/L2	Spacecraft	Wind Speed
EDDY	2004	L1	Aircraft	Sea Mean Level & Sea Height
GOLD-RTR	2007	L1	Aircraft	Ocean Permittivity
LEiMON	2012	L1	Ground	Soil Moisture & Biomas
TDS-1 (SGR-ReSI)	2014	L1/L2/L5	Spacecraft	Wind Speed
CYGNSS (DDMI)	2016	L1/L2	Spacecraft	Wind Speed

Table 2.2: Summary of state-of-the-art GNSS-R missions discussed in section 2.2.3

2.2.3.3 UAV Missions

With the increasing interest in GNSS-R applications, a growing focus has been on developing payloads for UAVs (Unmanned aerial vehicles). Nowadays, UAVs serve as a practical and cost-effective testing ground for new GNSS-R instruments, representing an initial step in the technology readiness level before transitioning to more complex aircraft or space-based platforms. Several noteworthy projects exemplify this trend.

One such project was undertaken by a research group from Kyushu University in Japan in early 2019. They devised a low-cost GNSS-R altimetry system integrated into a UAV, achieving an impressive accuracy of 0.01 m when a sufficient number of GNSS satellites

were detectable. It is worth noting that they relied only on an LHCP antenna for the nadir antenna (Ichikawa et al. 2019). In 2019, an Italian research group conducted a feasibility study to explore the potential of a UAV-based GNSS-R payload for water detection, specifically for flood monitoring applications. Their investigation revealed promising results, as they could detect small water surfaces with a resolution in tens of metres and an impressive 92% accuracy rate (Imam et al. 2020).

2.2.4 Reflectrometry Observables

A critical distinction between direct and reflected GNSS signals lies in their signal strength, polarization, and variations in code delay and Doppler shift. The main observables of a reflected signal, including its delay, Doppler shift, and received power, can be measured from the received signal. As previously highlighted in this chapter, GNSS signals, upon reaching the Earth's surface, already fall below the thermal noise floor, as depicted in Figure 2.2. This diminished power of reflected GNSS signals poses a heightened detection challenge for standard GNSS receivers. To address these challenges caused by the weak reflected signals, a strategy involves leveraging the direct signal's frequency and code phase information to estimate the corresponding parameters for the reflected signal. This aids in the acquisition and tracking of these weakened reflections. Besides the power loss, reflected signals undergo a polarization shift upon impact with a surface, transitioning from RHCP to Left-Hand Circular Polarized (LHCP). The degree of polarization change hinges on the surface's roughness, dielectric constant, and the satellite elevation angle. In reflectometry, a primary hurdle arises in capturing exceedingly weak reflected signals, which may be challenging to distinguish from background noise. The low power of the reflected signals underscores the complexity of detecting and interpreting reflected signals in GNSS-reflectometry applications.

2.2.4.1 DDM and Delayed Waveform

The core concept explored in GNSS-reflectrometry is comparing direct and reflected GNSS signals. These differences manifest in three main aspects: reduced signal power, temporal lag, and frequency variation, depending on the reflective surface's characteristics. Two of these aspects are captured within delayed waveforms (DWFs), which offer a visual representation of signal power as a function of temporal delay. Furthermore, a three-dimensional depiction of the DWF, known as the Delayed Doppler Map (DDM), portrays the DWF's variations with respect to frequency. In this thesis, the DWFs and DDMs are generated with the cGNSS-R process, where received reflected signals are cross-correlated with a local replica across a specific delay and frequency range. Figure 2.12 shows examples of both DWF and DDM for reflected and direct signals received from PRN 28 by the CYGNSS mission.

In Figure 2.12, a clear distinction is observed between the direct and reflected GNSS signals. The direct signal exhibits a substantial correlated power of 5e13, notably stronger than its reflected counterpart, which registers a significantly lower power level, around one-tenth of the direct signal's strength. The direct signal's coherence is evident, manifesting as a circular shape in the plot. In contrast, the reflected signal displays a distinct incoherent element as a horseshoe shape. This incoherence is primarily attributed to the influence of strong winds over the ocean. In scenarios characterized by calm water bodies or smooth, vegetation-free surfaces, such as beaches or grass fields, the coherent element becomes more pronounced, and the horseshoe-shaped incoherence typically associated with turbulent wind conditions is absent.

2.2.4.2 Specular Reflection Point

In a practical study of GNSS-R products like DWF and DDM, the first crucial step involves pinpointing the position of the reflection surface, which is referred to as the specular point. This specular point can be precisely determined by calculating the shortest path between

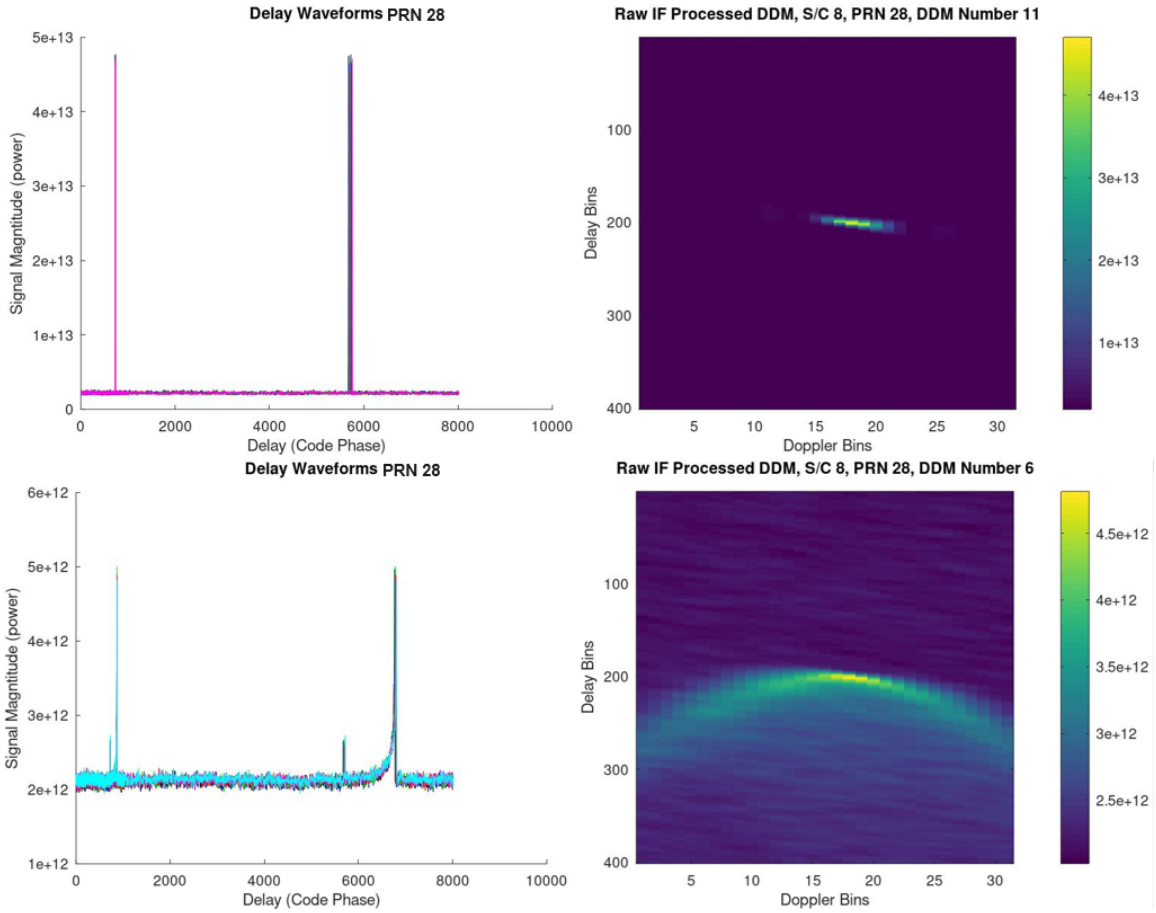

Figure 2.12: Ocean reflection CYGNSS data-set. Top from left to right, DWF and DDM of PRN 28 captured by the zenith navigation antenna onboard CYGNSS. Bottom from left to right, DWF and DDM PRN 28 captured by the nadir science antenna aboard CYGNSS. These graphs were generated by the author using the CYGNSS code and data-set.

the satellite's location (for instance, a GPS satellite), the receiver's position (GNSS-R payload onboard a UAV), and the specular point on the Earth's surface. At this specular point, the angles of incidence and scattering are equal, satisfying Snell's law. Figure 2.13 illustrates the geometry of a specular point. It should be noted that this explanation of the specular point assumes a flat surface, while more complex surfaces may have multiple specular points.

A MATLAB code (Gebre-Egziabher et al. 2009) was used to find the specular points. The script requires the ECEF coordinates for the GNSS satellite, which can be obtained from NASA's Archive of Space Geodesy Data (NASA-CCDIS 2023). ECEF, abbreviated

for Earth-centered, Earth-fixed, is a Cartesian coordinate system that employs X, Y, and Z measurements from the Earth's center of mass to represent the location of an object. These coordinates are provided for every five minutes, so if only a portion of a five-minute data collection is being analyzed, only one coordinate of the satellite can be used. The receiver coordinates are also given in ECEF; the UAV does not provide these coordinates. The code uses a for loop to iterate the constraint of Earth's surface to the shortest path between the satellite and the receiver. The outputs are provided in latitude and longitude of the specular locations. Note that this MATLAB code uses the World Geodetic System 84, also known as WGS84, which uses a reference ellipsoid that approximates the shape of the Earth.

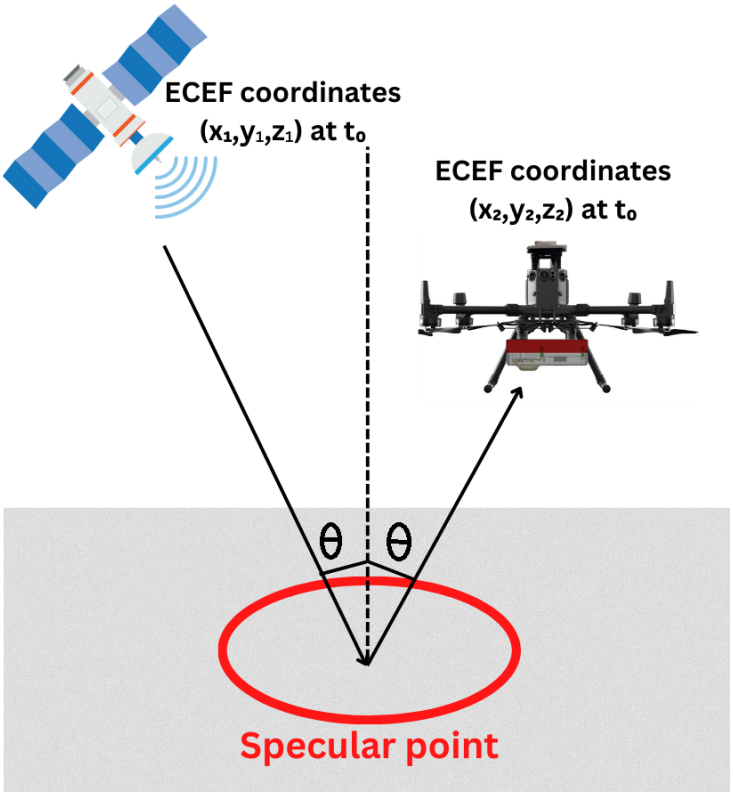

Figure 2.13: Illustration of the specular point

Chapter 3
Design of the GNSS-R Payload

In Chapter 2, the discussion centred around GNSS-R, a remote sensing technique that capitalizes on freely available and omnipresent GNSS signals and infrastructure. This approach proves helpful in extracting diverse geophysical properties, including altimetric heights, soil moisture, and surface roughness, an essential parameter in examining the Earth's surface.

Successful space-borne GNSS-R missions, exemplified by CYGNSS, do exist. However, their high costs and limited spatial resolution render them less than ideal for localized applications, particularly when monitoring small farms that require higher precision. An alternative approach involves integrating a GNSS-R payload onto a drone using COTS technology, offering enhanced spatial resolution. A comparison between space-borne methods and the proposed drone-based method is provided in Table 3.1. This comparison is not intended to directly contrast a space-grade payload with a UAV-based payload but rather to underscore the distinct applications of each. Space-grade payloads excel in tasks such as measuring surface wind speed during cyclones since they operate from Earth's orbit but struggle with more localized areas due to their limited spatial resolution.

	Space-Borne	**UAV based**
Spatial Resolution	Low e.g. CYGNSS's spatial resolution was verified at 15 km	High Depending on height can be between 50 to 200 m
Costs	High e.g. CYGNSS mission $100 million	Low Using COTS design $< $5000

Table 3.1: Space-born versus UAV-based payload and their temporal, spatial resolutions as well as their costs

3.1 Payload Objective and Requirements

The primary objective of this research is to design, build, and validate a GNSS-R payload tailored for a UAV platform. The design and assembly of the payload are guided by mission requirements and the UAV's compatibility. A set of requirements derived from past reflectometry literature and operational needs has been established to achieve this primary objective, detailed in the list below.

List of Requirements:

1. The GNSS-R receiver shall measure the signal strength of both RHCP and LHCP signals.

2. Payload must operate for a minimum 20-minute flight.

3. The total mass of the payload shall be less than 5kg, including mounting property.

4. The dimension of the receiver enclosure should not interfere with any of the UAV's sensors or propellers.

Requirement 1 is derived from the latest GNSS-R literature, setting a scientific benchmark based on state-of-the-art architecture. Requirement 2 stemmed from the science team requesting 10-15 minutes of data to support their soil moisture modelling algorithms. Considering the potential flight time from take-off to desired locations, which could be up to 2-3 minutes sometimes, a 20-minute flight duration was deemed necessary. Limitations influence requirement 3 in commercially available UAVs, and the science team sets specific timing constraints. Meanwhile, Requirement 4 is operational and safety-oriented, ensuring that flights are conducted securely and consistently.

3.2 Payload Architecture

The GNSS-R design resembles the Delay Doppler Map Instrument used in NASA's CyGNSS mission Figure 2.11. This payload can collect three Radio Frequency (RF) streams, comprising one from the zenith-facing antenna (RHCP) and two from the nadir-facing antenna (RHCP and LHCP). The low noise amplifier (LNA) integrated into the antennas receives power through the bias-tees. An attenuator is positioned between the front-end's (FE) channels and the antennas to meet the FE's automatic gain control (AGC) thresholds. The FE is linked to the onboard computer for configuration, data collection, and storage. The onboard lithium-ion battery pack powers all electrical components (see figure 3.1).

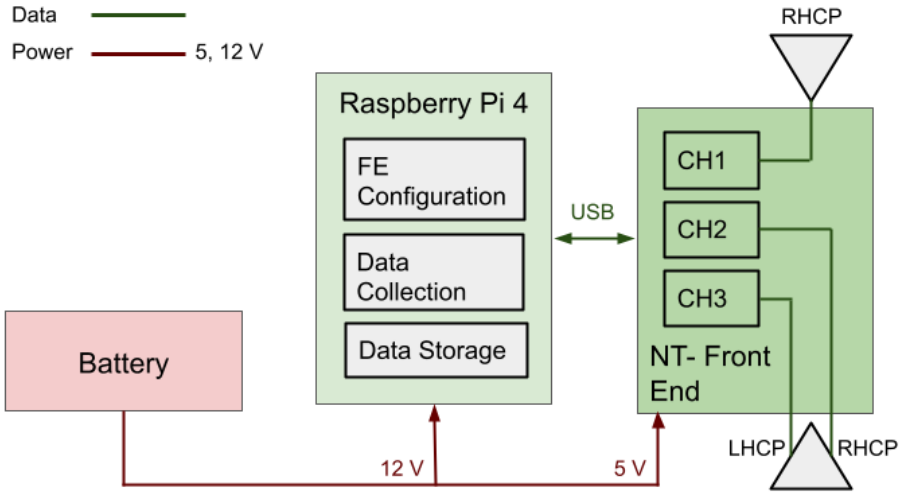

Figure 3.1: Overall architecture of the payload

3.3 Hardware and Equipment Overview

The hardware components employed in the design of this payload are exclusively commercial off-the-shelf (COTS) units. A comprehensive inventory of these components, including their respective models and manufacturers, is provided in Table 2.2. This section will offer a detailed exposition of the functionality of each component and how their integration contributes to fulfilling the payload's requirements.

Component	Model	Manufacturer
Antennas	42G1215RL	ANTCOM
Bias-tee	ZFBT-4R2G+	Mini Circuits
Attenuator	FW-10+	Mini Circuits
Front-end	NT1065	NTLab
On-Board-Computer	Pi 4 Model B	Rasberry Pi
Battery	Lithium Ion	Amazon Vendor
Payload mounting to UAV	Skyport	DJI
UAV	Matrice 300 RTK	DJI

Table 3.2: GNSS-R COTS components

3.3.1 Antenna

The antenna enclosure incorporated a built-in LNA, which generates a 33 dB gain. It is specifically designed for GNSS avionics-grade operations and can receive both L1 and L2 frequencies. The payload features two identical antennas, one positioned in the nadir direction and the other in the zenith direction. These antennas can simultaneously receive right-hand circular polarization (RHCP) and left-hand circular polarization (LHCP) signals, effectively performing the role of two antennas in one. Specifically, the dual-polarized functionality of the nadir antenna enables the reception of both RHCP and LHCP signals reflected from the ground. Conversely, the zenith antenna exclusively utilizes the RHCP output, with the LHCP output connected to an RF termination since all GPS signals are RHCP. To ensure optimal RF performance, any unused ports are appropriately terminated with a 50 Ohms load (ANTCOM 2017). A comparison was conducted among

Figure 3.2: ANTCOM antenna picture (ANTCOM 2017)

three commercial RHCP/LHCP GNSS antennas to identify the most suitable antenna

for the payload's application. The first antenna considered was the European Antennas passive antenna FPA8-1.6RL/1563, boasting a gain of 7.25 dBic and a mass of 190 grams. The second option was Teleirbit's GPS Dual Circularly Polarized Antenna, an active antenna with an impressive overall gain of 38 dBic and a mass of 485 grams. Lastly, the ANTCOM's 42G1215RL was examined, featuring an overall gain of 33 dBic and a mass of 191 grams. This comprehensive comparative analysis aimed to identify the antenna that aligns most effectively with the payload's specific requirements and operational considerations. Ultimately, the ANTCOM antenna was selected, as it fulfills the criteria of being an active antenna but also matched the mass and volume requirements, making it the optimal choice for integration into the payload system.

3.3.2 Bias-Tee

Bias-Tee circuits are commonly employed to split signals to power active antennas, which differ from passive antennas due to integrating a low noise amplifier (LNA) within their circuitry. While some GPS receivers include this bias circuit within their front-end design to provide power, the chosen NT1065 Front-End lacks this feature. The bias-tee, a straightforward circuit with three connection points – the antenna, the front-end, and a DC power source plays a crucial role in addressing this power supply requirement. It allows the transmission of DC voltage to the antenna while preventing it from entering the front-end. Simultaneously, it ensures that RF frequencies can flow unimpeded from the antenna to the front-end. The selected bias-tee is well-suited for delivering the necessary voltage to power the LNA and offers a 50 ohm resistance that matches the front-end, antenna, and coaxial cables. Moreover, its operational range, from 10 to 4200 MHz, ideally accommodates GPS L1 signals at 1575 MHz (Mini-Circuits 2022b).

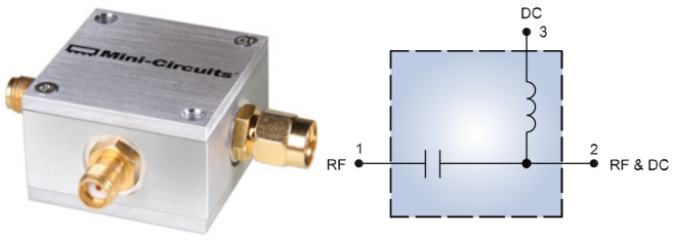

Figure 3.3: Bias-tee picture and electrical schematics (Mini-Circuits 2022b)

3.3.3 Attenuator

An attenuator, in contrast to an amplifier, is a passive device that reduces the amplitude or power of a signal without significantly distorting its waveform. While adding such a device to the RF line may seem counterproductive, particularly considering the weak nature of GNSS signals discussed in Chapter 2, it serves a crucial purpose. In the case of the NT1065, an AGC is utilized to address the fading propagation, characterized by variations in the amplitude of the received signal. Users can set upper and lower thresholds, with options ranging from -49 dBm to -40 dBm. During hardware testing, the AGC state consistently indicated that the input signal was "higher than regulating range". To rectify this, a variable attenuator was introduced into the line to determine the minimum attenuation required to bring the input signal power within the regulation range, which was found to be around 9 dB. Subsequently, a fixed attenuator at 10 dB, the closest commercial-off-the-shelf (COTS) option, was incorporated into the line to optimize signal performance (Mini-Circuits 2022a). Note that the active antenna still provides around 23 dB of gain to the received signal even after introducing an attenuator to the line.

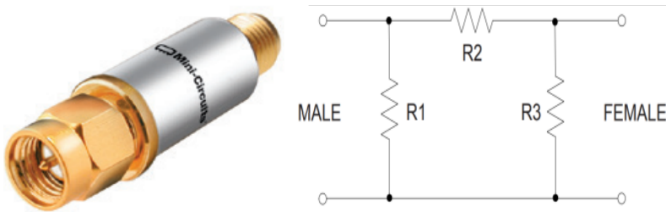

Figure 3.4: Attenuator picture and electrical schematic (Mini-Circuits 2022a)

3.3.4 Front-End

Figure 3.5 illustrates the front-end structure for one channel in the NT1065 receiver. Beginning at the top left of the front-end structure, the filtering stage employs a Band Pass Filter (BPF) to reject out-of-band signals, ensuring only GPS L1 signals, centring at 1575.42 MHz, can pass through. The three channels were set to an IF passband of 27.1 MHz. However, it's essential to recognize that bandpass filters are not perfect squares and lack an exact cutoff frequency. Instead, they feature a "transition band" where signal power decreases rapidly as you transition from the pass to the stop band frequencies. The IF Signal filtering continues through various stages to optimize signal acquisition, with a band-stop filter positioned immediately after the down-conversion stage (NT-Labs 2019).

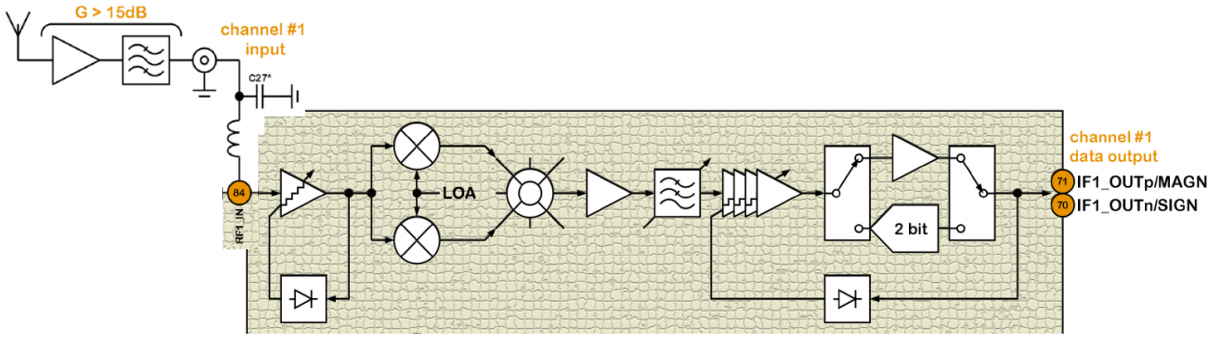

Figure 3.5: NT1065 receiver's front-end electrical schematic (NT-Labs 2019)

The local oscillator (LO) frequency can be adjusted by modifying one of the following parameters: the reference clock frequency (f_{TCXO}), the Phase-Locked Loop (PLL) divider ratio (N), or the reference clock divider ratio (R). Equation 3.1 depicts the relationship between these three parameters and the LO frequency (Ferreira et al. 2018). For the experiments conducted in this thesis, the LO frequency is consistently configured at 1590 MHz. Consequently, this setting establishes the intermediate frequency (IF) at 4.58 MHz.

$$LO = f_{TCXO} * N/R \tag{3.1}$$

3.3.5 Onboard Computer

The onboard computer, a Raspberry Pi 4, was used to configure the front-end, run the sampler for data collection, and store flight data on an SD card for subsequent post-processing. The Raspberry Pi 4's Linux platform hosted the NT lab GUI for front-end configuration and the sampler GUI for data collection. Before each flight, the front-end would get configured, the sampler would be initiated, and the flight would commence. Figure 3.3 shows the calculation done for the memory budget. To meet these memory requirements, a 1 TB SD card was selected for the Raspberry Pi 4, guaranteeing the capacity to accommodate data from ten to fifteen 20-minute-long data collection sessions daily without immediate data transfer.

	Data Rate (MB/s)	**Seconds**	**GB**
Raw IF for one channel	16.7	1200	20.04
Total required for 3 channels	16.7	1200	60.12
Operating system allocation	N/A	N/A	50
Minimum total memory required	N/A	N/A	110.12

Table 3.3: Memory budget calculation table

3.3.6 UAV

The UAV of choice for data collection in this study is the DJI MATRICE 300 RTK, selected after conducting a thorough trade study comparing it to other drone options. This decision was based on its user-friendly operation, suitability for diverse field campaign locations, and safety features, including obstacle avoidance sensors and intelligent flight modes. Furthermore, the drone's inherent weather resistance enhances its resilience. Complementing this, the payload design encloses the electronics for weather protection, with the avionics-grade antennas remaining exposed. The subsequent sections will detail the factors influencing the drone's selection and offer insights into its operational aspects. Figure 3.6 displays the DJI Matrice 300 RTK with the payload attached underneath and the zenith antenna mounted on top.

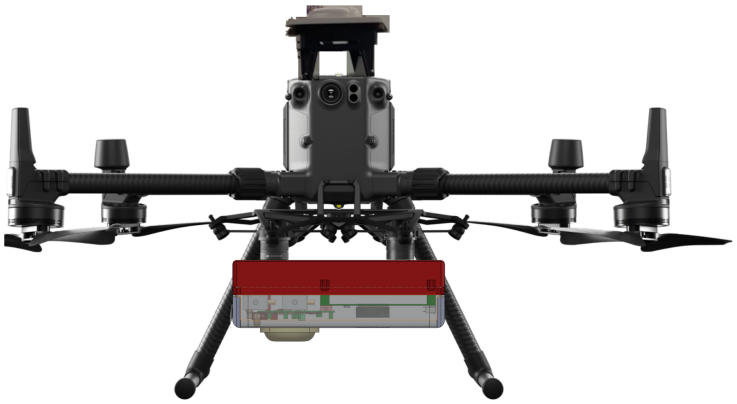

Figure 3.6: UAV payload integration

The mass budget represents a pivotal consideration influenced by the UAV selection. In the case of the DJI Matrice 300 RTK, the trade-off between flight time and allowable payload mass is shown in figure 3.7. For an optimal 30-minute flight duration, the payload weight must remain below 2.7 kilograms. It is worth noting that this value represents the upper limit of permissible payload's weight since, in the ideal scenario, achieving at least two complete flights before a battery change is desirable.

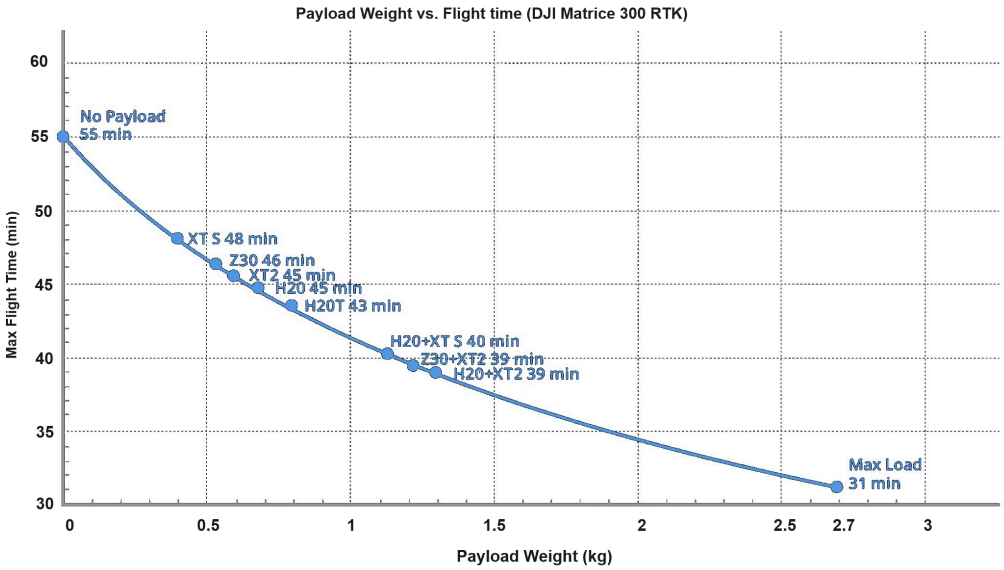

Figure 3.7: Payload Weight versus Flight time (Drone company 2023)

3.3.7 Payload mass budget

The payload is seamlessly integrated with the UAV using DJI's Skyport dual gimbal connectors, which offer a maximum load capacity of 1.2 kilograms. This integration significantly reduces the allowable payload weight, from 2.7 kilograms to 1.2 kilograms, reducing the overall mass budget. However, it brings about several benefits, including simplifying operations by allowing the payload to be attached to the UAV, like setting up a camera. Additionally, this setup helps minimize vibrations, thanks to the gimbal's built-in vibration absorption, enhancing the practicality of the data collection process. Table 3.4 shows the total mass budget calculations. As the mass budget slightly exceeded the 1.2 kg limit, an extra security measure was implemented for the payload. It was securely fastened to the gimbal's structure safety tether; refer to Figure 3.8.

Component	**Weight (grams)**	**Percentage of total weight**
Front-end	27.42	2
On-board-computer	45	3
Two GNSS antennas	382	30
Power system (battery, wires)	250	19
BNC cables	50	4
Enclosure 3D printed	300	23
Bias-tees	210	16
Attenuator	30	2
Total Payload Weight (grams)	**1294.42**	N/A

Table 3.4: Mass Budget Calculation Table

The payload components were modelled using SOLIDWORKS, a computer-aided design software, to facilitate adjustments for optimal mass distribution and balance within the box (see Figure 3.9). Adjustments were made since the nadir-looking antenna and the bias tees, accounting for up to 31 percent of the total mass, are positioned off-center. To achieve a more centralized center of mass within the X-Y plane of the payload, the battery system and printed circuit boards were intentionally moved off-center on the opposite side.

Figure 3.8: UAV and payload, just before the flight, during configuration

3.4 Payload Testing

Throughout the design and construction of the payload, a testing protocol was implemented at various stages to confirm its anticipated functionality. The testing procedure involved independently isolating and testing each component to assess its reliability. The entire payload configuration was evaluated before initiating flight campaigns to ensure its overall operational integrity.

3.4.1 Antenna Testing

This test aimed to confirm the effective functioning of the antenna in capturing GPS L1 signals. The experiment specifically isolated the antenna from other payload components. A commercial GNSS receiver, NovAtel's PwrPak7, was employed to execute the test. This receiver facilitated the evaluation by providing power to the antenna's low-noise amplifier and tracking all current and upcoming GNSS satellite signals, including GPS, GLONASS, Galileo, and BeiDou. The PwrPak7, with its 5 VDC antenna low-noise amplifier power output and a maximum current of 200 mA, met the requirements for

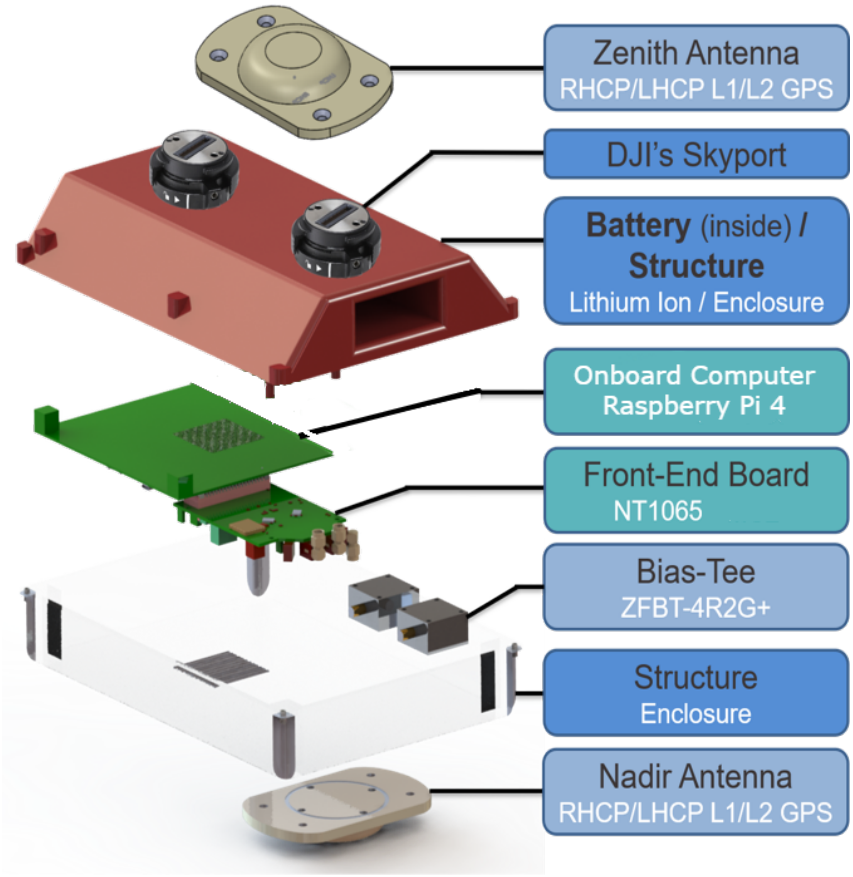

Figure 3.9: Exploded view: SolidWorks model of payload

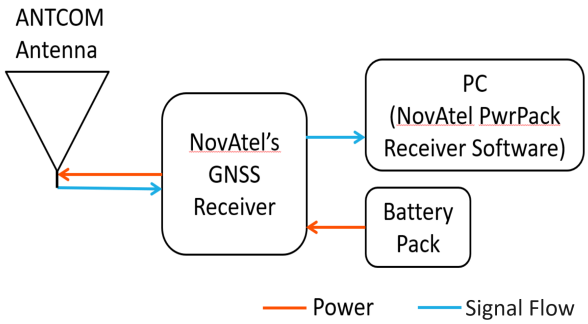

Figure 3.10: ANTCOM antenna testing configuration

the ANTCOM antenna. The real-time tracking capability within the computer software further streamlined the testing process.

The test configuration, illustrated in Figure 3.10, involved NovAtel's Antenna receiving signals and generating a navigation solution. This solution was then visualized using NovAtel software on a PC. The receiver, powered by a battery pack, not only processed the signals but also supplied power to the ANTCOM antenna. This entire test was conducted on York University's campus, utilizing a simple tripod to support the antenna.

The outcomes of the test are presented in Figure 3.11, which includes a screenshot of the NovAtel software displaying two skyplots featuring different GNSS constellations and their respective detected satellites. Additionally, a position panel provides information on the receiver's location, along with a status report detailing elements such as the temperature of the TCXO and the power levels supplied to the antenna. Notably, the receiver successfully identified all six GPS satellites (PRNs 2, 5, 12, 20, 25, and 29), affirming the effective functioning of the antennas used in the test.

3.4.2 Bias-Tee Testing

For an active antenna to function, voltage injection through its coaxial cable is required. However, since the front-end (NT1065) cannot provide DC power, a bias-tee is employed to introduce the necessary voltage into the line. The bias-tee ensures that the voltage travels exclusively to the antenna, preventing it from reaching the front-end. The testing

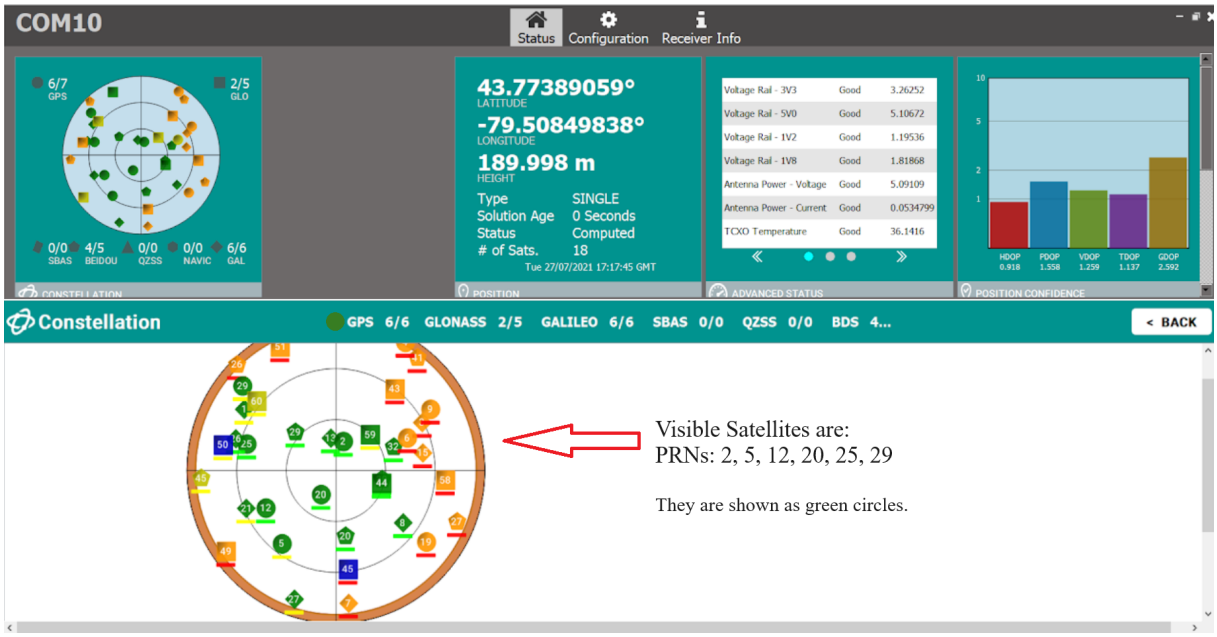

Figure 3.11: NovAtel PwrPack software results

procedure is straightforward: a DC power supply delivers 5 V to the DC port of the front-end. Subsequently, a multimeter is utilized to measure the voltage at the RF+DC port (directed to the antenna) and the RF port (connected to the front-end). The experimental setup is illustrated in Figure 3.12.

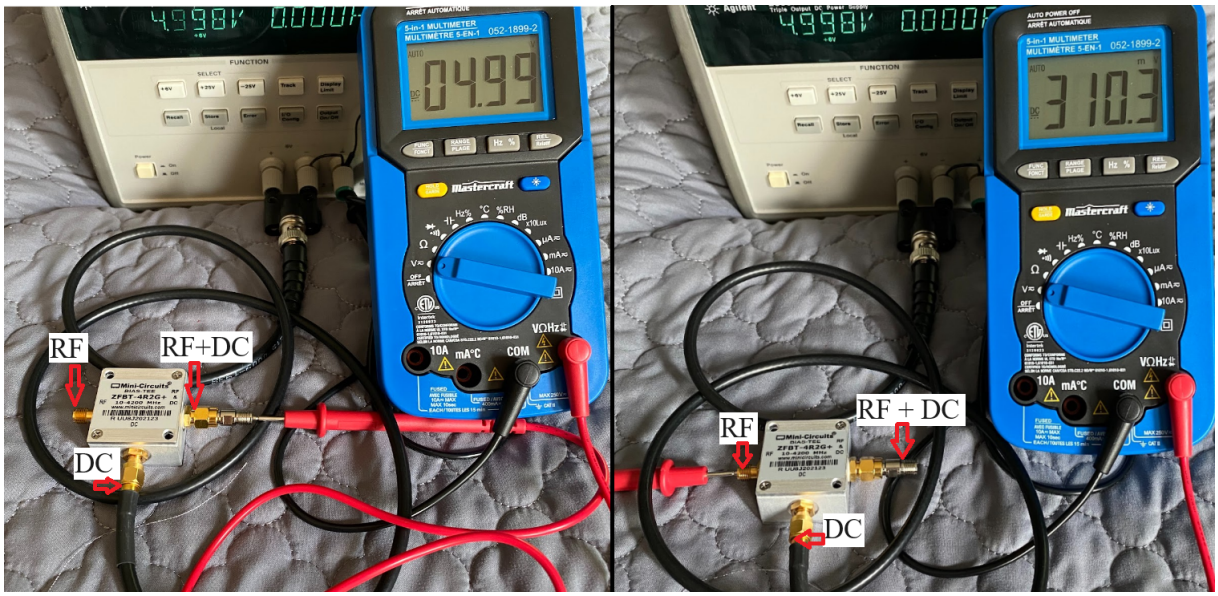

Figure 3.12: Bias-tee testing results

The test results are summarized in Table 3.5 for all three bias-tees implemented in the payload. From to the table, the voltage at the RF+ DC port matched the 4.99 V supplied by the power source, indicating precise alignment. Conversely, the voltage at the RF port registered in millivolts, demonstrating its nearly negligible value. These outcomes affirm the optimal functionality of the bias-tees in facilitating the directed voltage flow to the antenna while effectively blocking it from reaching the front-end.

Mini-Circuit	**Voltage at LNA (V)**	**Voltage at DC block (mV)**
1	4.99	327.5
2	4.99	310.3
3	4.99	300.2

Table 3.5: Bias-tee testing results

3.4.3 Front-End Simulation Testing

A reliable method to validate the functionality of the front-end and the onboard computer within a laboratory setting involves utilizing a GNSS signal simulator. In this experiment, the GSS9000 GNSS signal simulator was employed, directly connected to the front-end to serve as its RF input. This approach provides a controlled environment for assessing the performance of the front-end and the onboard computer in response to simulated GNSS signals. The experimental setup, illustrated in Figure 3.13, shows the configuration employed for this particular test. In this experiment, the Raw IF data acquired with the front-end on the Raspberry Pi is subject to post-processing in MATLAB utilizing the software-defined receiver.

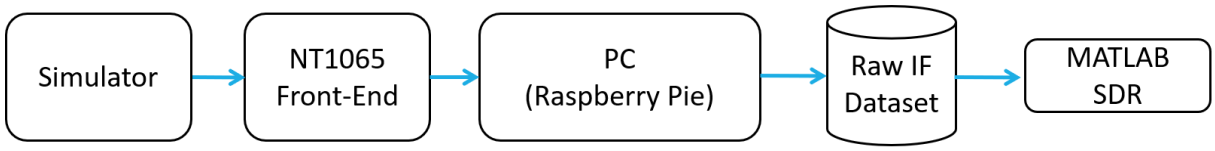

Figure 3.13: Front-end and Raspberry Pie simulator testing

In Figure 3.14, screen captures from the simulator reveal both the skyplot and a generated list of available pseudo-random noise (PRN) numbers. It's important to note

that the list follows chronological order based on the PRN numbers, not their visibility. The accompanying table and skyplot affirm the presence of PRNs 1, 3, 6, 7, 11, 14, 16, 19, 20, 22, 23, and 25 in the simulated scenario.

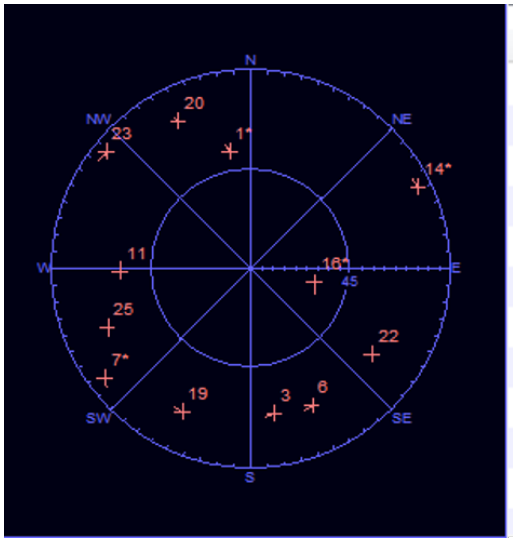

PRN	Elev	Azim	Tropo	Iono	Pseudorange
1	36.4	-10.3	4.2	2.3	22275894.204
3	23.8	170.7	6.1	3.0	23333203.197
6	22.3	155.8	6.4	3.1	23473692.388
7	8.1	-126.7	16.7	4.2	24904149.772
11	31.3	-91.3	4.7	2.6	22678714.618
14	6.2	64.1	21.2	4.4	25107263.465
16	60.4	102.0	2.8	1.7	20826807.399
19	18.7	-154.4	7.6	3.4	23823544.760
20	16.1	-26.2	8.7	3.5	24070987.159
22	23.2	125.4	6.2	3.0	23390789.065
23	6.4	-51.1	20.4	4.4	25079505.247
25	20.5	-112.2	7.0	3.2	23650876.670

Figure 3.14: Simulator's skyplot and PRN availability

In Figure 3.15, the acquisition plot illustrates the dataset collected using the signal simulator. The acquired satellites include PRNs 1, 3, 6, 7, 11, 14, 16, 19, 20, 23, 25, and 31. Notably, the MATLAB SDR missed PRN 22 but successfully acquired PRN 31, which, despite not appearing in the skyplot or table, contributes to an overall accuracy of 11 out of 12 satellites. This outcome serves as a verification that both the front-end and the onboard computer, Raspberry Pi, can function correctly and pass this specific test.

3.4.4 Tripod Testing:

In the conclusive phase of testing, the entire payload configuration, resembling the architecture depicted in Figure 3.1, undergoes comprehensive evaluation. This involves connecting the antenna to the front-end through the bias-tee, linking the front-end to the Raspberry Pi, and supplying power to the entire system via a battery pack. The experiment is conducted with the antenna positioned on a tripod just outside the York

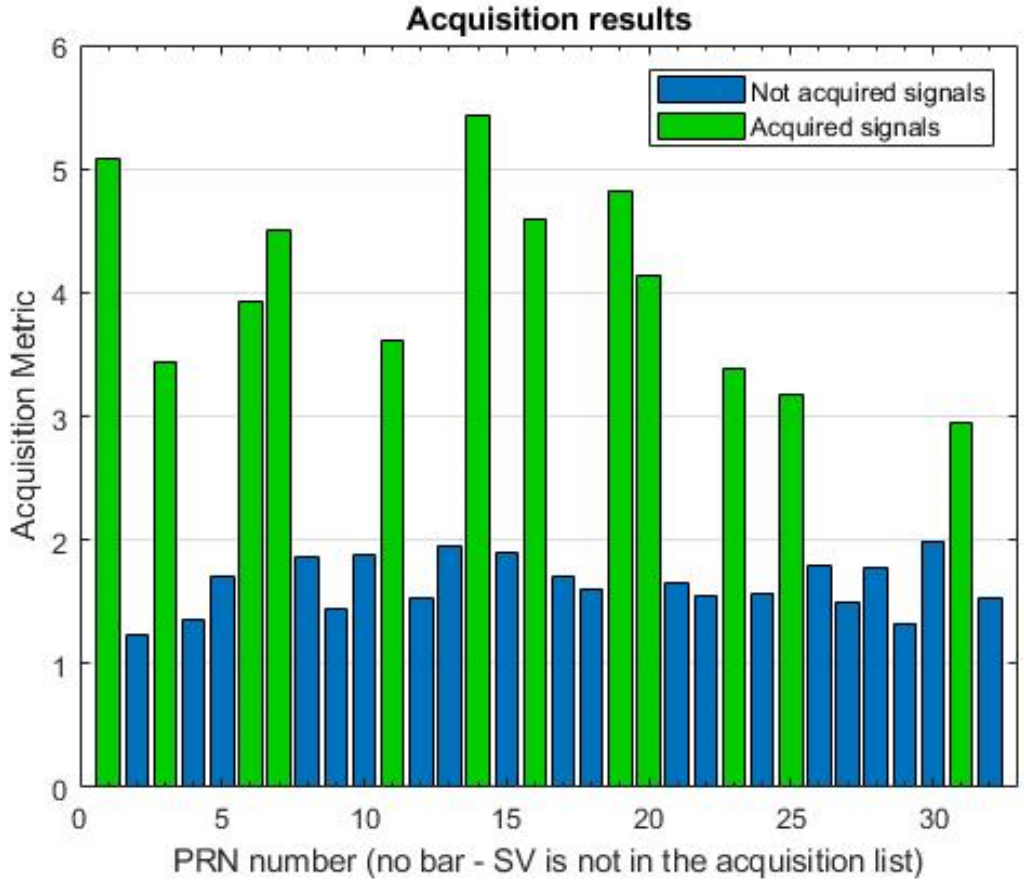

Figure 3.15: Acquisition results for the data gathered using signal simulator

GNSS lab, situated at Keele 4751 in the parking lot.

The sampled data underwent post-processing using the MATLAB SDR, as employed in previous simulation tests. The outcomes are presented in Figure 3.16, revealing the successful acquisition of PRNs 10, 24, and 32, the top three visible satellites at the given time and location. Based on the location and time parameters, GNSS planning software predicted these visible GPS satellites. Notably, the absence of PRN 23 was observed.

It's crucial to recognize that both the power levels and the count of acquired GPS satellites are notably lower than in the simulation. This divergence can be attributed to the inherent differences in the testing setups. Unlike the GNSS simulator, the real-world scenario involves the antenna capturing signals, which then traverse through various hardware components, such as the bias-tee and attenuator, before reaching the front-

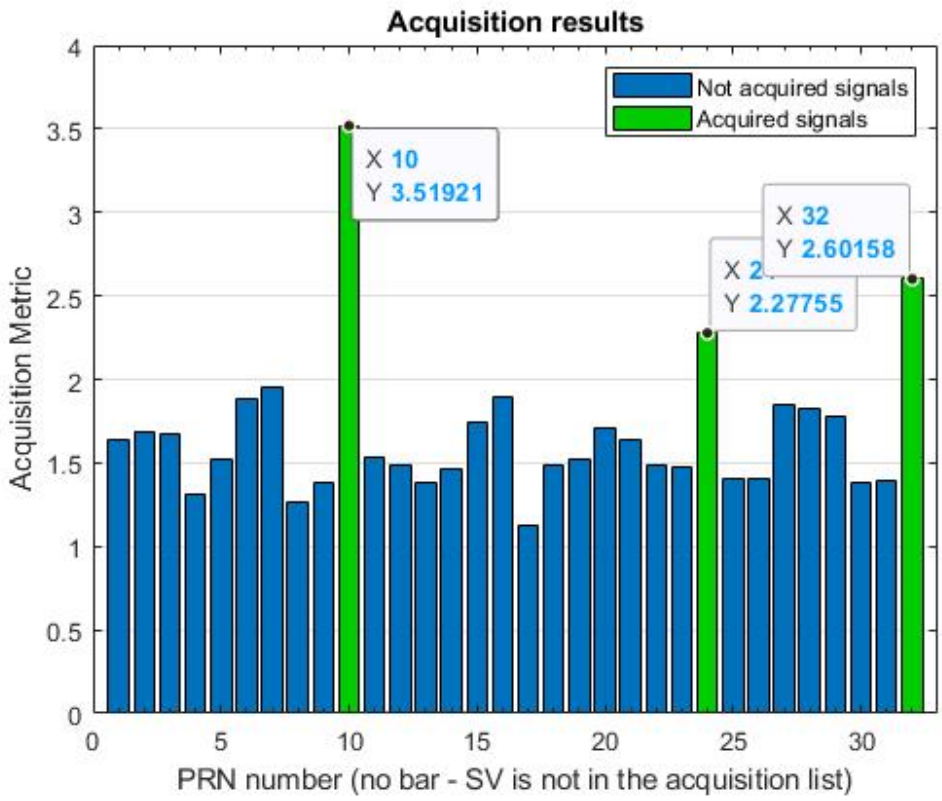

Figure 3.16: Acquisition results for the tripod testing

end. Additionally, the testing location's proximity to a building introduced potential obstacles, limiting the antenna's access to the complete clear sky. However, this constraint is expected to be mitigated during actual payload deployment on a drone, as it will operate above any obstructions.

3.5 Data Collection Flights

Figures 3.17, 3.18, and 3.19 depict the flight paths undertaken during the three data collection flights. Each flight took off from the same launch site, progressing until the UAV positioned itself directly over the target reflective surface, where it remained stationary for the data collection process. Figure 3.20 is the real-time view captured by the onboard camera, showcasing the three distinct landforms under observation.

These flights were conducted at Bluffer's Park Beach in Scarborough. This location

enabled the UAV to swiftly transition between flying over the waters of Lake Ontario, hovering above the sandy terrain of Bluffer's Beach, and positioning itself atop the dense vegetation of Scarborough Bluffs. This versatility provided the opportunity to compare the reflective properties of these three different surfaces. These flights took place on November 24, 2022.

3.5.1 Over Vegetation Flight

The drone initiated its flight from the helipad, starting at 50 meters and eventually ascending to 77 meters above the launch height as it positioned itself for data collection. This increase in altitude was necessary to account for the bluffs and tall trees. The distance between the take-off and hovering points was approximately 260 meters, ensuring the drone was precisely positioned above dense vegetation. The antenna has a beamwidth of 139 degrees, so at an altitude of 77 meters, the radius of the field of view is around 200 meters. Maneuvering the drone into the desired position took 2 minutes and 26 seconds. The payload began collecting data right before take-off, lasting for 10.5 minutes. This resulted in approximately 8 minutes of valuable data collected over the vegetation (see figure 3.17).

3.5.2 Over Sand Flight

The drone began its flight from the helipad, ascending to 43 meters above the launch height. Since it was already positioned atop the beach, the ascent was vertical, taking less than 1 minute to reach the desired altitude. The helipad was removed during this ascent, and everyone moved approximately 50 meters away to the side to clear the beach area. The payload began collecting data right before take-off, lasting for 10.5 minutes. This resulted in approximately 9 minutes of valuable data collected over the sand (see figure 3.18).

Figure 3.17: UAV flight path over vegetation

Figure 3.18: UAV flight path over sand

3.5.3 Over Water Flight

The drone initiated its flight from the helipad, ascended to 45 meters above the launch height and maintained this altitude throughout the flight. The distance between the take-off and hovering point was approximately 150 meters, ensuring the drone was positioned above water. Maneuvering the drone into the desired position took close to 2 minutes. The payload began collecting data right before take-off, lasting for 10.5 minutes. This resulted in approximately 8.5 minutes of valuable data collected over the water (see figure 3.19).

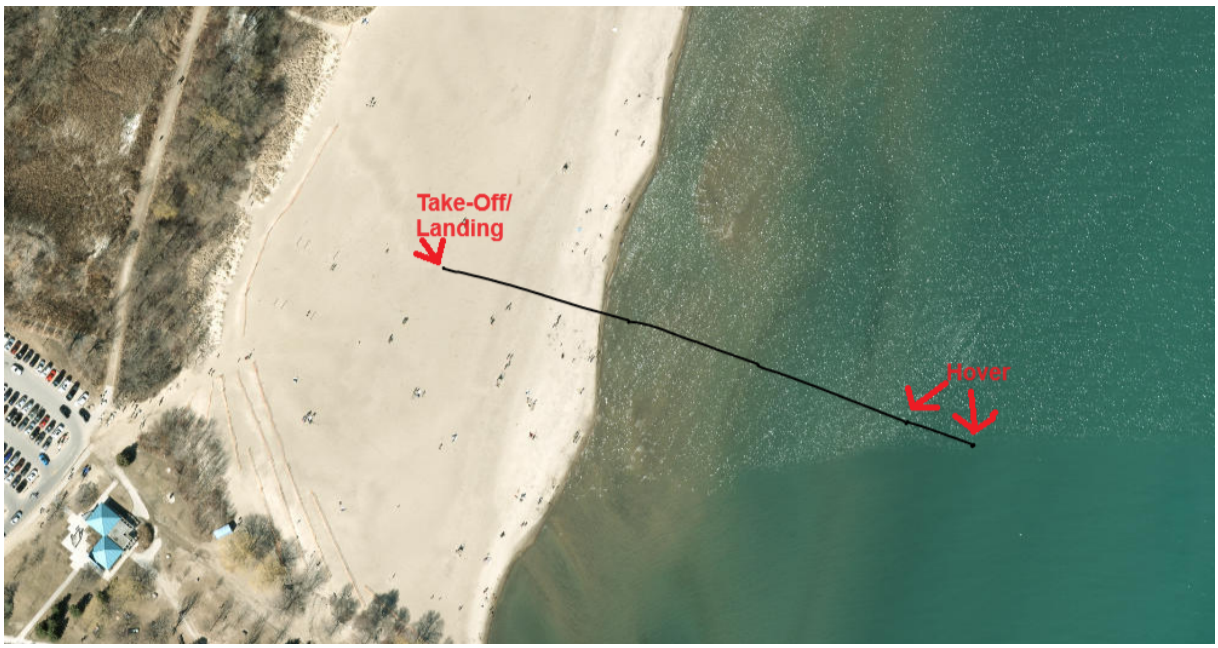

Figure 3.19: UAV flight path over water

3.6 Chapter Summary

In summary, the chapter details the development process of the payload, which was custom-built to meet specific requirements and ensure compatibility with UAV systems like the DJI MATRICE 300 RTK. The resulting payload receives RHCP and LHCP signals, operates for over 20 minutes, and weighs just under 1.3 kg. Its design minimizes interference with UAV sensors and propellers, incorporating key components such as active dual-polarized GPS antennas, bias tees, an RF front-end receiver, and an onboard computer. Each component underwent testing to confirm functionality, as outlined in section 3.4. Pre-flight testing was done indoors with a GNSS signal simulator and outdoors on top of a tripod. The field campaign aimed to verify its GNSS reflectometry capabilities across various terrains, including water, sand, and vegetation.

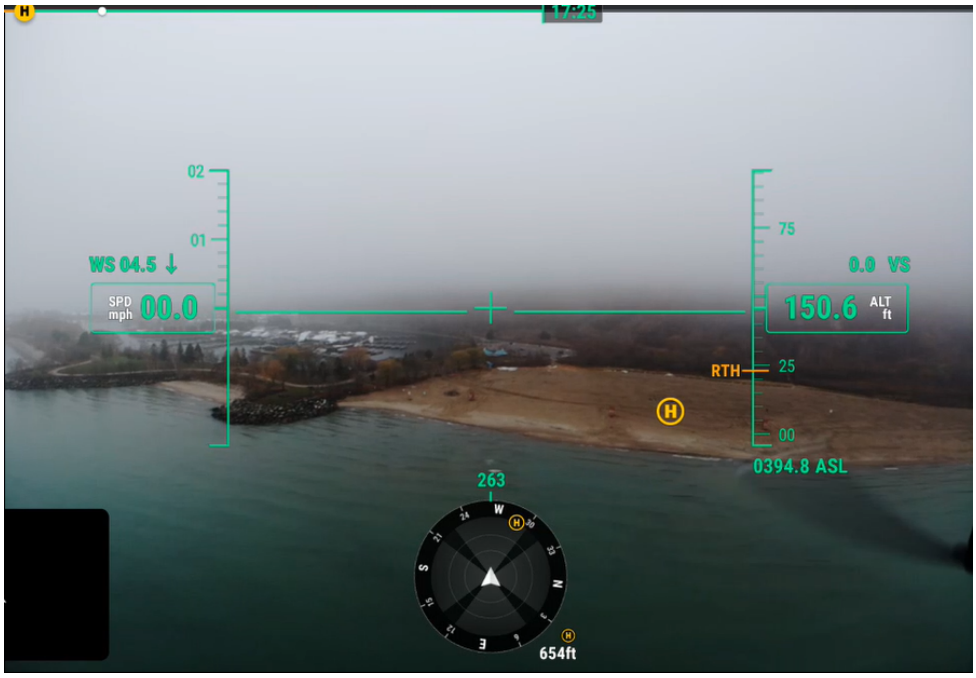

Figure 3.20: UAV camera view from Lake Ontario

Chapter 4
Payload Verification

In Chapter 3, the payload underwent design, development, and testing to ensure it met its basic requirements. The primary objective of this chapter is to validate the reflectometry functionality of the UAV-based payload, captured on a COTS front-end and post-processed by CYGNSS software. The approach involves a systematic process to replicate the expected results outlined in existing literature.

It is important to note that the research scope does not involve an in-depth analysis of reflectometry outcomes to determine precise values for specific geophysical properties such as soil moisture. Instead, the focus is on observing specific characteristics evident in reflectometry products, such as DDM and DWF. For instance, when examining reflections from different surfaces, such as calm water versus a highly vegetative and rough surface, two key observations are anticipated: lower signal powers and increased noise. These insights can be easily derived from reflectometry products like DDM and DWF.

Building on previous GNSS-R research, the hypothesis is that smooth physical surfaces, such as sandy beaches or calm lake water, yield higher power and more coherent results than rough, highly vegetative surfaces. This chapter will utilize the collected data to generate reflectometry products, specifically DDM and DWF, for each surface. The subsequent analysis will determine whether the results align with the hypothesis, providing valuable insights into the reflectometry capabilities of the developed payload.

4.1 Methodology

Figure 4.1 depicts the methodology used for payload verification. Initiating the process involves working from the raw dataset captured during the field campaign with the payload.

Concurrently, detailed information, including the exact times of capture and location, is recorded for each flight. As the dataset is obtained using a COTS front-end and post-processed with NASA's CYGNSS code, a secondary code is employed to reformat the raw dataset into a format compatible with the CYGNSS C code software. This technical transformation will be elaborated upon in Section 4.2.

Subsequently, the code executes a cold call on all 32 PRNs to determine which ones are acquired. In this context, a cold call refers to the program's search for all 32 potential GPS satellites rather than relying on an almanac to anticipate which satellites would be visible based on the receiver's position at a specific time. The acquired PRNs are then recorded and sorted based on their correlated powers. Simultaneously, utilizing each dataset's time and location data, available PRNs are derived using GNSS planning software. The results of the acquisition and the planning software are compared to one another to verify the acquisition step. Moving to the next stage, ensuring that the reflections from the acquired PRNs originate from the intended surfaces becomes crucial. Given the proximity of the bluffs, beach, and lake, there is a potential risk that satellite reflections may come from neighboring surfaces. To mitigate this, specular point locations are mapped for each acquired PRN. Once this verification is completed, the dataset can be leveraged to generate DDM and DWF for each PRN in that specific dataset.

This process is iterated for all three datasets, each corresponding to a distinct reflective surface. Following this, the reflectometry products of each dataset are individually studied and then compared with one another to assess if the results align with the predictions in the hypothesis. This comprehensive analysis serves as the verification of the payload.

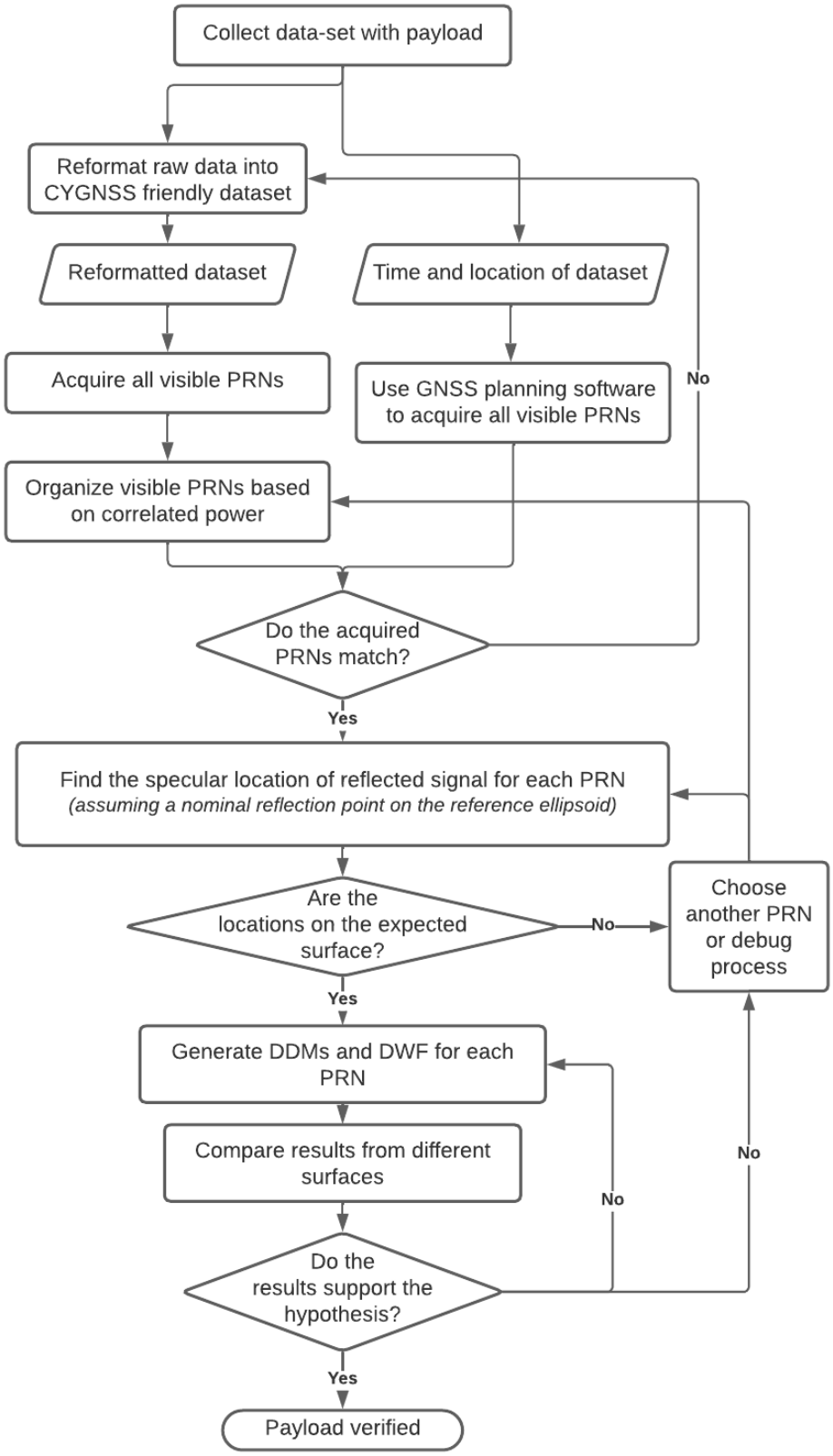

Figure 4.1: Methodology flowchart for payload verification

4.2 Post Processing of the Data-Sets

NASA's CYGNSS C and Octave code were used to post-process the payload's data to address this. It is essential to highlight that the CYGNSS C code was originally designed for the further ground processing of raw IF data acquired by the CYGNSS mission satellites, which differs from the NT1065, a COTS front-end used in our experiment. Consequently, modifying the C code and incorporating a Python script was implemented to reformat the NT lab data set, facilitating the processing of the raw IF data using the NT data set. This section of the thesis provides an in-depth exploration of this process.

4.2.1 NT1065 Format

The thesis outlines the utilization of the NT1065 front-end, provided by NTLab, for the acquisition of IF data sets from each antenna channel within the payload. In the conducted experiments, the chosen file structure for the NT1065 front-end data output is the "Single File, all Channels" mode, as illustrated in Figure 4.2. Under this configuration, data from all four channels, comprising the direct and two reflected antennas and channel four connected to a terminator, are interleaved. Each byte within this data structure consists of eight bits, subdivided into groups of two bits each. These two-bit groups represent the sign and magnitude of a single sample from an individual channel.

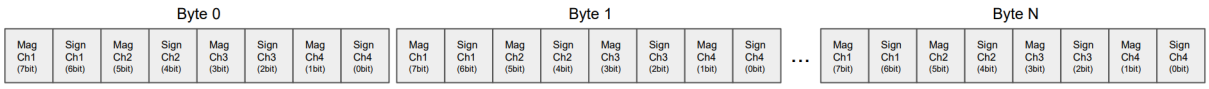

Figure 4.2: NT1065's "Single file, all channels" mode (NTLAB 2021)

4.2.2 CYGNSS Format

Figure 4.3 shows the CYGNSS raw IF data structure. The CYGNSS data set differs from NTlab in several vital ways. First, while NTlab incorporates four channels, CYGNSS

utilizes only three channels. This disparity arises because NT1065 is a COTS product with four channels, while CYGNSS front-ends are made for the mission's requirements.

Moreover, the structure of the data sets varies significantly between the two systems. In CYGNSS, data from the three channels is organized through byte interleaving. Each byte within the data set comprises four samples from a single channel, and the subsequent byte contains four samples from the following channel.

Conversely, NTlab's data arrangement differs because each byte contains samples from all four channels. Another noteworthy distinction emerges in the ADC bit assignments. In the case of NT1065, odd-numbered bits correspond to magnitude, while even-numbered bits represent Signs. This bit assignment is reversed in CYGNSS, further accentuating the contrast between these two systems.

Data format: 2 Data format name: Channel 0, 1, 2. Sampling: I only, 2bit				
Byte number	Bit number	Channel number	Sample number	ADC bit
0	7	0	0	Sign
0	6	0	0	Mag.
0	5	0	1	Sign
0	4	0	1	Mag.
0	3	0	2	Sign
0	2	0	2	Mag.
0	1	0	3	Sign
0	0	0	3	Mag.
1	7	1	0	Sign
1	6	1	0	Mag.
1	5	1	1	Sign
1	4	1	1	Mag.
1	3	1	2	Sign
1	2	1	2	Mag.
1	1	1	3	Sign
1	0	1	3	Mag.
2	7	2	0	Sign
2	6	2	0	Mag.
2	5	2	1	Sign
2	4	2	1	Mag.
2	3	2	2	Sign
2	2	2	2	Mag.
2	1	2	3	Sign
2	0	2	3	Mag.
Repeating…	Repeating…	Repeating…	4	Repeating…

Figure 4.3: Interleaving of raw IF data bytes for 3 channel sampling (Gleason et al. 2020)

4.2.3 Reformatting

The initial phase of data reformatting occurs within Python code. Users can specify start and end offsets, allowing them to select the specific segment of the data they wish to analyze. Subsequently, within an iterative loop, each byte of data undergoes examination. During this process, the two bits associated with channels one, two, and three are extracted and segregated into separate arrays. In comparison, the final two bits, which pertain to channel four, are disregarded. These bit sequences, corresponding to each channel, are then converted into byte arrays and saved as individual .bin files, rendering them compatible with the subsequent C code for further analysis and processing.

Further code modifications were introduced to the CYGNSS C code, reversing the ADC assignments. Specifically, odd-numbered bits now signify magnitude, whereas even-numbered bits signify Sign. Furthermore, configuration settings were adjusted to accommodate a single channel presence instead of three, thus preventing any accidental skipping of bytes.

4.3 Verification of Direct Acquisition Results

Following reformatting the dataset, the initial step involves verifying direct acquisition results. The primary objective is to identify visible pseudo-random noise (PRNs) for each dataset, with a secondary aim of validating the GNSS portion's functionality within the GNSS-R payload. This verification is crucial, given that GNSS-R instruments rely on a zenith antenna for navigation solutions and distinguishing anticipated reflections from nadir antennas corresponding to specific PRNs.

The approach employs the C code DDM processor to process each dataset's channel 1, associated with the zenith antenna. This step focuses on determining the acquired PRNs. As previously discussed in Chapter 2, signal acquisition occurs when a distinctive peak emerges during the auto-correlation process, indicating alignment between the re-

ceived signal and the replica generated from a specific PRN code, as explained in 2.1.4.3. Successful direct acquisition is demonstrated when the peak signal strength significantly surpasses the noise level.

Figure 4.4 presents an illustrative example of a signal acquisition scenario. For PRN 30, it is apparent that acquisition was not achieved, primarily due to the proximity of the noise floor to the signal strength. This scenario resembles what one might expect in the case of a reflected signal. However, a distinct and robust peak is discernible when examining PRN 32 in the same context. This outcome is a practical demonstration of successful acquisition, where the signal peak significantly stands out from the noise.

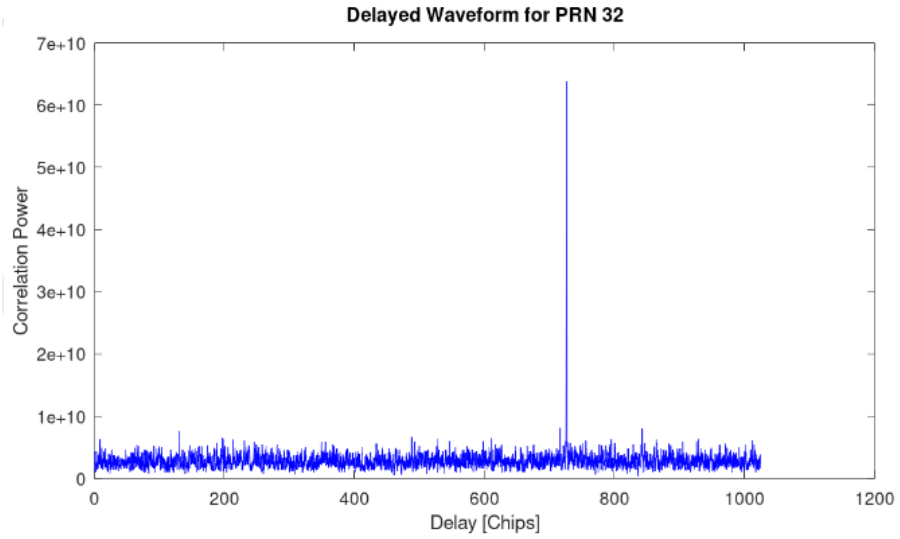

a. Correlation acquired

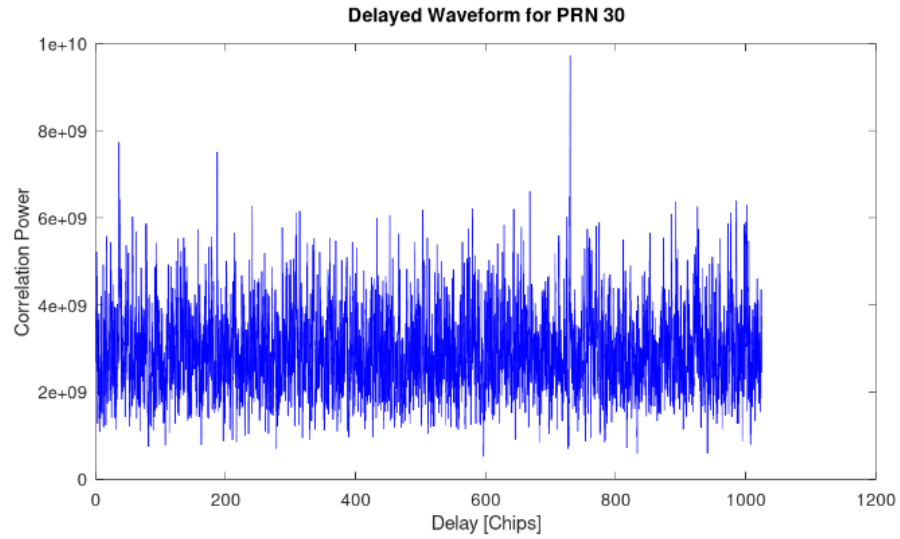

b. No correlation acquired

Figure 4.4: Figure a depicts a scenario where an acquisition peak is clearly present above the noise floor, Figure b depicts a scenario where the acquisition peak is not as clear and very close to the noise floor

4.3.1 GNSS Planning Software

Trimble's GNSS planning software is used to validate acquisition results across datasets. By inputting positioning data such as latitude, longitude, height, and time the software predicts the visibility of satellites for that particular location. Utilizing satellite orbits, Earth's rotation, and atmospheric conditions, the software calculates the availability of PRN signals over time.

The Sky Plot screen in Figures 4.5, 4.6, and 4.7 illustrates the GNSS planning software's visualization for GPS satellites within a 5-minute interval, focusing on the relevant portions of each dataset discussed in the previous section. In Figure 4.5, PRNs 10, 12, 21, 22, 23, 24, 25, 31, and 32 are visible. Similarly, in Figure 4.6, the visible PRNs include 10, 12, 21, 22, 23, 24, 25, and 32. Lastly, Figure 4.7 depicts the visibility of PRNs 10, 12, 21, 22, 25, 31, and 32.

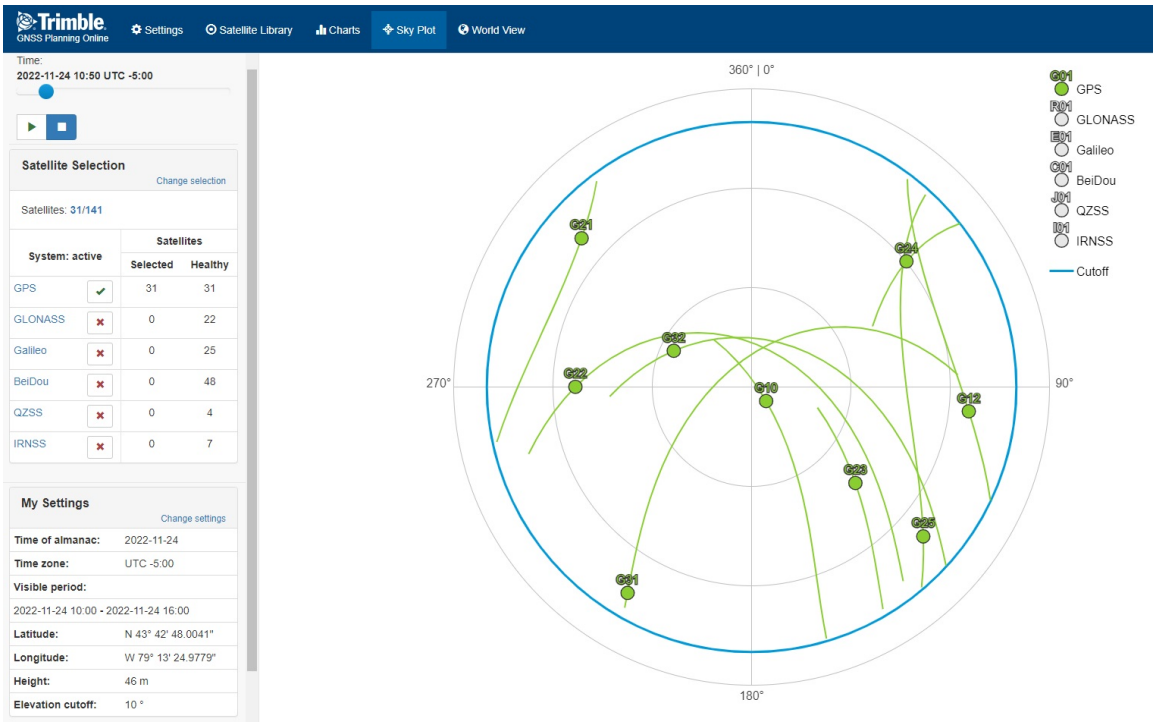

Figure 4.5: Trimble PRNs Water (Trimble-Inc. 2023)

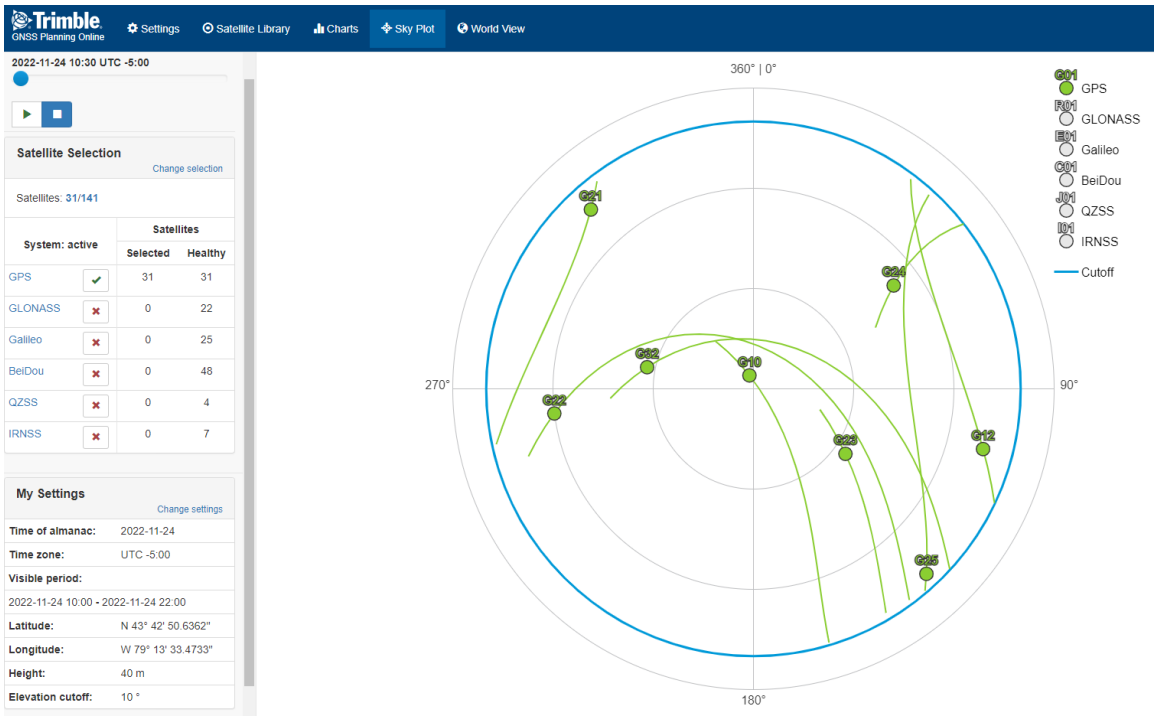

Figure 4.6: Trimble PRNs Sand (Trimble-Inc. 2023)

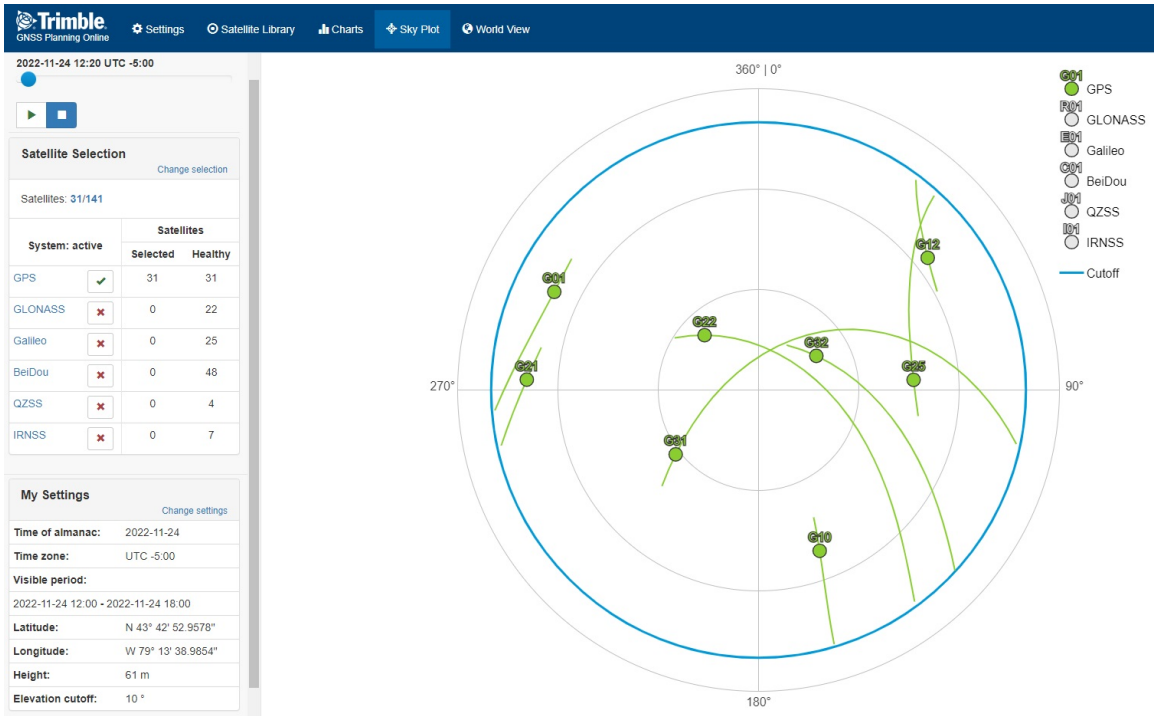

Figure 4.7: Trimble PRNs Vegetation (Trimble-Inc. 2023)

4.3.2 Over Water Acquisition Results

Figures 4.8 and 4.9 present the acquisition results for all 32 PRNs in the dataset captured over water using a drone. The x-axis denotes the delay, while the y-axis represents correlation power. The DDM processor conducted the PRN search, employing a cold-case approach with a short data duration of 1 second, corresponding to one DDM or DWF. A broad Doppler search range detected all zenith direct signals in view. A threshold of 1e10 was set for the acquisition process, designating anything above this value as a successfully acquired satellite. Examining Figure 4.8 and 4.9, PRNs 10, 12, 21, 22, 23, 31, and 32 have been successfully acquired.

4.3.3 Over Sand Acquisition Results

Figures 4.10 and 4.11 display the acquisition outcomes for all 32 PRNs in the dataset captured over a sandy beach. In alignment with the overwater acquisition, the x-axis signifies the delay, while the y-axis illustrates correlation power. A consistent cold-case approach was applied, maintaining the same data duration and Doppler search range. Figure 4.10 and 4.11 shows that PRNs 10, 11, 24, and 32 have been successfully acquired, as indicated by exceeding the 1e10 threshold.

4.3.4 Over Vegetation Acquisition Results

Figure 4.12 and 4.13 illustrates the acquisition outcomes for all 32 PRNs in the dataset captured over a bluff characterized by high vegetation and rough surfaces. Similar to the water and sand scenarios, the axes, cold-case approach, data duration, and Doppler parameters remain consistent. Analyzing Figure 4.12 and 4.13, it is evident that PRNs 10, 12, 21, 22, 25, 31, and 32 have been successfully acquired, surpassing the 1e10 threshold. This consistent thresholding criterion ensures a standardized evaluation of successful PRN acquisition across varied environmental scenarios.

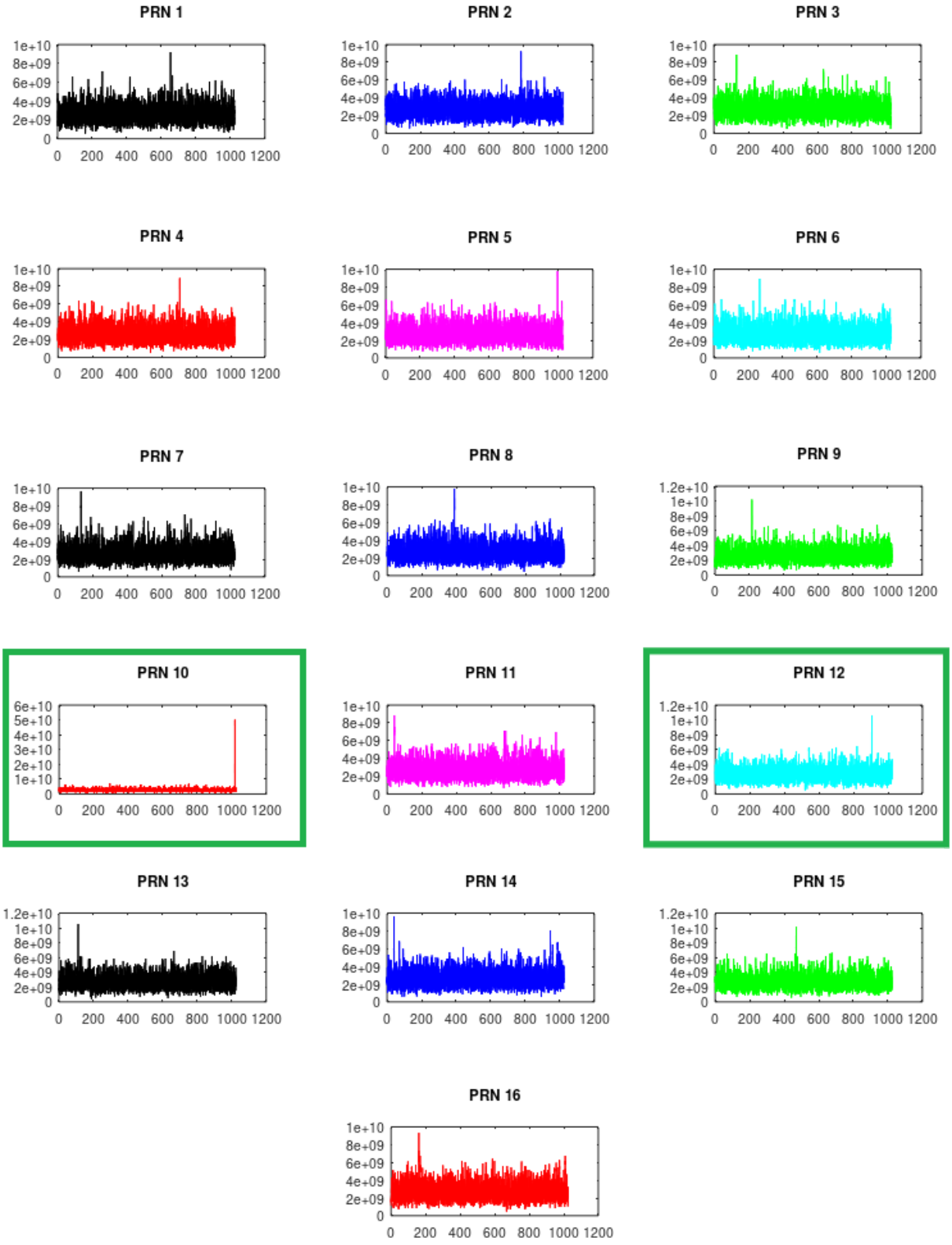

Figure 4.8: Acquisition results over water PRNs 1 to 16

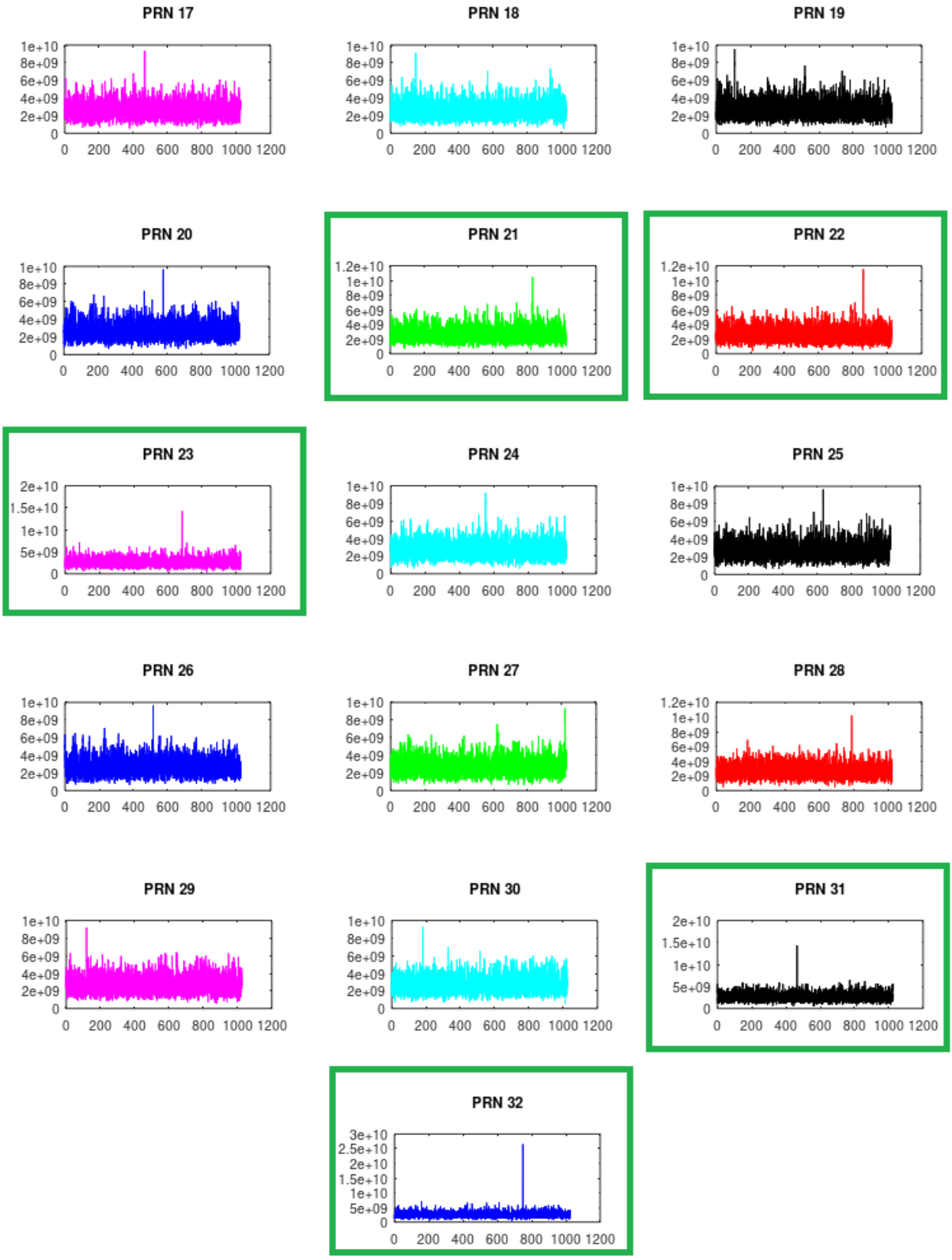

Figure 4.9: Acquisition results over water PRNs 17 to 32

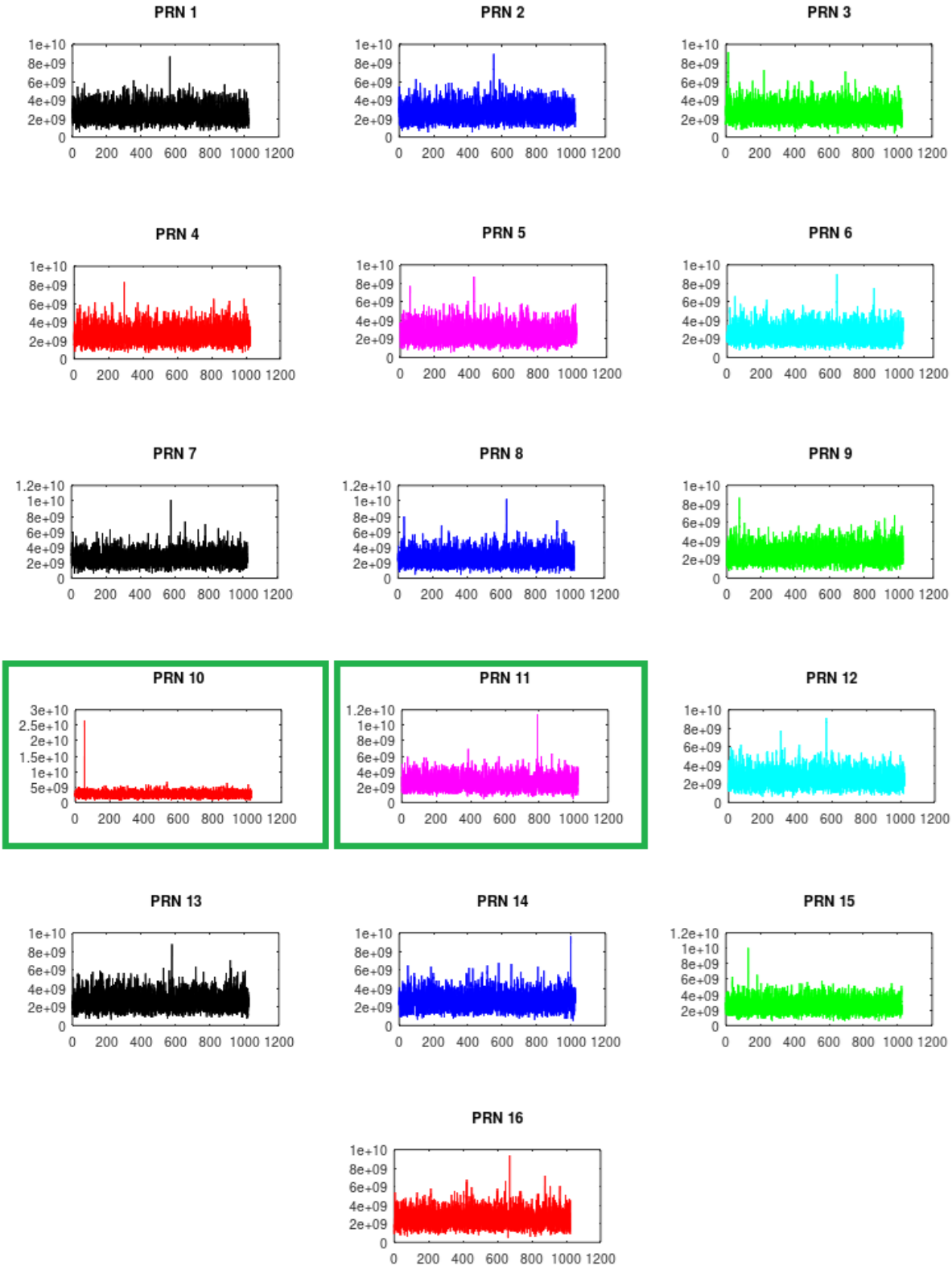

Figure 4.10: Acquisition results over sand PRNs 1 to 16

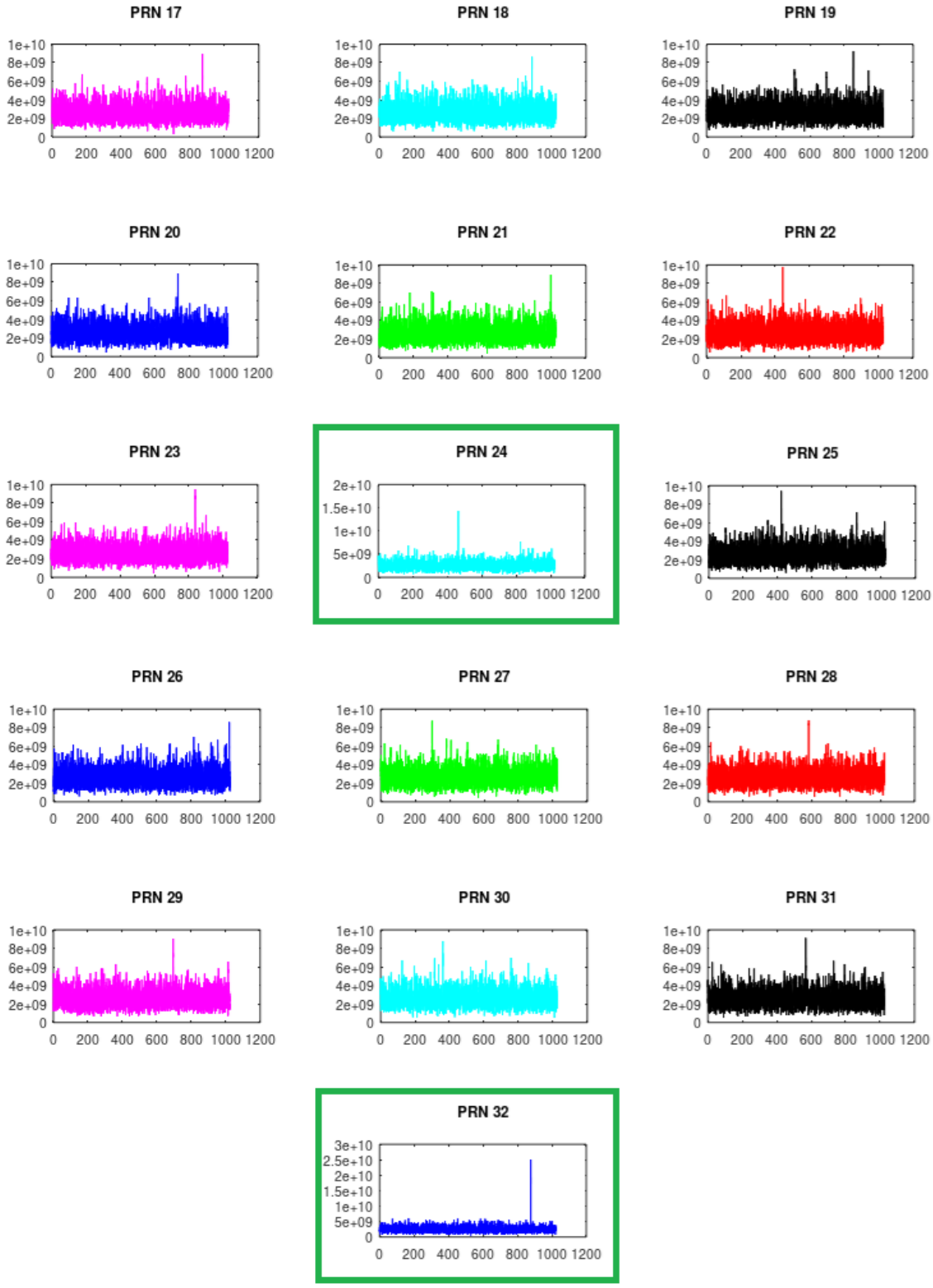

Figure 4.11: Acquisition results over sand PRNs 17 to 32

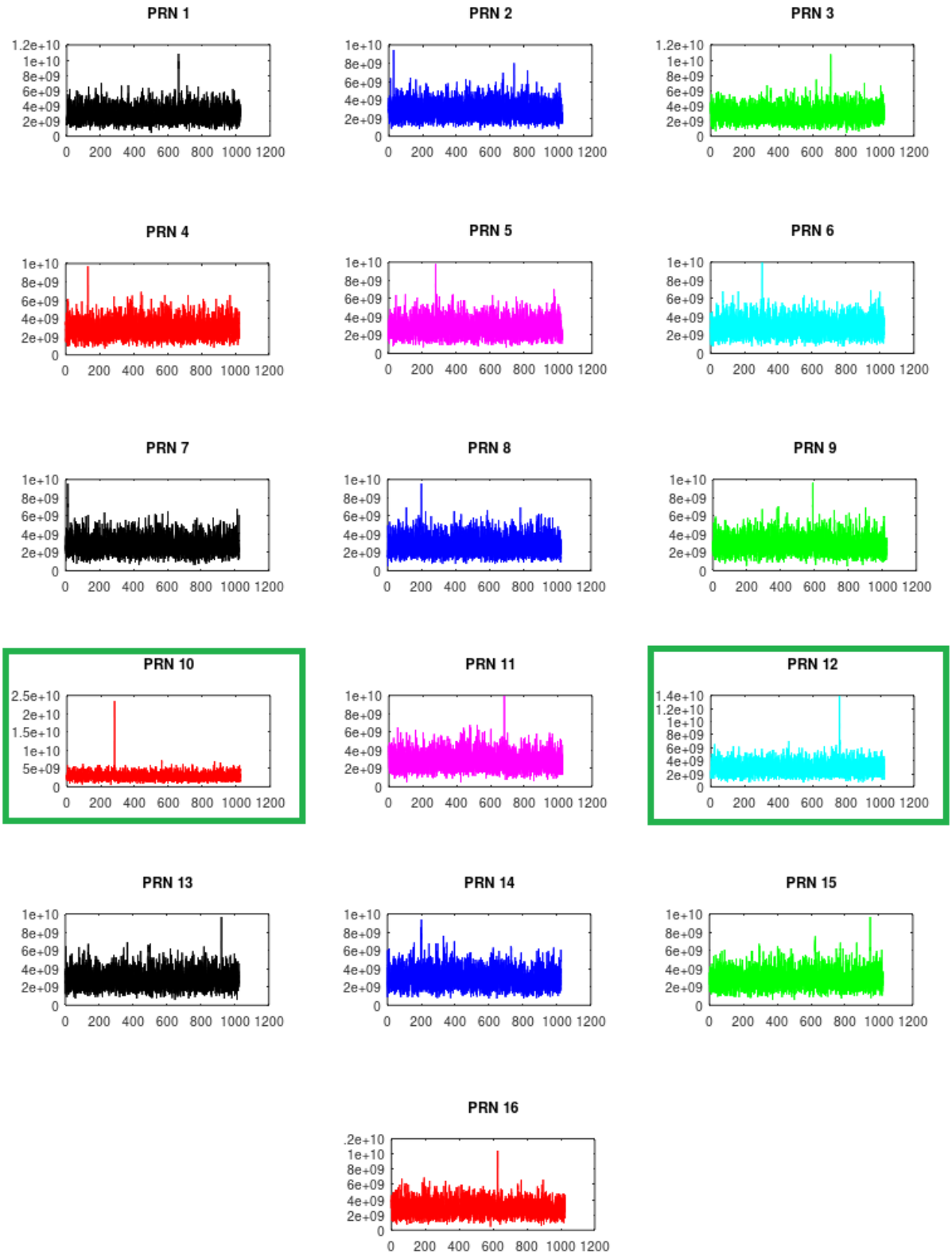

Figure 4.12: Acquisition results over vegetation

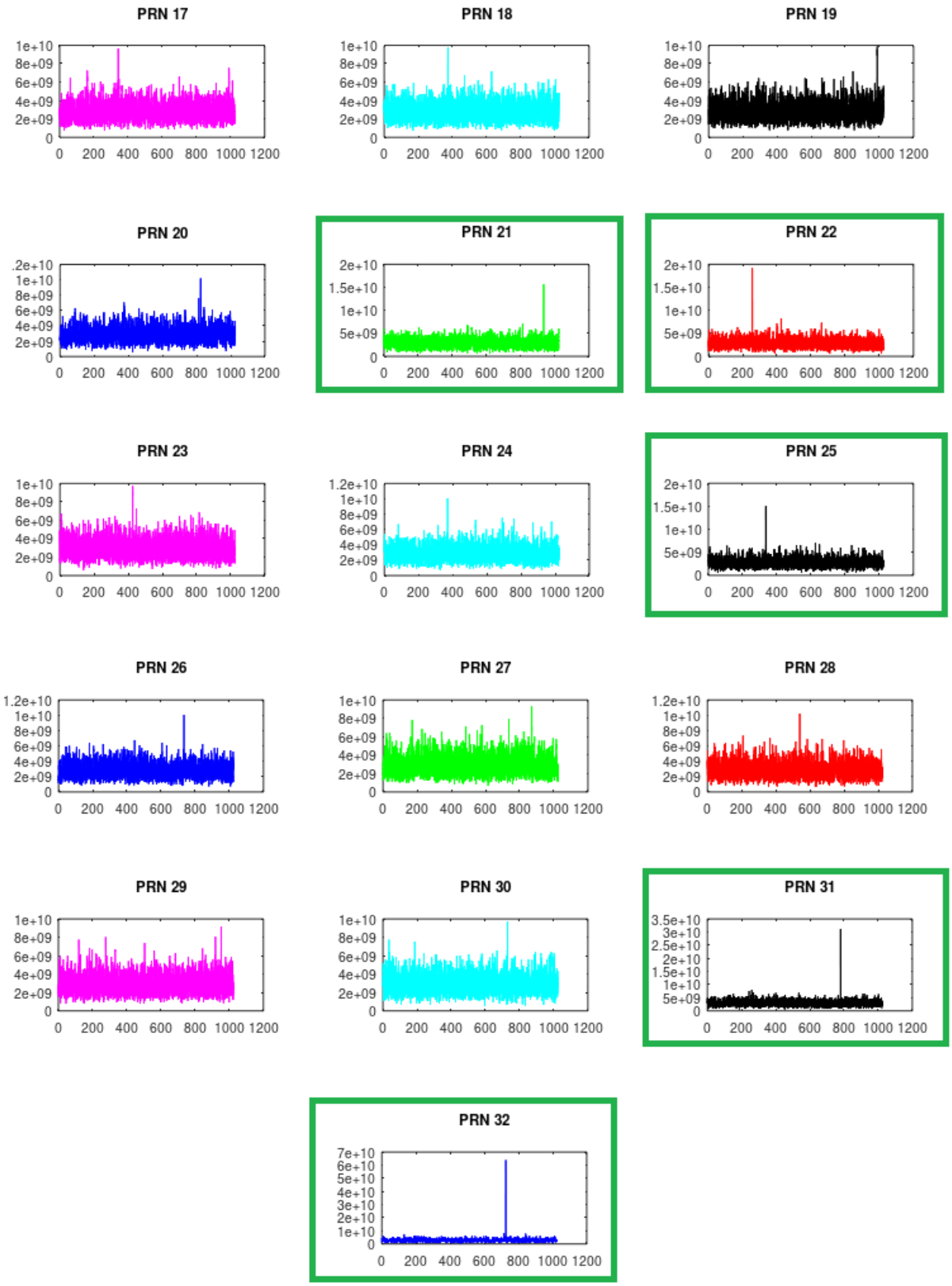

Figure 4.13: Acquisition results over vegetation

4.3.5 Comparing Acquisition Results

In the over-water scenario, the CYGNSS DDM software successfully acquired PRNs 10, 12, 21, 22, 23, 31, and 32. All these PRNs were part of the Trimble planning, except for 24 and 25. Over sand, the acquired PRNs include 10, 11, 24, and 32, aligning with the Trimble planning, except for PRN 11. Over vegetation, the acquired PRNs—10, 12, 21, 22, 25, 31, and 32—align with Trimble. As expected, the top three PRNs with the highest correlation power from each dataset also find correspondence in the Trimble GNSS planning software. For a detailed overview, please refer to Table 4.1, which outlines the top three correlated PRNs per dataset. To enhance the reliability of the reflectometry findings and reduce the likelihood of errors, outliers, or inconsistencies, the analysis was broadened to consider reflections from the top three PRNs exhibiting the highest correlation power rather than exclusively concentrating on the single PRN with the highest correlation power.

Water		**Sand**		**Vegetation**	
Acq.PRN	Corr.Power	Acq.PRN	Corr.Power	Acq.PRN	Corr.Power
10	5.0×10^{10}	10	2.5×10^{10}	32	6.5×10^{10}
32	2.5×10^{10}	32	2.5×10^{10}	31	3.0×10^{10}
23	1.5×10^{10}	24	1.5×10^{10}	10	2.4×10^{10}

Table 4.1: Acquisition results for top 3 PRNs for each data set

4.4 Verification of Specular Points

Water: During the data collection over the lake water, three satellites were acquired to have the highest signal; those are listed in Table 4.1 as PRN10, PRN32, and PRN23. The orbital coordinates of these satellites within one of the five-minute window of the data collection is found:

PRN 10 5908.549641 -19888.745630 16555.030278

PRN 32 -4416.278281 -16658.858148 20412.380183

PRN 23 15149.923342 -20483.774470 7240.201472

Figure 4.14 shows that all three specular points are located close to one another and are on the lake.

Figure 4.14: Specular point water

Sand During the data collection over the beach, three satellites were acquired to have the highest signal; those are listed in Table 4.1 as PRN10, PRN32, and PRN24. The orbital coordinates of these satellites within one of the five-minute window of the data collection is found:

PRN 10 3084.567341 -17991.690630 19335.403864

PRN 32 -7859.292967 -17854.006380 18265.873381

PRN 24 15041.355597 -4528.129818 21054.742944

Figure 4.15 shows that all three specular points are located close to one another on the sandy beach.

Figure 4.15: Specular Point Sand

Vegetation During the data collection over the vegetative bluffs, three satellites were acquired to have the highest signal; those are listed in Table 4.1 as PRN32, PRN31, and PRN10. The orbital coordinates of these satellites within one of the five-minute window of the data collection is found:

PRN 32 9038.158260 -14671.306060 20309.225810

PRN 31 -4105.443535 -23167.954975 11697.042887

PRN 10 10930.688602 -23924.801189 2253.856544 Figure 4.16 shows that all three specular points are located close to one another on the bluffs.

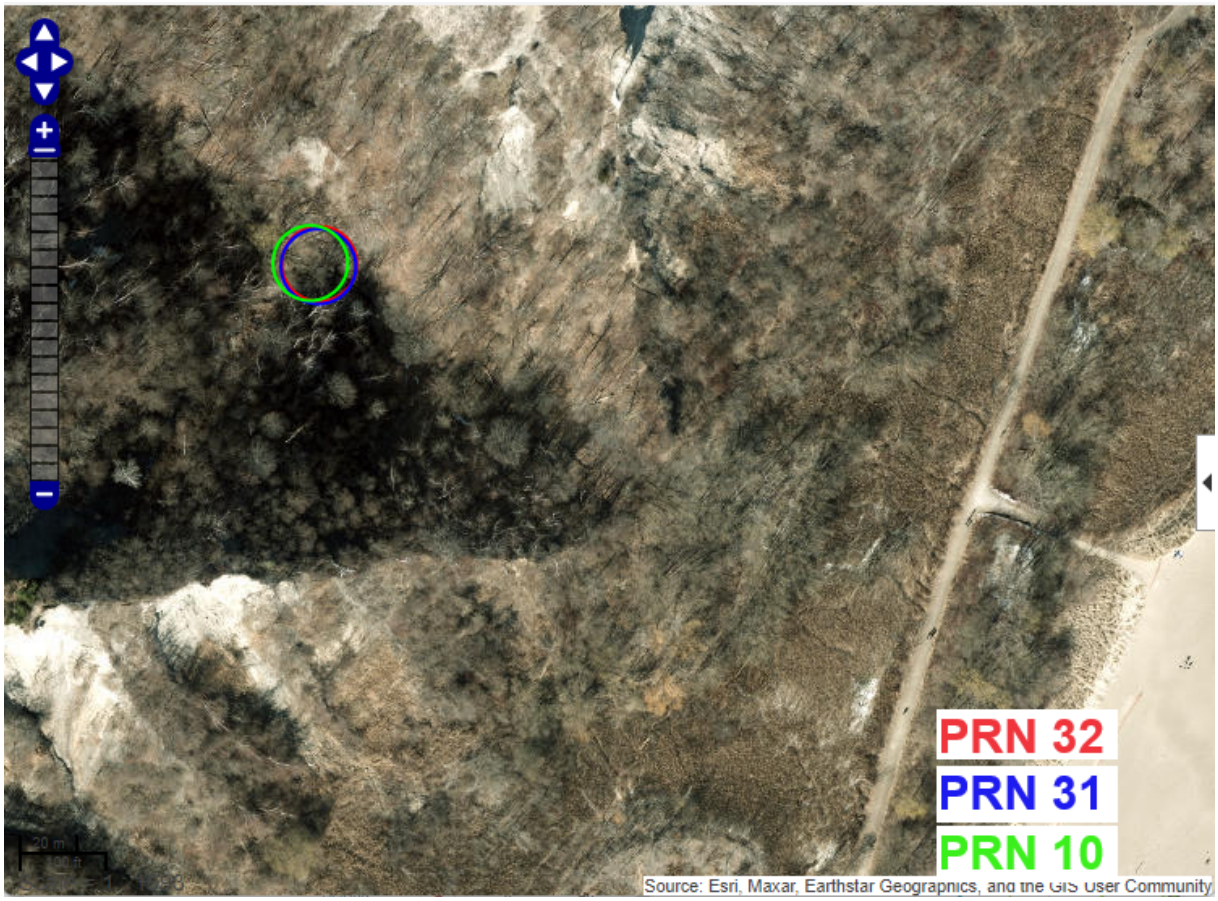

Figure 4.16: Specular Point Vegetation

4.5 Water Reflection Results

DWF: The DWF provides a clear view of the main acquisition peak and the surrounding noise floor. In Figure 4.19, the x-axis represents the delay, and the y-axis represents signal power. Across all three DWFs, a noticeable peak is consistently evident, clearly surpassing the established noise floor. These peaks consistently register at around 8e09, while the noise floor remains consistently set at 4e9.

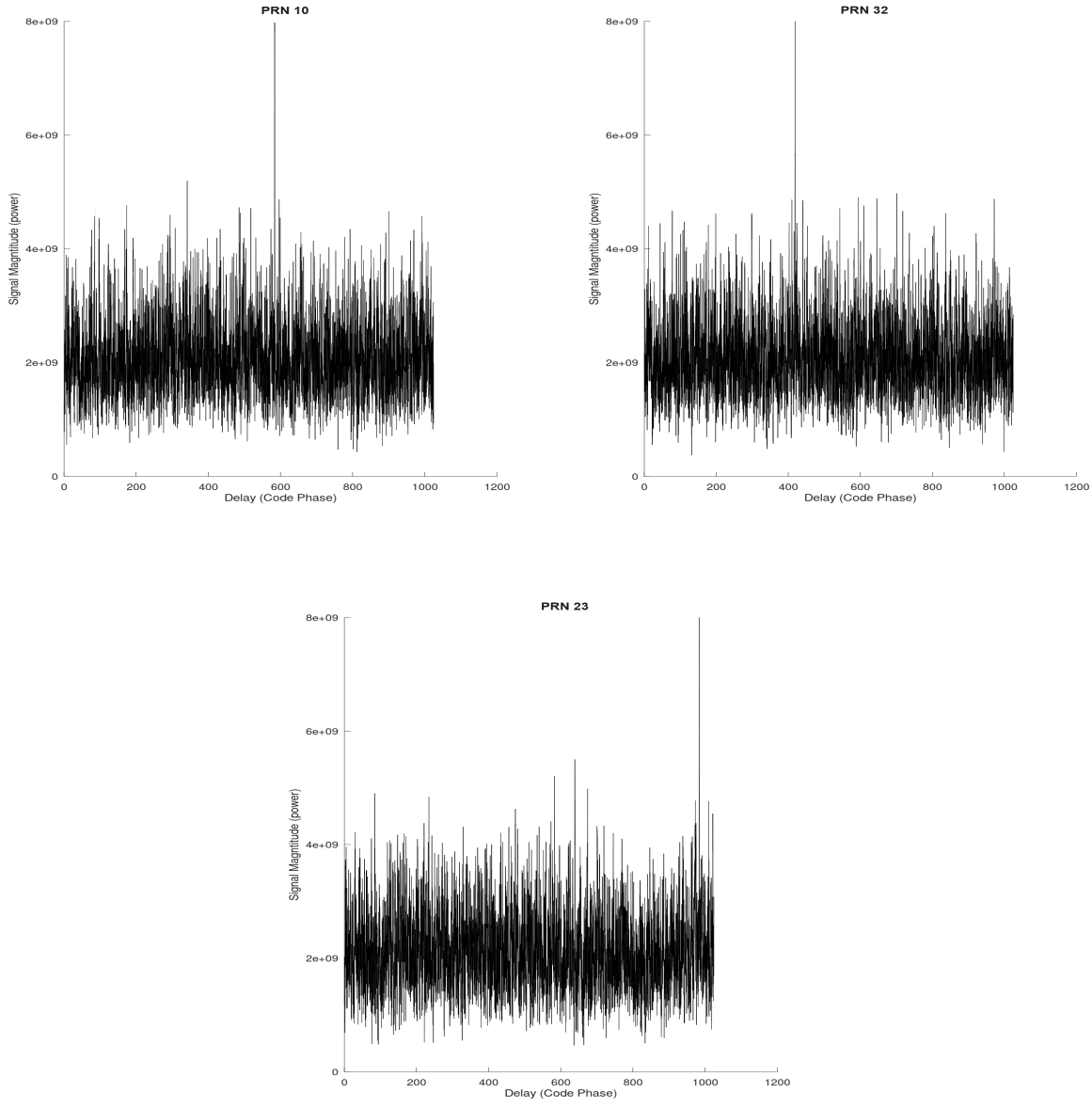

Figure 4.19: DWF of PRNs 10, 32, and 23 from water reflections

DDM: In Figure 4.19, the generated DDMs for PRNs 10, 32, and 23 in the over water dataset are illustrated. The x-axis represents doppler bins, the y-axis represents delay bins, and the colors depict correlation power. The DDMs are deliberately cropped to highlight the program-identified highest power peak, improving the capability to analyze the overall shape. Notably, in these figures, the highest peak emerges at approximately 8e9. The circular appearance of the DDM suggests a dominance of coherent elements and a notable lack of incoherent elements.

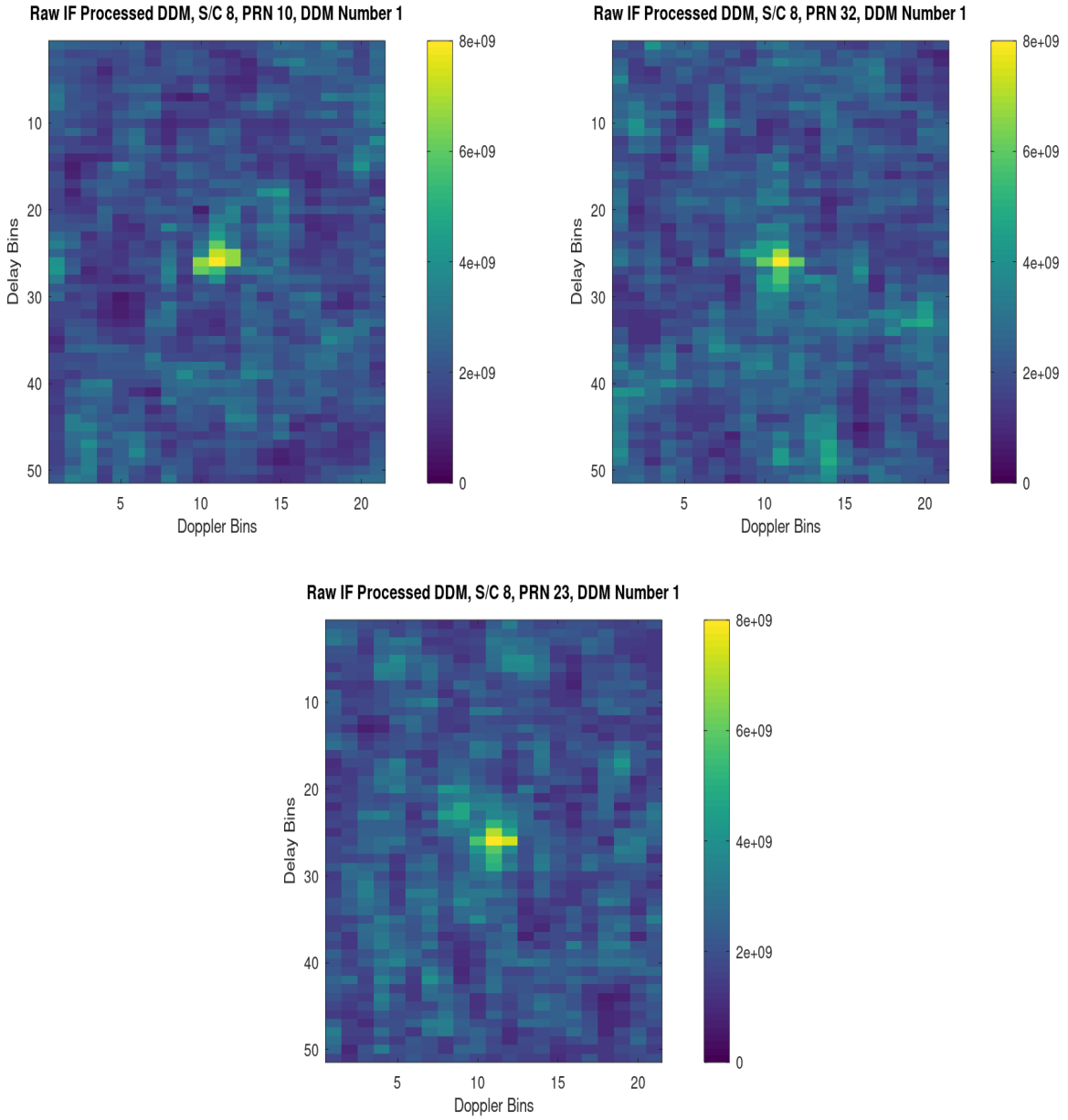

Figure 4.22: DDM of PRNs 10, 32, and 23 from water reflections

4.6 Sand Reflection Results

DWF: Figure 4.22 depicts the DWF for sand reflections for PRNs 10, 32, and 24. On the x-axis, the delay is represented, and the y-axis indicates signal power. In all three DWFs featured in Figure 4.25, a distinct peak is consistently observable, surpassing the established noise floor. These peaks register at approximately 7.5e9, while the noise floor remains consistently set at 4e9. Notably, some noise peaks extend up to 5.5e9.

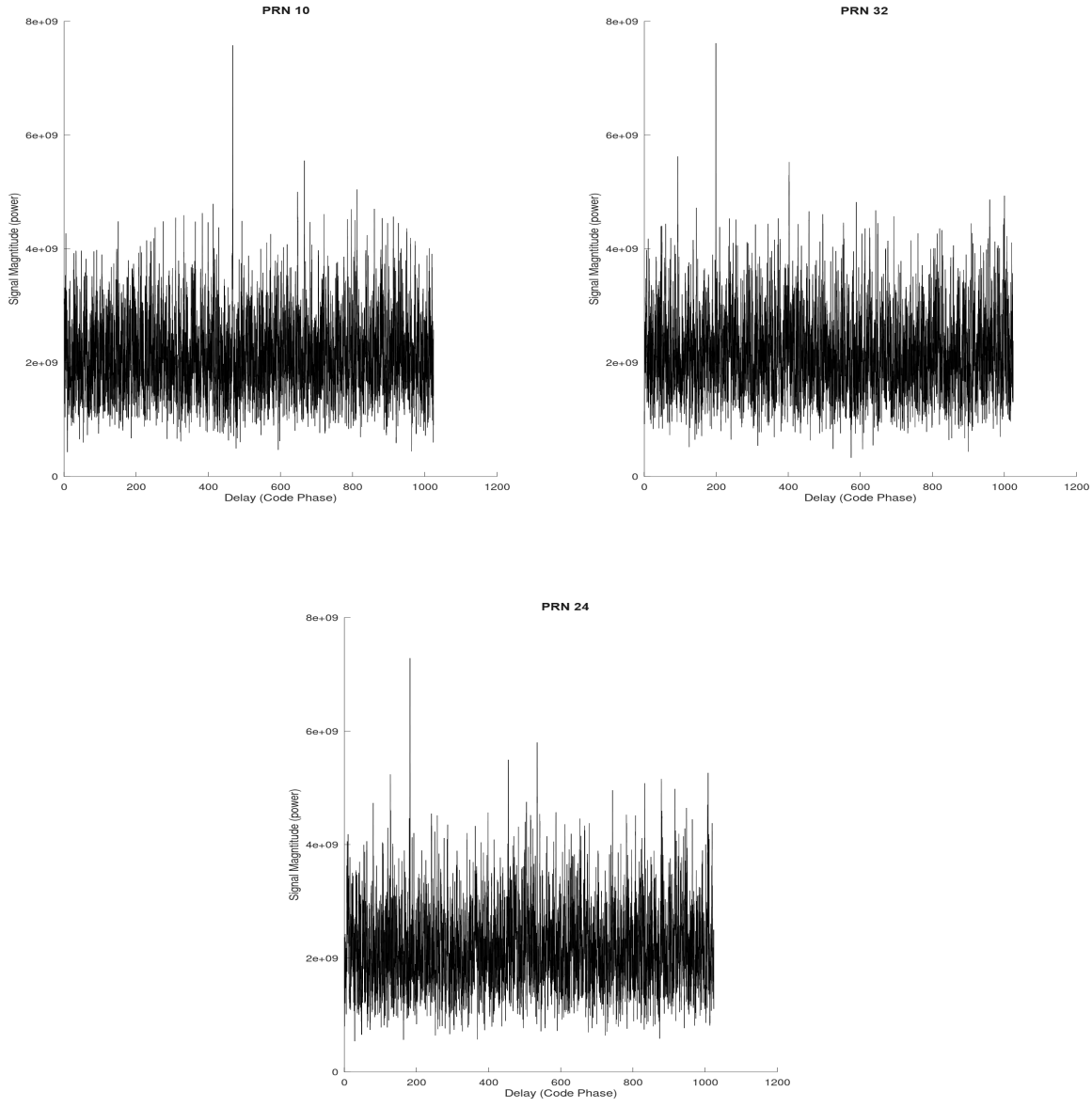

Figure 4.25: DWF of PRNs 10, 32, and 24 from sand reflections

DDM: In Figure 4.23, the generated DDMs for PRNs 10, 32, and 24 for the over sand dataset are illustrated. The x-axis represents Doppler bins, the y-axis represents delay bins, and the colours depict correlation power. The DDMs seem to be cropped around the main peaks, which all appear to have a minimum power of 7e9. The DDMs display a circular shape, which indicates a high degree of coherent element present.

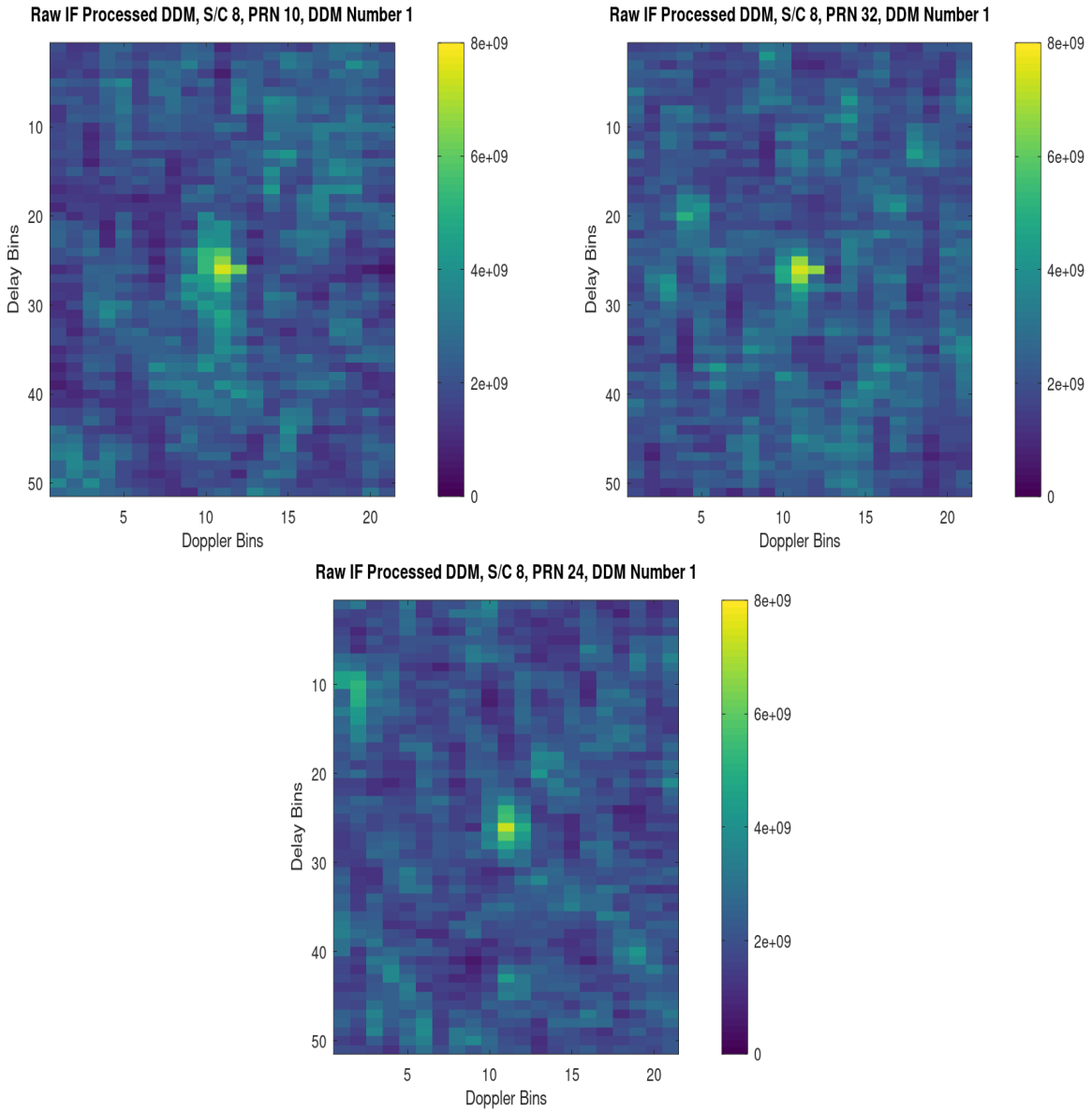

Figure 4.26: DDM of PRNs 10, 32, and 24 from sand reflections

4.7 Vegetation Reflection Results

DWF: Figure 4.27 depicts the DWF for vegetation reflections for PRNs 32, 31, and 10. The x-axis denotes delay, while the y-axis illustrates signal power. Each of the three DWFs exhibits nearly two or more discernible peaks. One of these peaks consistently stands slightly higher than multiple noise peaks, typically around 6e9.

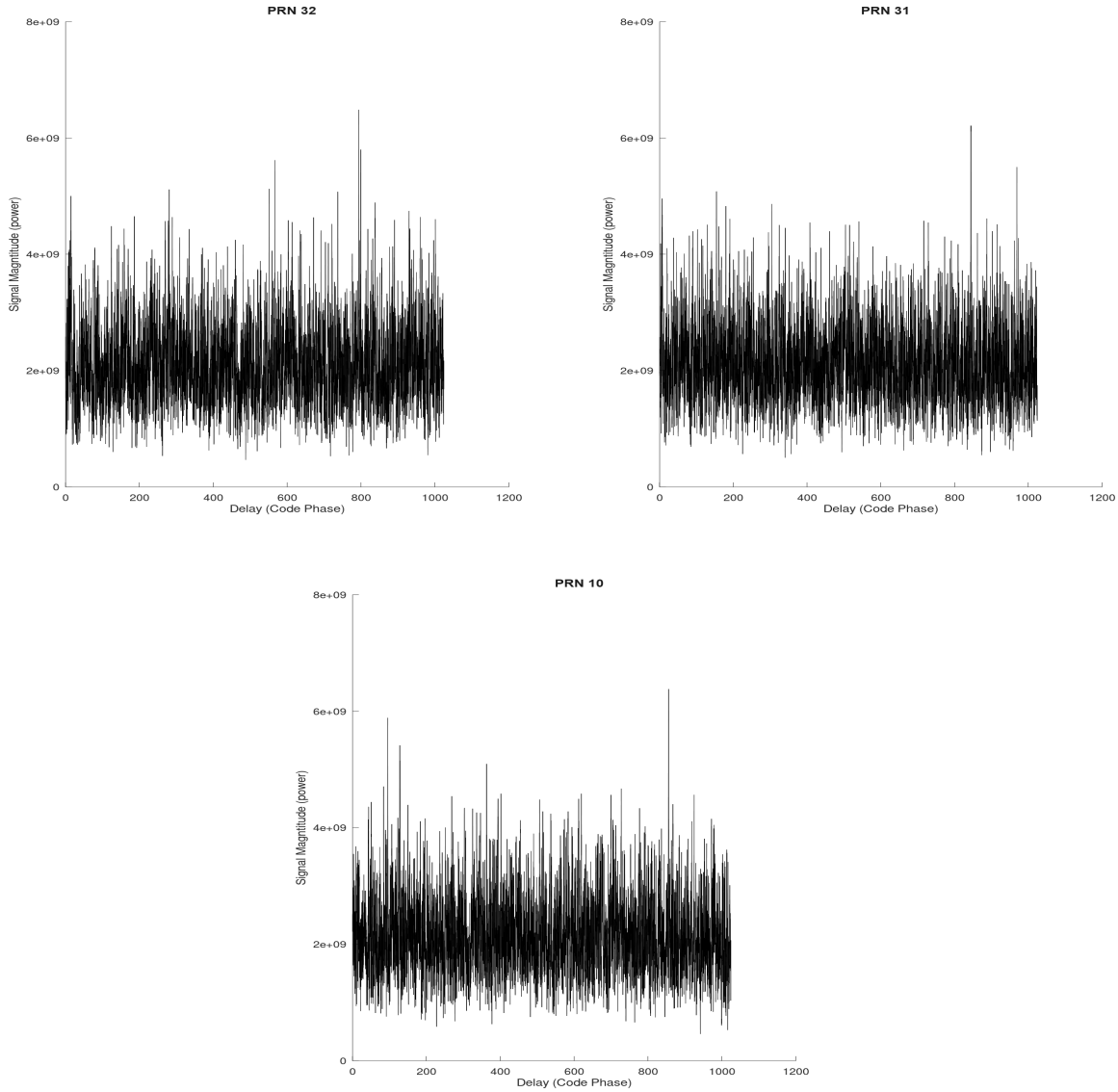

Figure 4.27: DWF of PRNs 32, 31 and 10 from vegetation reflections

DDM: Figure 4.25 illustrates the generated DDMs for PRNs 32, 31, and 10 in the over-vegetation dataset. The x-axis corresponds to doppler bins, the y-axis to delay bins, and the colours indicate correlation power. Notably, the DDMs exhibit a noise profile, appearing as if cropped around the highest noise peak. The DDMs are somewhat shadowy and do not exhibit a distinct shape.

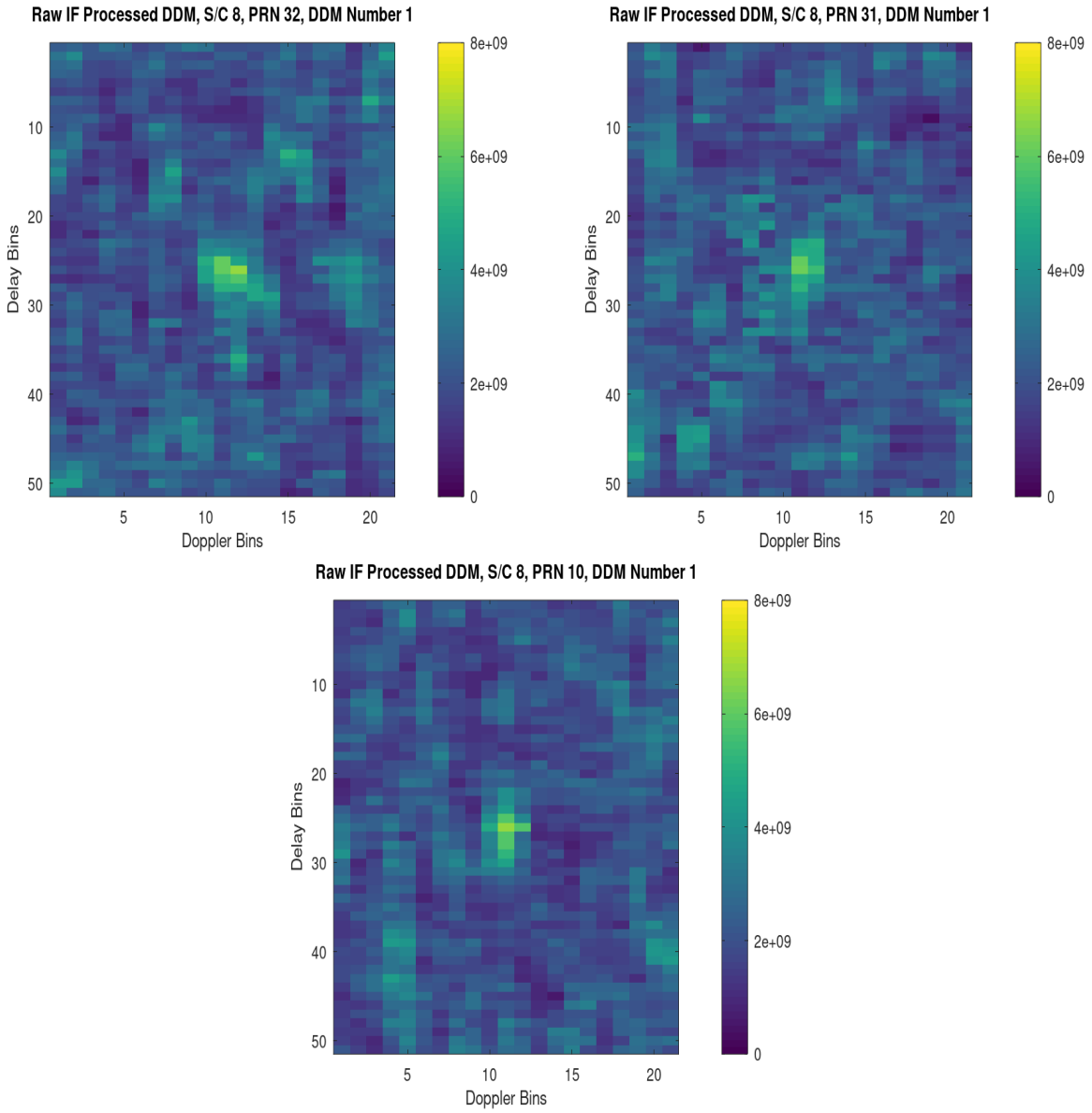

Figure 4.28: DDM of PRNs 32, 31 and 10 from vegetation reflections

4.8 Reflection Results Discussion

In Figure 4.19, all three DWFs exhibit a discernible peak above the noise floor. Notably, the circular shape of the DDMs challenges the anticipated horseshoe shape associated with water reflections, as discussed in Chapter 2. This circular appearance may be explained by calm lake water conditions, where the absence of strong winds causes the water surface to mimic land behaviour. This practical observation emphasizes the influence of environmental factors, such as wind, on DDM shapes, providing valuable insights into GNSS-R signal behaviour over small bodies of water. Furthermore, this could be influenced by the altitude of the UAV, which, when close to the ground, results in a much smaller reflection area compared to that of a system like CYGNSS, for example.

Similarly, over sand DWFs share similarities with the over water scenario, featuring a distinct peak above the noise floor. As expected, the DDMs display a circular shape, aligning with the coherent nature of land reflections. Additionally, the power of sand reflections consistently falls slightly below that of water reflections, aligning with the anticipated behaviour of sand reflections.

In contrast, the over vegetation DWFs appear noisier, with more than one prominent peak. This outcome is consistent with expectations, given the complex topography of the reflective surface marked by abundant vegetation and surface roughness. Consequently, the main peak is less powerful and shares space with nearby noise peaks. This pattern is reflected in the DDMs, resembling noise profiles cropped around the highest noise peak. Such results align with highly vegetated and rough terrains, where multipath signals and signal loss are commonplace.

In summary, the reflectometry results from over water, over sand, and over vegetation datasets confirm the hypothesis that smooth surfaces like sandy beaches or calm lake water produce stronger and more organized signals compared to rough, highly vegetated surfaces. The clear peaks and circular shapes observed over water and sand align with

expectations of coherence, while the noisier patterns and multiple peaks over vegetation correspond to the complex and rough nature of highly vegetated surfaces. These findings align with the GNSS-R literature and verify the payload's reflectometry capabilities.

Chapter 5
Conclusions and Recommendations

This chapter provides an overview of the design and construction of the GNSS-R payload, along with the subsequent post-processing steps used to assess its effectiveness in reflectometry applications. Furthermore, it provides conclusions and recommendations for future use, addressing aspects related to both the payload design and the post-processing of the captured data.

5.1 Conclusions

In this conclusion section, the research's two main objectives are discussed. Firstly, the development of a GNSS-R payload is addressed, and secondly, the validation of its functionality for commercial UAVs is examined. The payload met the first objective by meeting expectations for flight duration while adhering to mass and dimensional requirements. Furthermore, it demonstrated effective reflectometry capabilities in tests conducted across diverse terrains. The system can currently be used onboard a UAV to capture and store raw IF GPS reflectometry digitized signals. These signals can then undergo post-processing using NASA's CYGNSS code to generate Delay Doppler Maps (DDM) and Delay Waveforms (DWF) The following subsections will provide more detailed information on the fulfillment of each objective.

5.1.1 Payload Design and Development

This research aimed to design a reliable GNSS-R payload for commercial UAVs, using off-the-shelf components and meeting specific operational criteria. Individual testing ensured the individual reliability of each hardware component. The GNSS-R receiver can measure

both RHCP and LHCP signal strengths. The payload demonstrated operational reliability with a 20-minute flight duration, weighing 2kg-3kg, which is below the maximum limit and featuring dimensions designed to avoid interference with UAV sensors or propellers. In conclusion, the payload met all outlined requirements, fulfilling the research objective.

The payload components underwent thorough testing in controlled and real-world lab environments, employing simulators for lab assessments and in-situ measurements for real-world scenarios. This dual-testing approach aimed to comprehensively assess the components, contributing to their overall validation and reliability across various operating conditions. The antenna underwent outdoor testing using a commercial GNSS receiver, allowing it to identify six visible GPS satellites. The front-end was tested indoors using a GNSS signal simulator. The data captured during these tests was processed using a MATLAB script, revealing that all simulated satellite signals were successfully acquired. The payload underwent outdoor testing on a tripod as a final confirmation before flight campaigns. This scenario captured three visible satellites, as confirmed through post-processing.

5.1.2 Payload Verification for Reflectometry Applications

The second objective of this research aimed to validate the reflectometry capabilities of the developed payload through field tests conducted in diverse terrains, with Toronto Scarborough Bluffs selected as the testing site. This location was chosen due to the presence of a large body of water, a sandy beach, and dense vegetative terrain, providing a variety of landscapes for assessment.

The post-processing of the collected data involved utilizing NASA's CYGNSS C code, which is capable of generating both Delayed Waveform (DWF) and Delayed Doppler Map (DDM) data. To prepare the data for processing with the CYGNSS code, a reformatting process was applied. Before generating reflectometry results, a cold search was conducted on each dataset to identify all visible zenith GPS satellites. These satellites were then

cross-referenced with GNSS planning software, considering the time and location of the captured data, to ensure dataset accuracy. Subsequently, the top three GPS satellites with the highest correlation power were selected to generate DDMs and DWFs. The payload's reflectometry capabilities were affirmed by producing DWFs and DDMs for all three datasets, providing a comprehensive validation of its performance.

The DWF analysis revealed variations in signal strength, with water exhibiting higher power than sand, surpassing the densely vegetated area with rough terrain. Additionally, the DDM shapes aligned with expectations, depicting noisy peaks for vegetation, a circular coherent shape for sand, and lake water acting as a land reflection due to its calm and low-wind conditions. These findings serve to validate the payload's reflectometry capabilities across different terrains.

5.2 Future Work

While the project has succeeded within its defined scope, this research has significant unexplored potential. Future real-world applications based on this thesis involve utilizing a GNSS-R payload, made from COTS components, on a commercial UAV for practical use, particularly within the agricultural sector. GNSS-R makes use of existing GNSS signals, and when paired with a cost-effective payload made from easily accessible components suitable for UAV integration, it capitalizes on the versatility of UAVs as aerial platforms capable of flying at various altitudes to meet diverse spatial resolution requirements. This technology offers an enticing opportunity for accurately assessing soil moisture content, a critical parameter essential for effective agricultural and water management strategies.

The following subsections offer more detailed next-step considerations for potential future work, aiming to enhance and further expand upon the current research. This includes improvements in payload hardware, enhancements in post-processing techniques, and the incorporation of additional field experiments.

5.2.1 Payload Hardware Improvements

One crucial avenue for enhancing the performance of the payload in future missions is using more sensitive antennas that can operate without overloading the frond-end's AGC thresholds. While introducing an attenuator resolved this issue, it is more desirable to avoid the need for signal attenuation before entering the frond-end. During the payload's development and testing, various antennas were experimented with, some of which did not require attenuation. However, they were not chosen due to their RHCP polarization, whereas the nadir antenna necessitated LHCP. It is advisable to consider ordering an LHCP antenna with a similar VSWR ratio to assess if it can better match the frond-end, potentially eliminating the need for attenuation.

In the original configuration, the frond-end sampler operated at a 53 MHz ADC sampling rate, but this had to be reduced to 16.7 MHz due to the limitations of the onboard computer. If a more powerful onboard computer capable of sampling at 53 MHz becomes available in the future, it is recommended that it be employed. This potential upgrade could significantly improve the resolution of reflectometry products generated by the payload.

5.2.2 Post-Processing Improvements

The CYGNSS post-processing algorithm features a tracking option that leverages metadata from both CYGNSS and GPS satellites to track and calculate Doppler values, Doppler velocity, and acceleration. If a similar tracking algorithm could be developed and implemented for the payload onboard the UAV, it would offer significant advantages. This enhanced capability would contribute to greater precision in configuring the DDM-generating code, resulting in more accurate and improved results.

After making the suggested improvements, conducting additional flight experiments with the upgraded payload is practical. While Bluffer's Beach offered diverse topogra-

phies, future tests should include terrain-specific flights, like large sand dunes, farms, forests, and coastal towns. More diverse flights will broaden the dataset, offering a more comprehensive assessment of the payload's performance in varied environmental conditions.

References

ANTCOM (June 2017). *RHCP/LHCP L1/L2 Antenna, P/N: 42G1215RL-AA-XT-1.* ECCN 7E994. CC: 3CVE1, NAICS: 334511, S.Huynh.

Arnold, J. E. (1999). *Soil Moisture Study.* URL: https://weather.ndc.nasa.gov/landprocess/.

Balanis, C. A. (2016). *Antenna theory: Analysis and design.* John Wiley Sons.

Borre, K., D. M. Akos, N. Bertelsen, P. Rinder, and S. H. Jensen (2007). "4. GNSS Antennas and Front Ends". In: *A software-defined GPS and Galileo receiver: A single-frequency approach.* Birkhauser, 53–54.

Cardellach, E., F. Fabra, O. Nogués-Correig, S. Oliveras, S. Ribó, and A. Rius (Dec. 2011). "GNSS-R ground-based and airborne campaigns for ocean, land, ice, and snow techniques: Application to the GOLD-RTR data sets". In: *Radio Science - RADIO SCI* 46. DOI: 10.1029/2011RS004683.

Clarizia, M. P., C. P. Gommenginger, S. Gleason, M. A. Srokosz, C. Galdi, and M. Di-Bisceglie (2009). "Analysis of GNSS-R delay-Doppler maps from the UK-DMC satellite over the ocean". In: *Geophysical Research Letters* 36.2. DOI: https://doi.org/10.1029/2008GL036292. eprint: https://agupubs.onlinelibrary.wiley.com/doi/pdf/10.1029/2008GL036292. URL: https://agupubs.onlinelibrary.wiley.com/doi/abs/10.1029/2008GL036292.

CSA (2019). *Grants awarded under the flights and fieldwork for the Advancement of Science and Technology (FAST) 2017 announcement of opportunity.* URL: https://www.asc-csa.gc.ca/eng/funding-programs/programs/fast/grants-awarded-fast-ao-2017.asp.

Drone company, D. (2023). *DJI Matrice 300 RTK: Free shipping in Canada and the USA.* URL: https://drdrone.ca/pages/dji-matrice-300.

Egea-Roca, D, M Arizabaleta-Diez, T Pany, F Antreich, J. Lopez-Salcedo, M Paonni, and G Seco-Granados (2022). "GNSS User Technology: State of the Art and Future Trends". In: *IEEE ACCESS* 10, pp. 39939 –39968. ISSN: 2169-3536 (online). DOI: 10.1109/ACCESS.2022.3165594(online). URL: https://ieeexplore.ieee.org/document/9751089.

Egido, A., M. Caparrini, G. Ruffini, S. Paloscia, E. Santi, L. Guerriero, N. Pierdicca, and N. Floury (2012). "Global Navigation Satellite Systems Reflectometry as a Remote Sensing Tool for Agriculture". In: *Remote Sensing* 4.8, pp. 2356–2372. ISSN: 2072-4292. DOI: 10.3390/rs4082356. URL: https://www.mdpi.com/2072-4292/4/8/2356.

Ferreira, T., R. Sarnadas, C. Lopez, J. Curran, F. Pelica, and C. Prajanu (2018). *Front End*. URL: https://gssc.esa.int/navipedia/index.php/Front_End#cite_note-1.

Flores, A. (2021). *NAVSTAR GPS Space Segment/Navigation User Interfaces*. Tech. rep. GPS.gov.

Garrison, J. L. and S. J. Katzberg (2000). "The Application of Reflected GPS Signals to Ocean Remote Sensing". In: *Remote Sensing of Environment* 73.2, pp. 175–187. ISSN: 0034-4257. DOI: https://doi.org/10.1016/S0034-4257(00)00092-4. URL: https://www.sciencedirect.com/science/article/pii/S0034425700000924.

Gebre-Egziabher, D and S Gleason (2009). *GNSS Applications and Methods*. GNSS technology and applications series. Artech House. ISBN: 9781596933309. URL: https://books.google.ca/books?id=juXAE3SHQroC.

Gleason, S., S. Hodgart, Y. Sun, C. Gommenginger, S. Mackin, M. Adjrad, and M. Unwin (2005). "Detection and Processing of bistatically reflected GPS signals from low Earth orbit for the purpose of ocean remote sensing". In: *IEEE Transactions on Geoscience and Remote Sensing* 43.6, pp. 1229–1241. DOI: 10.1109/TGRS.2005.845643.

Gleason, S., S. Musko, T. Butler, C. Ruf, and D. McKague (2020). *Algorithm Theoretical Basis Document for High Resolution and Extended DDM Products*. INITIAL RELEASE. NASA.

Hajj, G. A., R. Ibañez-Meier, E. R. Kursinski, and L. J. Romans (1994). "Imaging the ionosphere with the global positioning system". In: *International Journal of Imaging Systems and Technology* 5.2, pp. 174–187. DOI: https://doi.org/10.1002/ima.1850050214. eprint: https://onlinelibrary.wiley.com/doi/pdf/10.1002/ima.1850050214. URL: https://onlinelibrary.wiley.com/doi/abs/10.1002/ima.1850050214.

Hall, C. and R. Cordey (1988). "Multistatic Scatterometry". In: *International Geoscience and Remote Sensing Symposium, 'Remote Sensing: Moving Toward the 21st Century'.* Vol. 1, pp. 561–562. DOI: 10.1109/IGARSS.1988.570200.

Hofmann-Wellenhof, B., H. Lichtenegger, and E. Wasle (2007). *GNSS-Global Navigation Satellite Systems*. ger ; eng. 1. Aufl. Vienna: Springer Verlag, Wien. ISBN: 9783211730126.

Ichikawa, K., T. Ebinuma, M. Konda, and K. Yufu (2019). "Low-Cost GNSS-R Altimetry on a UAV for Water-Level Measurements at Arbitrary Times and Locations". In: *Sensors* 19.5. ISSN: 1424-8220. DOI: 10.3390/s19050998. URL: https://www.mdpi.com/1424-8220/19/5/998.

IEEE-Std (1984). "IEEE Standard Letter Designations for Radar-Frequency Bands". In: *IEEE Std 521-1984*, pp. 1–8. DOI: 10.1109/IEEESTD.1984.81588.

Imam, R., M. Pini, G. Marucco, F. Dominici, and F. Dovis (2020). "UAV-Based GNSS-R for Water Detection as a Support to Flood Monitoring Operations: A Feasibility Study". In: *Applied Sciences* 10.1. ISSN: 2076-3417. DOI: 10.3390/app10010210. URL: https://www.mdpi.com/2076-3417/10/1/210.

J. Sanz Subirana J.M. Juan Zornoza, M. H.-P. (2011). *GNSS Basic Observables*. [ESA Navipedia]. URL: https://gssc.esa.int/navipedia/index.php/GNSS_Basic_Observables#:~:text=The%20basic%20GNSS%20observable%20is,c%20%CE%94%20T%20between%20them..

Katzberg, S. J. and J. L. Garrison (1996). *Utilizing GPS To Determine Ionospheric Delay Over the Ocean*. NASA Technical Memorandum 4750.

Kramer, H. J. (2013). *TechDemoSat-1 (technology demonstration satellite-1)*. URL: https://www.eoportal.org/satellite-missions/techdemosat-1#mission-status.

Lawrence, L. B. (2013). "Implemention and Evaluation of a Differential GPS Based on Smartphones and Internet Technology". MA thesis. Halmstad Embedded and Intelligent Systems Research (EIS), p. 52.

Leick, A., L. Rapoport, and D. Tatarnikov (2015). *GPS satellite surveying, fourth edition*. eng. 4th ed. Wiley. ISBN: 9781119018285.

Lowe, S., C. Zuffada, J. LaBrecque, M. Lough, J. Lerma, and L. Young (2000). "An ocean-altimetry measurement using reflected GPS signals observed from a low-altitude aircraft". In: *IGARSS 2000. IEEE 2000 International Geoscience and Remote Sensing Symposium. Taking the Pulse of the Planet: The Role of Remote Sensing in Managing the Environment. Proceedings (Cat. No.00CH37120)*. Vol. 5, 2185–2187 vol.5. DOI: 10.1109/IGARSS.2000.858350.

Lowe, S. T., C. Zuffada, Y. Chao, P. Kroger, L. E. Young, and J. L. LaBrecque (2002). "5-cm-Precision aircraft ocean altimetry using GPS reflections". In: *Geophysical Research Letters* 29.10, pp. 13–1–13–4. DOI: https://doi.org/10.1029/2002GL014759. eprint: https://agupubs.onlinelibrary.wiley.com/doi/pdf/10.1029/2002GL014759. URL: https://agupubs.onlinelibrary.wiley.com/doi/abs/10.1029/2002GL014759.

Martin-Neira, M. (Jan. 1993). "A Passive Reflectometry and Interferometry System (PARIS): Application to ocean altimetry". In: *ESA Journal* 17, pp. 331–355.

Masters, D., V. Zavorotny, S. Katzberg, and W. Emery (2000). "GPS signal scattering from land for moisture content determination". In: *IGARSS 2000. IEEE 2000 International Geoscience and Remote Sensing Symposium. Taking the Pulse of the Planet: The Role of Remote Sensing in Managing the Environment. Proceedings (Cat. No.00CH37120)*. Vol. 7, 3090–3092 vol.7. DOI: 10.1109/IGARSS.2000.860346.

Milligan, T. A. (2005). *Modern Antenna Design*. IEEE Press.

Mini-Circuits (2022a). *VAT-10+ Coaxial SMA Fixed Attenuator*. Rev. H, M151107, 200520. URL: https://www.minicircuits.com/pdfs/VAT-10+.pdf.

— (2022b). *ZFBT-4R2G+ Coaxial Bias-Tee Data Sheet*. Rev. C, M151107. URL: https://www.minicircuits.com/pdfs/ZFBT-4R2G+.pdf.

Moernaut, G. and D. Orban (Feb. 2009). "GNSS antennas an introduction to bandwidth, gain pattern, polarization, and all that". In: 20, pp. 42–48.

NASA-CCDIS (2023). *NASA's Archive of Space Geodesy Data*. URL: https://cddis.nasa.gov/archive/gnss/products/2237/.

Nogues-Correig, O., E. Cardellach, J. Sanz-Campderros, and A. Rius (2007). "A GPS-Reflections Receiver That Computes Doppler/Delay Maps in Real Time". In: *IEEE Transactions on Geoscience and Remote Sensing* 45.1, pp. 156–174. DOI: 10.1109/TGRS.2006.882257.

NT-Labs (2019). *NT1065$_L E_D S_v$*2.19. Ver. 2.19. 4-Channel GPS/GLONASS/Galileo/BeiDou/NavIC/QZSS L1/L2/L3/L5 band RF Front-End IC.

NTLAB (2021). *NT1065_USB3 data files structure.pdf*. RELATED DOCUMENTS. LT-09303 88 Zalgirio, Vilnius, Lithuania: NTLAB. URL: https://drive.google.com/drive/folders/0B6dx7OglV_tYTHlQVzl0QzQzY3M?resourcekey=0-tdzkIDhuj6B_Dl9ybmTMqA.

Onrubia, R., J. Querol, D. Pascual, A. Alonso-Arroyo, H. Park, and A. Camps (2016). "DME/TACAN Impact Analysis on GNSS Reflectometry". In: *IEEE Journal of Selected Topics in Applied Earth Observations and Remote Sensing* 9.10, pp. 4611–4620. DOI: 10.1109/JSTARS.2016.2556745.

Onrubia-Ibáñez, R. (2020). "Advanced GNSS-R instruments for altimetric and scatterometric applications". PhD thesis. UPC, Departament de Teoria del Senyal i Comunicacions, pp. 14–17. DOI: 10.5821/dissertation-2117-328191. URL: http://hdl.handle.net/2117/328191.

Pascual, D., H. Park, R. Onrubia, A. A. Arroyo, J. Querol, and A. Camps (2016). "Crosstalk Statistics and Impact in Interferometric GNSS-R". In: *IEEE Journal of Selected Topics in Applied Earth Observations and Remote Sensing* 9.10, pp. 4621–4630. DOI: 10.1109/JSTARS.2016.2551981.

PO.DAAC JPL, N. (2017). *Cyclone Global Navigation Satellite System (CYGNSS)*. URL: https://podaac.jpl.nasa.gov/CYGNSS?tab=mission-objectives&sections=about.

Razal, R., S. Gleason, and C. Ruf (Oct. 2014). "The NASA CYGNSS mission: a pathfinder for GNSS scatterometry remote sensing applications". In: *Proceedings of SPIE - The International Society for Optical Engineering* 9240, pp. 5–6. DOI: 10.1117/12.2068378.

Ruf, C., R. Rose, and S. Gleason (Oct. 2014). "The NASA CYGNSS mission: a pathfinder for GNSS scatterometry remote sensing applications". In: *Proceedings of SPIE - The International Society for Optical Engineering* 9240. DOI: 10.1117/12.2068378.

Ruffini, G., F. Soulat, M. Caparrini, O. Germain, and M. Martín-Neira (2004). "The Eddy Experiment: Accurate GNSS-R ocean altimetry from low altitude aircraft". In: *Geophysical Research Letters* 31.12. DOI: https://doi.org/10.1029/2004GL019994. eprint: https://agupubs.onlinelibrary.wiley.com/doi/pdf/10.1029/2004GL019994. URL: https://agupubs.onlinelibrary.wiley.com/doi/abs/10.1029/2004GL019994.

Schmidhuber, M. and T. Lopez-Delgado (2022). "Telemetry, Commanding and Ranging System". In: *Spacecraft Operations*. Ed. by F. Sellmaier, T. Uhlig, and M. Schmidhuber. Cham: Springer International Publishing, pp. 357–375. ISBN: 978-3-030-88593-9. DOI: 10.1007/978-3-030-88593-9_18. URL: https://doi.org/10.1007/978-3-030-88593-9_18.

Sehnal, M. (n.d.). *GNSS Reflectometry*. GGOS (Global Geodetic Observing System). URL: https://ggos.org/item/gnss-reflectometry/#learn-this.

Sickle, J. V. (2001). *GPS for Land Surveyors, Third Edition*. Taylor & Francis. ISBN: 9781575040752. URL: https://books.google.ca/books?id=sHvJLDqkLFcC.

Southwest-Antennas (Oct. 2015). *GPS Active L1 Antenna, +11 dB Active Gain, SMA(m)*. 1027-004. Doc: 217-0001-541, Page 4.

Susi, M. (July 2017). "Improved receiver tracking models for scintillation monitoring". PhD thesis. University of Nottingham, p. 170.

Süzer, A. E. and H. Oktal (2017). "PRN code correlation in GPS receiver". In: *2017 8th International Conference on Recent Advances in Space Technologies (RAST)*, pp. 189–193. URL: https://api.semanticscholar.org/CorpusID:25538039.

Texas-Instruments (Apr. 2015). *Principles of Data Acquisition and Conversion*. Tech. rep. SBAA051A. Texas Instruments Incorporated.

Trimble-Inc. (2023). *Trimble GNSS Planning Online*. Version 1.6.1.0. URL: https://www.gnssplanning.com/#/settings.

WMO (2021). *What are Essential Climate Variables (ECVs)?* URL: https://gcos.wmo.int/en/essential-climate-variables/about.